Seismic performance evaluation of RBS-CFT connections with bidirectional bolts under cyclic loads

Thesis submitted
in partial fulfillment of the requirement
for the degree of

Doctor of Philosophy

by

Subhra Paul
(166104029)

Department of Civil Engineering
Indian Institute of Technology Guwahati, 781039
October 2022

Certificate

This is to certify that the thesis entitled "***Seismic performance evaluation of RBS-CFT connections with bidirectional bolts under cyclic loads***" submitted by Mr. Subhra Paul, Roll No. 166104029 to the Indian Institute of Technology Guwahati, for the award of the degree of Doctor of Philosophy in Civil Engineering is a record of bonafide research work carried out by him under our supervision and guidance. The thesis work, in our opinion, has reached the requisite standard fulfilling the requirement for the degree of Doctor of Philosophy.

The results contained in this thesis have not been submitted in part or full to any other University or Institute for award of any degree or diploma.

(*Dr. Sajal K. Deb*)
Professor, Department of Civil Engineering,
Indian Institute of Technology Guwahati
Guwahati-781039, INDIA.
Date: 18-10-2022 Place: Guwahati

Acknowledgement

This thesis is the result of the experimental investigation carried out at the department of Civil Engineering at Indian Institute of Technology. Guwahati, India. At the outset, I would like to express my deep sense of gratitude from the core of heart to my supervisor Prof. Sajal K. Deb initiating an interesting and innovative research topic and for their personal commitment, interesting discussion and valuable advice. I appreciate the opportunities I got to develop myself in a new area of structural engineering. Prof. Deb has been continuously encouraging throughout the work and contributed with valuable guidance and supervision. Such a huge steel experimental work was done in structural laboratory of IIT Guwahati, which demanded lot of new test set up, fabrication of frames and mobilization of construction materials etc.

My supervisors have taken lot of pains to manage the finance for all these materials and workmanship for the fabrication of test specimens. Prof. Deb has never left me alone during the planning, organizing and conducting the tests. In every phase, I found them very close to share the agonies of failure and joys of success, in all these experimental works. I deeply acknowledge the support of Retd. Dr. Atop Lego, Chief Engineer, Arunachal Pradesh P.W.D., during procure of the test specimens for the experimental program. This experimental work would not have been possible without the support of technical staff of Structural Engineering Laboratory of IIT Guwahati. I express my gratitude to Dr. Arun Chandra Borsaikia, Scientific Officer and Mr. Biswajit Debnath, Technical superintendent for their earnest effort to manage the all instruments and workers needed for test-setup of the specimens, managing long steel bars for fixing the specimens to the strong floor and especially for operating the MTS servo hydraulic dynamic actuators during the testing. I express my thanks to Pankaj da, and Suresh da for their continuous help and ideas for fixing and removing of the specimens during the course of the experiments.

I am also grateful to Mr. Susanta, Mr. Bhrigu, Mrs. Archana and Mrs. Jhuri who are the office staffs of Civil Engineering Department for their help in various occasions. I would also like to express my thanks to workshop staffs of Workshop and Center of instrument facility for helping me in fabrication of test sample and many other works involving steel fabrication.

Thanks, are also due to Prof. Hemant B. Kaushik, Prof. K.S.R. Krishna Murthy and Prof Anjan Dutta, who were the members of my doctoral committee and who contributed with valuable remarks and ideas to obtain the final results of this research work. Special thanks to Prof. A. Dutta, who has given me lot of blessings and love for my research work and life.

I would like to acknowledge the encouragement and enthusiasm which I received from Prof. Satyabrata Choudhury of NIT Silchar, Assam. I am thankful to Dr. Supratik Maitra of District Horticulture Office, Nadia (W.B.) who has given me suggestion for doing research in IIT-Guwahati. I am grateful to Mr. Rahul Dev Barman of Microsoft, who has given me suggestion regarding reference books and papers related to OpenSees.

Many of my friends and colleagues like Saroj, Siddharth, Tamen, Vivekananda, Sukanta, Barri, Sagar, Arnab, Prasanta, Chandan, Koustav, Nasim, Pallab, Manjusha, Tori, Ajay, Biplab, Subhankar and Abhay who inspired and helped me in different times for my research work in IIT Guwahati, I am grate full to all of them. Special thanks to Abhay H. Rangoonwala to teach me the interaction property in the ABAQUS Model. I found him one of the talented post graduate scholar working under Prof. Deb.

Finally, I express my thanks to my parents, who has been looking with enormous patience during the days of my research. Few words of thanks to my teachers Mr. Asit Paul and Mr. Sukanta Saha, to whom I have learnt basic education of mathematics and science. Indeed, I am grateful to my uncle Mr. Bipul Paul, Executive Engineer, Arunachal Pradesh P.H.E., who helped me in several family affairs in my college days. My heartfelt thanks are for my parents, by whose blessings I could complete this work successfully.

Mr. Subhra Paul
IIT, Guwahati (India)
18-10-2022

Abstract

It was reported that the beam-column connection in steel buildings acts as one of the weakest parts in moment resisting steel framed structures during past catastrophic seismic event such as Northridge (1994) and Kobe (1995) earthquakes. The failure of beam-column connections is the reason for the poor behaviour of welded steel frame constructions in different parts of the world during earthquakes. It was observed that the external connections experienced more damage than the interior connections during earthquakes. The failure of beam-column connections during earthquakes prompted new interest to improve the seismic behaviour of moment resisting frames. Large number of studies were conducted on the beam-column connections to improve the strength, energy dissipation capacity and ductility since 1994.

Engineers observed that column flanges in steel buildings were ruptured, welds were fractured and there was imperfect plastic hinge development in the beam-column joint region particularly during Northridge earthquake. Ideally, it is expected that plastic hinge will form in beam only. But it was observed that plastic hinge formed in panel zones, joints and sometimes in column also. These incidents established that there are needs for improvement of seismic performance of connections to ensure adequate strength, energy dissipation capacity and ductility. Several conventional methods of strengthening the beam-column connection were tried. But, these conventional methods had many problems. However, these difficulties and problems could be minimized by introducing reduced beam section (RBS). Hence, recent research efforts were focused on the use of RBS for improving the seismic performance of moment resisting frames (MRFs).

Moment resistant frame connection, comprising of concrete-filled tube (CFT) column and steel-*I* beam, has been widely studied. This type of frame gained popularity in construction of multi-storeyed buildings over the last two decades. CFTs combine the advantages of both steel tubes and concrete. The confinement provided by the steel tube removes the need for formwork during construction, and the concrete lowers susceptibility of local tube wall buckling.

Broadly RBS are classified in two categories: (*i*) shaved cut RBS (*ii*) drilled cut RBS. Shaved cut RBS has been one of the primary research areas after the Northridge earthquake. Large numbers of research works have been carried out on two different types of shaved cut RBS: (*i*) radius cut RBS (*ii*) constant cut RBS. Studies on shaved cut RBS established that radius cut RBS is efficient as compared to constant cut RBS. Radius cut RBS connection has large energy dissipation capacity and ductility as compared to the other RBS. But, it was also reported that higher out-of-plane deformation (twist) of the beam was observed in case of radius cut RBS.

Steel beam-CFT connection are critical elements of frames because this element ensures all components work together. Many connections types were studied to connect steel beam to CFT column. Bolted steel beam-CFT connection was found to have potential of providing high energy dissipation capacity, ductility and higher load-carrying capacity. In this study, seismic performance of RBS-CFT connection with bidirectional bolts was evaluated.

Material properties of beam, CFT, bolts were evaluated using steel coupon tests. *M30* grades of concrete was used to fill the CFT. Four different types of RBS-CFT connection with bidirectional bolts were designed based on guidelines reported in literatures. The proper design procedures were followed to design the each of the RBSs. In this study, one new type of shaved cut RBS designated as *V*-cut RBS is designed. The new RBS are developed with the following objectives: (*i*) reduction of out of plane deformation, (*ii*) enhancement of energy dissipation capacity and ductility. The seismic performance of *V*-cut RBS-CFT connection with bidirectional bolts is evaluated and compared with conventional radius-cut RBS and drilled cut RBS-CFT connections.

In this study, all the RBS-CFT connection with bidirectional bolts were subjected to displacement controlled cyclic loading. Total six numbers of geometrically scaled RBS-CFT connection were tested. Two types of strain sensors were used to record the strain value in the RBS zone and panel zone of RBS-CFT connections. Strains were measured in multiple locations in the flanges of RBS zones to record the strain distributions. One inclinometer was used to measure the rotation of the beam. Servo hydraulic dynamics actuators (Make: MTS, USA, Model 244.31) are used to apply cyclic loads to the specimens. During testing, a hydraulic jack was used to maintain a constant axial load on the column to simulate gravity loading. To avoid the accidental out of plane deformation, two specifically constructed vertical posts were placed on either side of the test specimen. The loading history was chosen in accordance with the AISC 341-10 and SAC/BD-97/02 standards.

Recorded data was used to study hysteretic behaviour, envelope curve, stiffness degradation, energy dissipation capacity, strain distribution, ductility for shaved cut connections first. In terms of the above-mentioned parameters, seismic performance of RBS-CFT connections were analysed to arrive at the important inferences. It was observed that *V*-cut RBS had higher ductility and energy dissipating capacity as compared to the radius cut RBS.

Similarly, recorded data also was used to study hysteretic behaviour, envelope curve, energy dissipation capacity, strain distribution, ductility for two types of the drilled cut connection. It was observed that varied drilled cut (*VD*-cut) RBS had higher energy dissipation capacity and stiffness as compared to constant drilled cut (*CD*-cut) RBS.

Nonlinear finite element analysis of RBS-CFT connections with bidirectional bolts was performed using the general-purpose software ABAQUS (v 6.6-1, 2006) and OpenSees (v.17.7.3, 2006). The failure patterns of the connections were obtained by the ABAQUS software. Force vs. displacement behaviour under increasing monotonic load were simulated for the all the connections which were then compared with those obtained from the experimental study. A simplified numerical model was proposed in OpenSees platform for simulation hysteresis loops which were then validated by comparing with those obtained from the experimental study.

Fragility function are useful tools for post-earthquake damage assessment. Developing the fragility functions of RBS-CFT connections from experimental studies are considered to be the most reliable one among the different approaches. However, studies on development of fragility functions of semi-rigid connection from experimental data was limited, since such experiments involve time, infrastructures and large investment. An attempt was made to develop experimental fragility functions in the present study considering two damage states.

From this study, it was evident that adopted design of RBS-CFT connections satisfied strong column-weak beam concept as no damage was observed in panel zone or CFT during the experimental study. Semi-rigid nature of these connections ensured overall ductile behaviour of the connections. All of the connections fulfilled requirement for special moment resistant frames as per the recommendation of AISC (2016) by achieving the 0.04 rad minimum rotational capacity. Thus, it is established that RBS-CFT connections with bidirectional bolts would be effective in improving seismic performance of steel framed building in seismically active regions.

Table of Contents

List of Figures

List of Tables

List of symbols

a: Distance of cut from the face of column
b: Length of cut
c: Depth of cut
R: Radius of cut
b_f: Width of flange
t_f: Thickness of flange
d_b: Depth of beam
ϕ: Diameter of drill size
f_y: Yield strength of steel material
s: Distance from center of column to center of radius cut
s_h: Distance from column face to center of radius cut
L: Center to center distance between columns
L': Length of beam
f_u: Ultimate strength of steel material
$\Phi(\cdot)$: Standard normal cumulative distribution function
β: Logarithmic standard deviation
μ_X: Mean of random variable X following normal distribution
σ_X: Standard deviation of random variable X following normal distribution
O_i: Observed frequencies
E_i: Expected frequencies
D_n: Critical value for K-S goodness-of-fit test
χ_v: Critical value for chi squared goodness-of-fit test
n: Sample size
n_c: Number of classes
l: Total number of classes
k: Number of parameters estimated
v: Degrees of freedom for chi squared goodness-of-fit test

Abbreviations

MRFs:	Moment resisting frames
RBS:	Reduced beam section
UTM:	Universal testing machine
CFT:	Concrete filled tube
SCWB:	Strong column-weak beam
DRBS:	Double reduced beam section
HSFG:	High strength friction grip
LVDT:	Linear variable displacement transducer
SHS:	Structural Hollow Section
CP:	Concentrated plasticity
EDP:	Engineering Demand Parameter
EEP:	Extended End Plate
FEMA:	Federal Emergency Management Agency
IDR:	Inter-story drift ratio
C3D8R:	Continuum 3-dimensional eight noded brick elements with reduced integration
C3D6:	Continuum 3-dimensional six noded linear prism elements
RI:	Rupture Index
LS:	Life Safety
RP:	Reference point
GOF:	Goodness-of-fit
MRF:	Moment Resisting Frame
NLTH:	Non-Linear Time History
NPB:	Narrow Parallel Flange Beam
ORF:	Ordinary Moment resisting Frame
PEEQ:	Equivalent plastic strain
RBS:	Reduced Beam Section
SCWB:	Strong Column Weak Beam
SHS:	Square Hollow Section
SMF:	Special Moment resisting Frame

CHAPTER-1
Introduction

CONTENTS

1.1 Background

Moment resisting frames (MRFs) are one of the oldest structural forms and used in seismically active regions for many decades. MRFs have been popular among engineers for mainly two reasons *i*) highly ductile structural forms *ii*) good space versatility. In these MRFs, beams are rigidly connected to the columns by welding as shown in Fig. 1.1. Before 1994, welded flange, welded web connections were the most general types of connection used in MRFs. These frames resist the lateral loads effect in form of shear force and bending moment in the frame elements and connections. The lateral stiffness of the entire MRFs depends on flexural rigidity of beam and column [1]. But, in the Northridge earthquake (1994) many of the MRFs were damaged. Exactly

Fig. 1.1: Steel moment resisting frame [1]

a year later, the Kobe earthquake (1995) confirmed the similar shortcomings in steel MRFs. Observations after the earthquakes in Northridge (1994) and Kobe (1995) revealed that welded MRF suffered brittle fractures. Northridge Earthquake resulted different types of fractures in welded moment connections. Fig. 1.2(a) showed a typical fracture failure in welded MRF connection designed prior to 1994. The most commonly fractures were initiated in the beam flange and extended to the column web and flange. Fig. 1.2(b) showed the typical fracture paths of pre-Northridge connections [2].

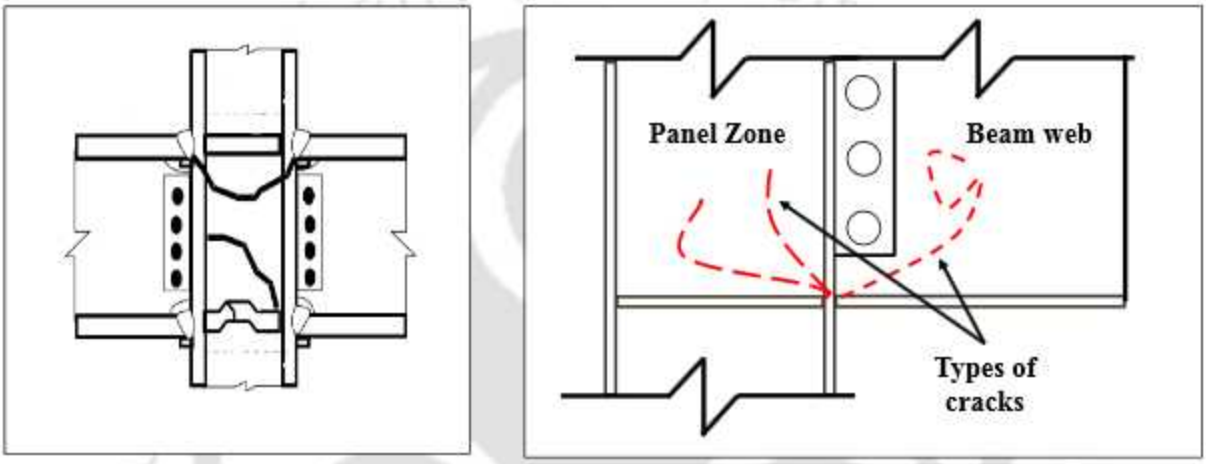

Fig. 1.2 (a) Typical fracture failure in MRF connection [2] (b) Crack propagation in MRF connection

These two seismic events drew global attention towards further research to upgrade the seismic behaviour of steel MRFs. Many modifications in design procedures and its connection types were started thereafter. Reduced beam section (RBS) is one of the such modification in the beam-column connections. Large volume of experimental studies on this RBS-column connection was performed to improve the seismic performance of MRFs after the Northridge earthquake (1994) [3].

1.2 RBS-column connection

RBS-column connection is among one of the most widely studied steel connections developed after the Northridge (1994) and the Kobe (1995) earthquakes. In this type of connection, a portion

of the beam flange is shaved or drilled, depending upon the type of RBS, at a small distance away from the beam-column interface as shown in Fig. 1.3. Reduction of beam flange width makes this zone weakest in the connection and hence, forces the formation of plastic hinge in the beam away from the joint region [4]. Reduction of beam flange width was achieved by shaving the flanges or drilling holes in the flanges. The idea of shaving the beam flanges to improve the seismic performance of steel connections was first proposed by Plumier [5]. The experimental study on RBS connection was first carried out by Chen and yeh [6]. The results confirmed that RBS connection significantly enhance the ductility and energy dissipation capacity as compared to conventional beam-column connections.

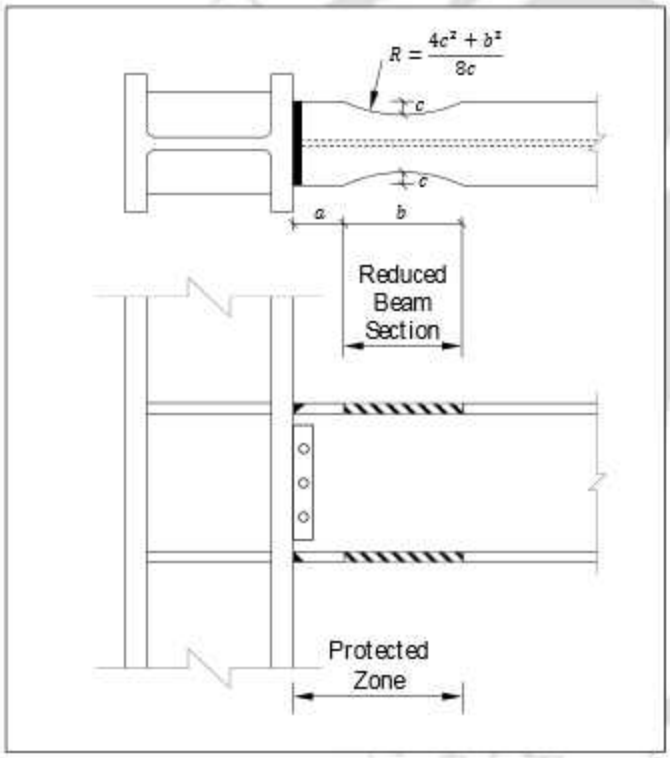

Fig. 1.3: Typical geometry of radius-cut RBS

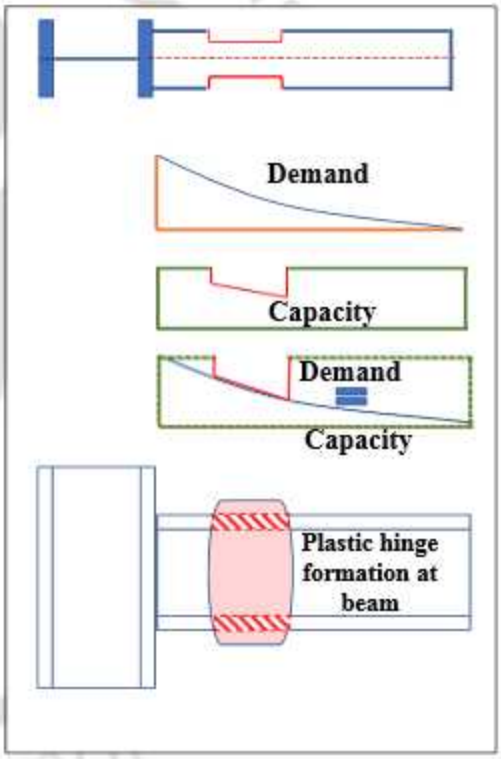

Fig. 1.4 Design principle of RBS

In an electrical circuit, a fuse has been used as a safety device that operates to provide overcurrent protection of an electrical circuit. Similarly, the RBS acts as a fuse for steel MRFs. The steep moment gradient in the beam under an earthquake excitation usually induce high level of stress concentration at the interface between the beam flange and column. The reduction in cross sectional area in beam would reduce its moment capacity at a discrete location to avoid high stress concentration in the panel zone and column.

It was found that by shaving or drilling of the beam flanges near beam-column connections, the moment capacity of the beam can be reduced as shown in Fig.1.4. By this mechanism the provided moment capacity is equal to or slightly less than that of the demand value. Thus, an enlarged plastic hinge could be formed in the pre-defined location in the beam [7].

Reduced beam sections (RBS) are broadly classified into two categories: (*i*) shaved cut and (*ii*) drilled cut [6]. These two categories of RBS were primarily studied for enhancement of seismic performance of MRFs. Constant cut, radius cut RBS can be considered as shaved cut while constant drilled cut (*CD*-cut) and varied drilled cut (*VD*-cut) RBS comes under the second category. Fig. 1.5 showed the different types of reduced beam section (RBS).

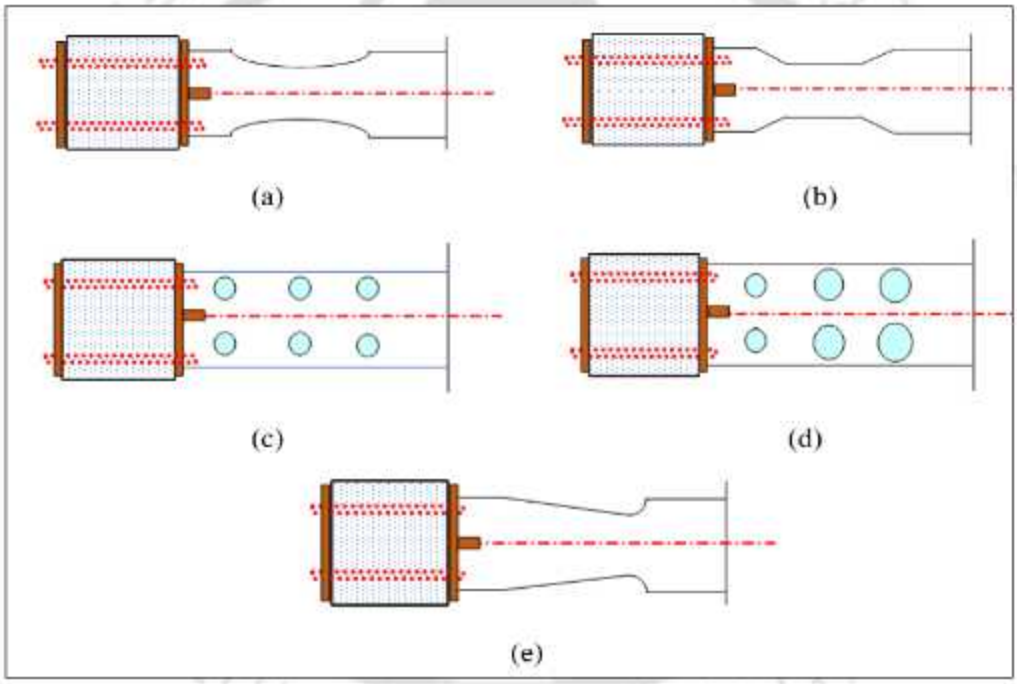

Fig. 1.5 Different types of RBS (a) Radius cut (b) Constant-cut RBS (c) Constant drilled cut RBS (d) Varied drilled cut RBS (e) *V*-cut RBS

1.3 Problem identification

Steel beam-column connections play very significant role in seismic behaviour of steel MRF. Welded beam-column connection experienced huge damages due to poor energy dissipation capacity and ductility. In almost all connections, steel beam was connected to *I* or *H*-shaped steel

column using various types of welding [8]. After the Northridge earthquake (1994), efforts were made to design a new type of connection with large energy-dissipating capacity and ductility. The primary objectives for the design of the new type connection were to improve energy dissipation capacity and ductility [9].

Extensive research focusing on the seismic behavior of the steel beam-CFT connections was carried out in the last two decades. Steel beam-CFT connections can be broadly classified into three categories. Welding was used to join steel beam to CFT columns in the first category. This sort of connection offers high bearing capacity, stiffness, and energy dissipation. But this class of connection were found to be more prone to brittle failure of the weld when subjected to additional bending during earthquakes [10]. In the second connection category, one of the rigid moments resisting connections, the steel beam passes through the column via openings in the steel tube. Due to the complexity in fabrication, this category of connection is not generally adopted for practical implementation [11]. Third category of connection consists of bolted steel beam-CFT connection which improve overall ductility of the frame and enhances ease of fabrication. Bolted beam-CFT connection generally behaves as a semi-rigid connection. This class of connection facilitates relatively simple and low-cost reparability in case of any damage following an earthquake [12-15]. Bidirectional bolted steel beam-CFT connections were considered as a viable alternative due to simple fabrication process, and easy field installation. Their seismic behaviour were extensively studied both experimentally and numerically [16-17].

The most common types of shaved cut RBS with potential of field implementation are radius cut RBS, constant cut RBS for their excellent energy dissipating capacity and ductility. The radius cut RBS was extensively studied by various researcher for ensuring formation of plastic hinges in beam along with high energy dissipating capacity and ductility. However, some of the studies reported that this RBS experiences out-of-plane deformation due to lateral torsional buckling. It was also observed that the constant cut RBS experienced fracture failure due to sudden change in geometry.

Therefore, it is necessary to develop new types of RBS in order to minimize out-of-plane deformation and avoid sudden change in geometry for stable hysteretic behavior with enhanced energy dissipation capacity by ensuring higher plastic rotation [18].

Further, it was found that very limited experimental studies were carried out on seismic performance evaluation of two popular drilled cut RBS designated as: *CD*-cut RBS and *VD*-cut RBS. There were no available literatures on comparison of experimental response of shaved cut RBS-CFT semirigid connection with that of the drilled cut RBS-CFT semi-rigid connection.

This research work focusses on design and fabrication of a new RBS, designated as *V*-cut, for stable hysteretic behavior with higher energy dissipation capacity and lower of out-of-plane deformation. In this present experimental study, geometrically scaled RBS-CFT connections with bidirectional bolts were tested under cyclic loads for assessment of their force-displacement hysteretic behavior. Comparison of energy dissipation capacity, ductility and out-of-plane deformation of *V*-cut RBS was made with those parameters of the conventional radius cut RBS and two variants of drilled cut RBS connection.

1.4 Objectives of the Present Study

Literature review carried out in the present study revealed that seismic performance of RBS-CFT connection with bidirectional bolts has not been studied so far despite their unique earthquake-resistant features. Therefore, an attempt has been made in the present study to understand the seismic behaviour of RBS-CFT connection with bidirectional bolts. Present research work also addresses the concerns and gap areas identified during the literature review. Primary objectives of the present study are:

- To develop a new RBS specimen to ensure stable force-displacement hysteretic behaviour and to reduce lateral-torsional deformation in the RBS-CFT connection with bidirectional bolts.
- To carry out experimental study for the evaluation of seismic performance of four different types of RBS-CFT connections with bi-directional bolts under cyclic loading.
- To carryout comparative study on seismic performance of different types of RBS-CFT connections with bidirectional bolts.
- To develop a finite element model of RBS-CFT connections for numerical study on ABAQUS for nonlinear monotonic behaviour and failure patterns of the RBS-CFT connection. Also, to develop a simple nonlinear cyclic behaviour model of RBS-CFT

connections in OpenSees platform for simulation of force-displacement hysteresis behaviour.

- To develop experimental fragility curves of RBS-CFT connections for assessment of their seismic vulnerability.

1.5 Scopes of the present study

An extensive study was undertaken to achieve the above-mentioned objectives by carrying out several tests on RBS-CFT connection with bidirectional bolts and this was followed by numerical simulation and seismic vulnerability study. Scopes of the present study were:

1. Design and fabrication of new RBS specimen (*V*-cut RBS) was carried out. The mechanical properties of beam, column and bolts were experimentally evaluated under uniaxial loading conditions using universal testing machine (UTM).
2. Experimental test setup was fabricated for carrying out cyclic testing of the RBS-CFT connections. Two steel post were placed on either side of the test sample to avoid accidental out-of-plane deformation of the RBS-CFT connections. A hydraulic jack fixed with A-type frame was used to apply axial load to the column.
3. Seismic behavior of RBS-CFT connection were evaluated for the geometrically-scaled specimens under cyclic loading. Displacement controlled cyclic loading was applied using servo controlled dynamic actuator. Response of RBS-CFT connections was captured by means of several strain sensor, inclinometer, LVDTs and load cells.
4. Finite element models of RBS-CFT connections were developed in ABAQUS platform to analyze and understand their behaviour on the basis of stress-distribution and failure pattern under monotonically increasing load.
5. OpenSees platform was used to develop simplified numerical models to analyze the force-displacement hysteretic behaviour of RBS-CFT connection with bidirectional bolts.
6. Fragility functions were developed for seismic vulnerability assessment. Data collected from past research works and experimental data obtained in the present study were combined to develop the fragility curves for two distinct damage states.

1.6 Outlined of the dissertation

Besides the present introductory chapter, the dissertation consists seven more chapters. The brief outline of the thesis is as given below:

- **Chapter 2:** presents review of literature covering various aspects of RBS, CFT, and bidirectional bolts along with the summary of the literature review and research gaps.
- **Chapter 3:** describes the design outline for new RBS, material testing, instrumentation and experimental setup required to perform the present experimental study.
- **Chapter 4:** focuses on seismic performance evaluation of four nos. of shaved cut RBS-CFT connection based on experimental study. Different seismic parameters are calculated to evaluate the seismic performance.
- **Chapter 5:** highlights seismic performance evaluation of two nos. of drilled cut RBS-CFT connection by performing experimental study. Different seismic parameters are calculated to evaluate the seismic performance.
- **Chapter 6:** presents numerical modelling of RBS-CFT connection with bidirectional bolts using ABAQUS and OpenSees software.
- **Chapter 7:** focuses on development of experimental fragility curves for seismic vulnerability assessment of the RBS-column connections.
- **Chapter 8:** summarizes entire work reported in this thesis, major conclusions are highlighted and the scope of future research is outlined.

CHAPTER-2

Literature Review

CONTENTS

2.1 Overview

RBS-column connections have potential to become popular design option in seismically active zones in different parts of the world. The seismic performance of RBS-column connections is evaluated by their energy dissipation capacity, ductility and failure patterns, etc. The performance of RBS evolved with time in terms of their geometrical shapes, design assumptions, joint details and construction methodology, etc. Several experimental and numerical studies have been carried out in the past to understand its seismic behaviour. In this chapter, relevant literature has been reviewed to evaluate the seismic behaviour of the RBS-column connection investigated by various researchers. The seismic performance of connections in past earthquakes was discussed first. Concrete filled tube (CFT) is frequently employed in civil engineering structures due to its unique load bearing capacity, ductility, low cost and construction convenience. Due to these reasons CFT are replacing normal *I* and *H* shaped column in high-rise buildings. The benefits of concrete-filled tube (CFT) column are explored. Different methods for modifications of connection are reviewed to get some ideas about various design alternative of designing the connection. Thereafter, the experimental behaviour of different types of RBS-column connections are discussed. Various numerical models developed for simulating the lateral load behaviour of RBS-column connection are also reviewed. This is followed by a discussion on design guidelines and their influence on the overall behaviour of MRFs.

2.2 Past performance of welded-frame structure

Welding is one of the oldest fabrication techniques used in steel construction to connect the beam and column elements. Different types of welded-framed structures are constructed in seismically active regions. Popularity of these structures is mainly due to their construction convenience and its aesthetics [19]. But, Northridge (1994) and Kobe (1995) earthquake demonstrated that the seismic performance of welded connections has been inferior compared to that of the bolted connections. In the welded framed structure, fractures were initiated at the junction of the beam-column connection, as shown in Fig. 2.1.

Fig. 2.1 Typical fracture paths at the welded beam-column connection [20]

In general, high intensity earthquakes inflicted damages in the connection of welded-frame structure due to poor welding quality, low toughness of weld, weld damaging, shear distortion of panel zone, poor connection design, and poor-quality control. The extent of the damage experienced by the welded-frame connections vary with types of connections. Most of damages are attributable to the design methodology. All the connections were designed based on the strength-based design approach before 1994. The design philosophy/ procedure of the beam-column connections was modified to enhance energy dissipation capacity, ductility, and strength after mid-nineties [20].

2.3 Modifications in connections

After the Northridge earthquake in 1994, researchers in different parts of the world focused on improving the seismic performance of beam-column connections, particularly in countries with

high levels of seismic activities. These research works led to the adoption of a new design procedure. The latest design guidelines would help to avoid brittle fractures at beam-column connections in steel structures [21-24]. Many numerical and experimental investigations were carried out by researchers to improve the ductility and energy dissipation capacity of the connections by either strengthening the column or weakening the beam section. The ultimate aim was to achieve higher inelastic rotation capacity, without sudden degradation of strength, in the connections.

Popov *et al.* [25] proposed that the connections must have flexural capacity 80% of plastic moment M_p of the connected beam (M_p= plastic moment of the beam) at 0.04 rad rotation level to meet the necessary criteria for special moment resisting frames. This recommendation was adopted in AISC 341 (2016). Broadly two different methodologies have been used to enhance the seismic performance of the connection. In the following section, a detailed overview of these two methodologies is discussed.

2.3.1 Strengthening the connection

Strengthening of connections was done by adding some extra elements to the connection. Strengthening of connection has been done by adding additional elements, including cover plates and flange plates, triangular haunches, straight haunches, upstanding ribs, lengthened ribs, side plates and bolted brackets [26-30] as shown in Fig. 2.2. This method based on reinforcing the connection so that the connection becomes stronger than the beam so that the plastic hinge moves away from the column face to the beam. Therefore, this would help to avoid stress concentrations at weld access holes, premature fractures resulting from potential weld defects, etc. However, the strengthening strategies do have a few limitations, which are: (i) increased beam moments at the column face, which necessitates the use of a larger column section to accommodate increased panel zone shear demand (ii) increased plastic rotation demands in the beams, (iii) complicated welding processes and increased the field welding.

2.3.2 Weakening of the beam Section

The second strategy is the weakening of the beam section. Weakening of the beam section has been done by reducing the flange width. Here, the beam flange width is reduced at a small distance

away from the column face, thereby forcing plastic hinge formation at that location. The reduced beam section (RBS) is broadly classified into two categories (*i*) shaved cut RBS and (*ii*) drilled cut RBS. Various types of RBS connections are shown in Fig. 2.3.

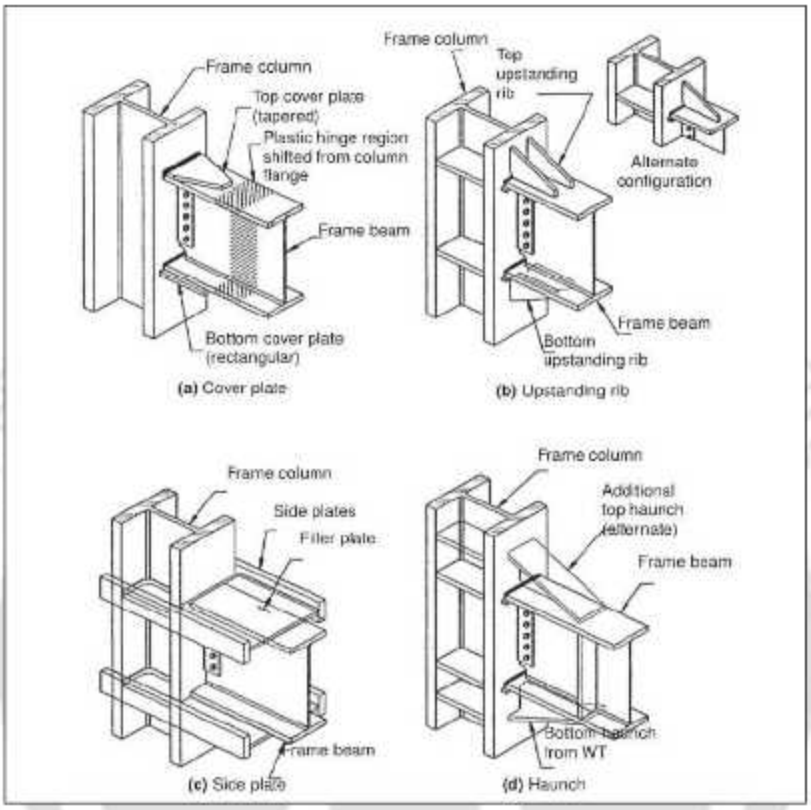

Fig. 2.2: Post-Northridge connection strengthening strategies [9]

Reduced flange width is used to improve the performance of the connection. In these methods plastic hinge formed in the beam, away from the connection region. The performance of RBS largely depends on the types of geometries of the RBS Zone, and types of connections. Various investigations were carried out by Chen *et al.* [31], Engelhardt *et al.* [32] and Uang *et al.* [33] to find the effect of RBS on the performance of beam-column connection considering different geometrics. The outcomes from these experimental studies indicated that RBS-column connection performed better than the strengthened connections.

Here, two different methods related to the modification of different connections are discussed. Weakening the beam section or RBS has been one of the popular and efficient methods to enhance seismic performance in terms of energy dissipation capacity and ductility. In the subsequent

sections, research works carried out on RBS by past researchers are discussed, and important outcomes of these studies have been highlighted with critical comments. In the following section, reasons for adopting CFT in place *I* /*H* sections for experimental study on RBS-column connection are highlighted.

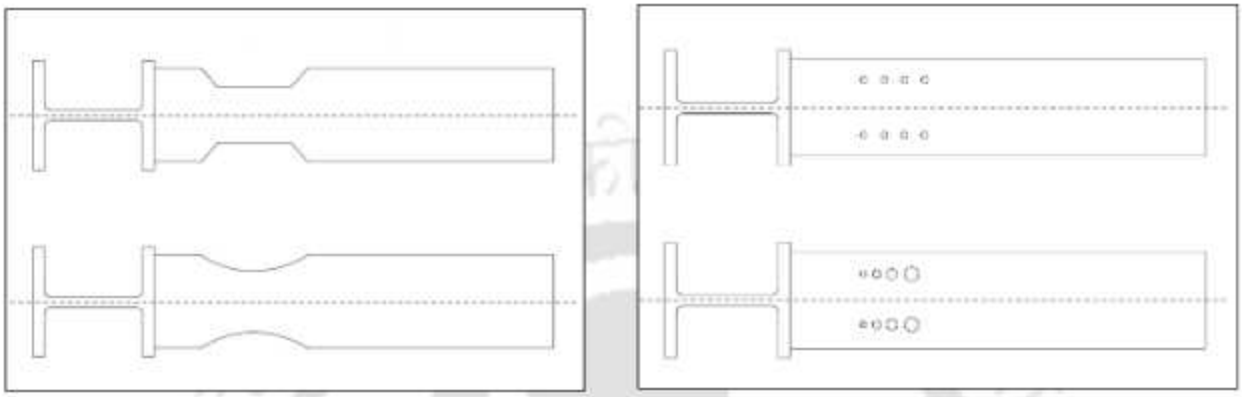

Fig. 2.3: Various types of RBS connection

2.4 Advantages of CFT column

Concrete filled tubes (CFT) have been used in MRFs since 1968. Application of CFT in buildings, bridges, and other structures has been observed. Bridge *et al*. [34] reported that a structural system with CFT combines the advantages of both steel and concrete elements. Two types of structural component that are widely used in practice for column members are open sections and Concrete Filled Tube (CFT). Moreover, in comparison with open sections i.e., *I* or *H* sections, tubular sections are more efficient when dealing with bending, compression, and torsion because generally, tubular sections have the advantages of symmetrical characteristics, large gyration radius, and good local stability. Concrete-filled steel tubes have many advantages as compared to other types of columns, including *i*) the tube eliminates the column formwork during construction, *ii*) it provides longitudinal and confining reinforcement, so that usual reinforcement for concrete columns is often not used, *iii*) the steel pipe prevents spalling of the concrete, and *iv*) the concrete prolongs the local buckling of the tube wall, *v*) CFTs possess more strength, lateral stiffness, and ductility as compared to those of other columns of similar size. Extensive experimental and analytical works have been carried out to study the behaviour of CFTs under different loading conditions. It is evident from the Fig. 2.4, that the strength and ductility of the CFT is significantly

higher than those of steel tube, reinforced concrete and steel tube RC member. Therefore, a better understanding of the behaviour of connections is needed to make CFT a vital alternative in steel moment-resisting frames [35-38].

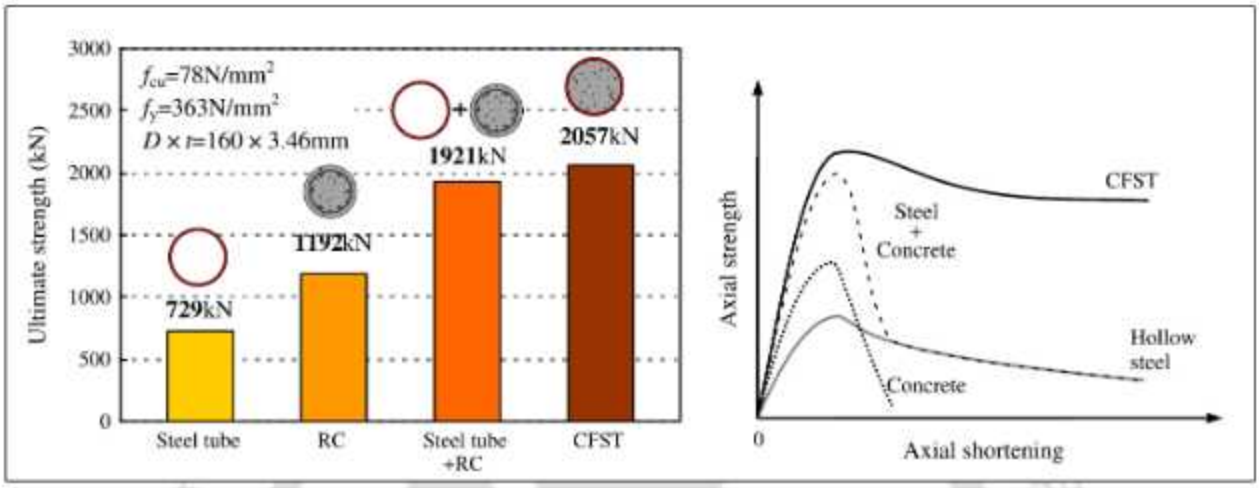

Fig. 2.4: Axial behaviour of various types of column section [34]

2.5 Steel beam-CFT connection

Connections play an important role in the case of any steel framed buildings. Large volumes of literature related to the experimental investigation of beam-CFT connections are available. Available steel beam-CFT connections may be broadly classified into three categories. A review of available literatures on these three types of connection categories are discussed in the following paragraphs.

2.5.1 Welded connection

Three different approaches have been used in the welded connections. In the first approach, the steel beam is directly welded to the CFT columns. Xu *et al.* [39] studied the seismic performance of welded beam-CFT connections. In the second approach, the interior, exterior, through diaphragm was welded to the CFT column, and then the steel beam is welded to the diaphragms shown in Fig. 2.5. Yu *et al.* [40] performed an experimental study on diaphragm connection. In the third approach, stiffeners have been used in place of through diaphragm to connect steel beam with CFT. Shin *et al.* [41] reported that the connection with horizontal or vertical stiffener shown

in Fig. 2.6 performed better as compared to that of the other welded connections. Based on experimental study, Mahin *et al.* [42] concluded that welded connection has a high bearing capacity, large stiffness, and good energy-dissipation capacity. However, these connections experienced large tensile stress under bending. This tension gets transferred to the tube wall inducing large deformation in the tube wall, which causes the brittle failure of the weld. Moreover, brittle fractures in the welded connection in special MRFs have been observed during a severe seismic event.

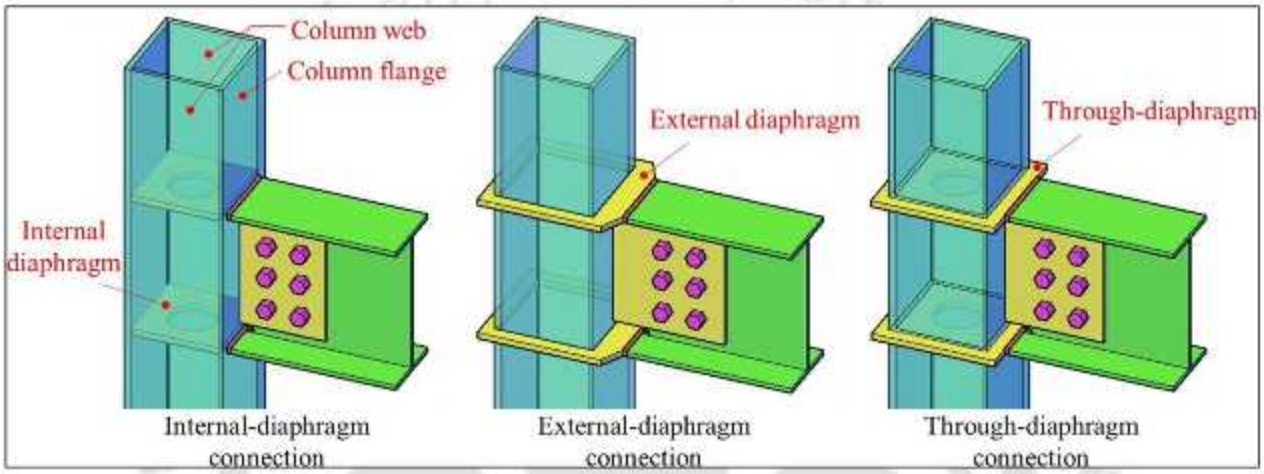

Fig. 2.5: Various types of diaphragm connection [40]

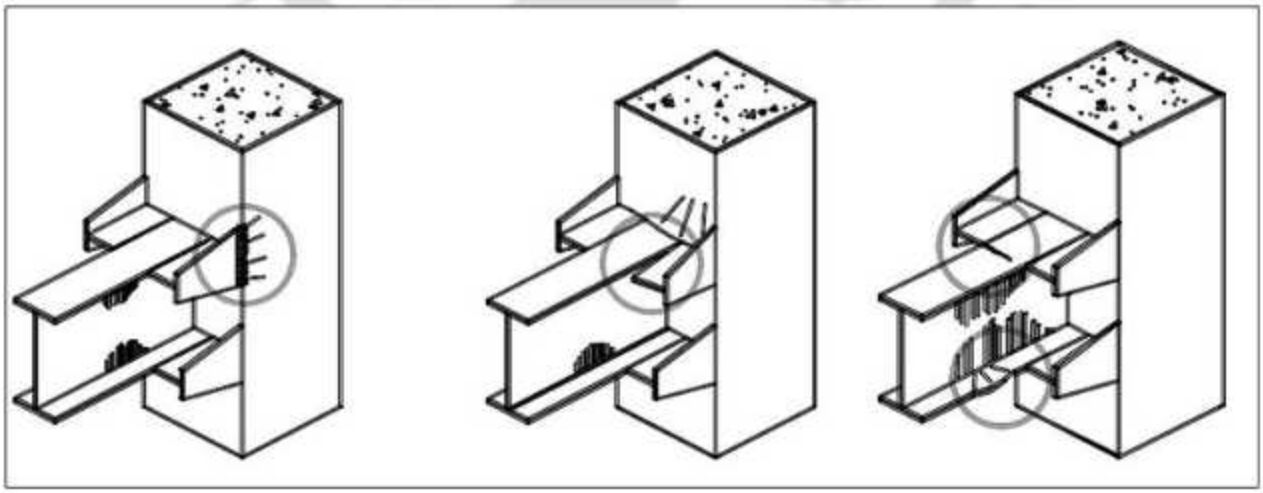

Fig. 2.6: Steel beam-CFT connection with stiffener [41]

2.5.2 Through beam connection

In the second type of connection, the steel beam passes through the hole made in the steel tube. Sheet *et al*. [43] and Jeddi *et al*. [44] observed that these connections behaved as rigid moment-resisting connections. However, the complicated fabrication process of these connections, limited practical implementation of this category of connections.

2.5.3 Bolted connection

The performance of the third category of the connections has been investigated by various researchers, including Tao *et al*. [45], Wang *et al*. [46], Tizani and Pitrakkos [47], to enhance the overall ductility and energy dissipation capacity of MRF. This class of MRFs connection would also improve both speed of fabrication and quality of connection. In addition, the restraint effect of the pretensioned bolts improved the performance of panel zones. Existing studies indicated that the bolted steel beam-CFT connections performed better as compared to that of the other categories of connections during severe seismic events [48-49]. Bolted steel beam-CFT connections can broadly be classified as: (*i*) blind bolted connections (*ii*) bidirectional bolted connections, as shown in Fig. 2.7.

Blind bolted connection: Yao *et al*. [50] conducted many studies on blind bolted connections in the last several decades, including experimental studies, theoretical analyses, and numerical simulations. Zhou *et al*. [51] first conducted the experimental study on steel beam-CFT tube connection by blind bolts. Further, analytical models of strength, stiffness and moment-rotation curve have been proposed by various investigators, including Wang *et al*. [52], Tizani *et al*. [53], Oktavianus *et al*. [54] and Thai and Uy 2016 [55].

Wang *et al*. [56] reported the typical failure modes of blind bolted connections, such as (*i*) local buckling appearing in the tube wall near bolt holes and (*ii*) lacerations in the corner of the steel tube. It was observed that the blind bolts in the tension zone are slowly pushed out when it is subjected to a bending moment. Thus, the column wall bulges out when bolts are subjected to tension. In turn, the corner of the steel tube is lacerated due to the stress concentration. These resulted the poor panel zone integrity, low bending capacity, and low stiffness of the connection.

Bidirectional bolted connection: Bidirectional bolted connections would facilitate ease of construction, and provide better panel zone integrity, higher load-carrying capacity, and larger initial stiffness as compared to these parameters for blind bolted connections. Bidirectional bolted connection for a steel-concrete composite structure was proposed in the 1980s, and it has been observed that this connection type ensured good seismic performance. Subsequently, many studies on the performance of these connections have been conducted by various researchers [57-63].

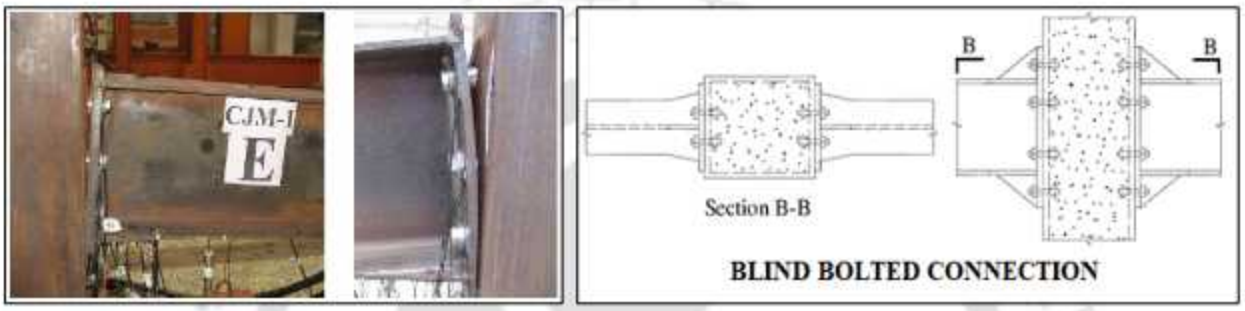

(a)

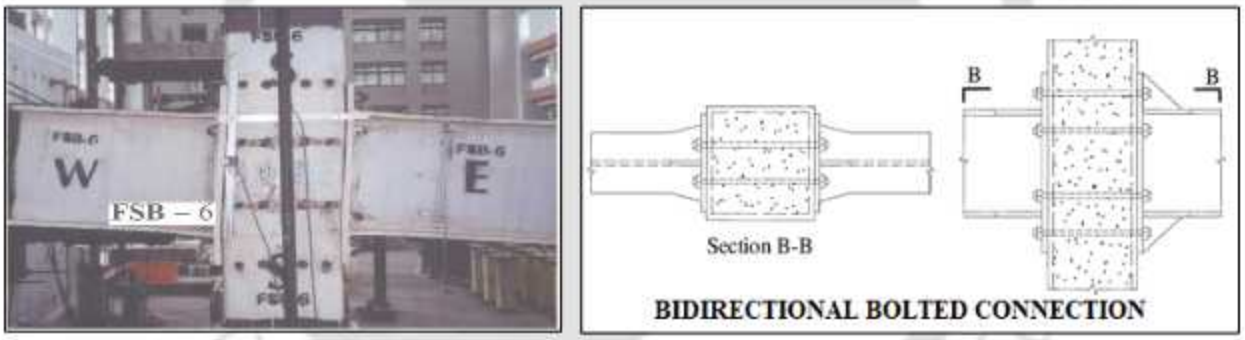

(b)

Fig. 2.7 (a) Blind bolted connection (b) Bidirectional bolted connection [57]

Zong *et al.* [64] studied stiffened bolted endplate connections and doubled split-tee plate connections with different axial compression ratios to evaluate the seismic performance of the connections. Wu *et al.* [65] investigated the seismic behaviour of bidirectional bolted connections for CFT columns and *H*-beams. Experimental results established that the seismic performance of the connection and their overall stability have been very good. Zong *et al.* [66] reported that the pseudo-static performances of stiffened bolted endplate connections were better than that of the regular bolt-welding connections. However, Alignment of bidirectional bolts in orthogonal

directions, particularly for interior joints, is challenging. It would be necessary to place the bolts in different levels in the orthogonal directions in the connections as shown in Fig. 2.7.

2.6 Experimental study on RBS-column connections

In the recent past, experimental studies on the evaluation of the performance of RBS-column connections have attracted the attention of researchers in different parts of the world. Different types of RBS-column connections have been studied to evaluate their seismic performance. Seismic performance of RBS-column connections is influenced by their mechanical characteristics in terms of ultimate loading capacity, ductility capacity, stiffness degradation, failure patterns, strain distribution in the RBS and panel zone of the joint. The geometry of RBS also influences the overall performance of RBS-column connections.

The seismic performance of the connection depends on many factors. Quasi-static testing of RBS-column connections has been generally carried out to evaluate the seismic performance. It is used to evaluate the influence of important parameters on the cyclic behaviour of such connections. Low-frequency cyclic testing facilitates visual observations of crack growth and failure patterns which provide better insight on the performance of the structure. Important results of past studies are discussed here in the following sub-sections.

Failure patterns of connections influence the seismic performance. For all steel MRF systems, the role of failure patterns is quite significant. Strong-column-weak-beam (SCWB) design principle was widely adopted for design of these systems to facilitate formation of plastic hinge in the beams while the columns and panel zones were allowed to remain in essentially elastic condition. However, after the Northridge Earthquake, many steels moment-resisting frames suffered from damage. These damages occur in the panel zone areas, beams, and columns. Nakashima *et al*. [67] reported that most of these failed connections showed fractures around the beam-column connections and in the columns. Several steel frame structures were studied using RBS to move the plastic hinges from the connection region to connected beam.

Chen *et al*. [68]; Popov *et al*. [69]; Jones *et al*. [70]. Kulkarni *et al*. [71] reported that RBS could shift the plastic hinge to the beam from the column ends compared to regular steel beam connection

based on the experimental and numerical study as shown in Fig 2.8. Thus, the RBS-column connection satisfied the strong column weak beam (SCWB) concept, and plastic hinge formation was observed in the beam in steads of the column or panel zone.

Oh *et al.* [72] reported that the RBS connection has a much higher energy dissipation capacity than the normal steel beam-column connection due to the increment of plastic hinge length in the RBS zone as shown in Fig. 2.8. Other past studies also showed that any form of RBS has much more energy dissipation capacity than a regular steel beam connection [73-77].

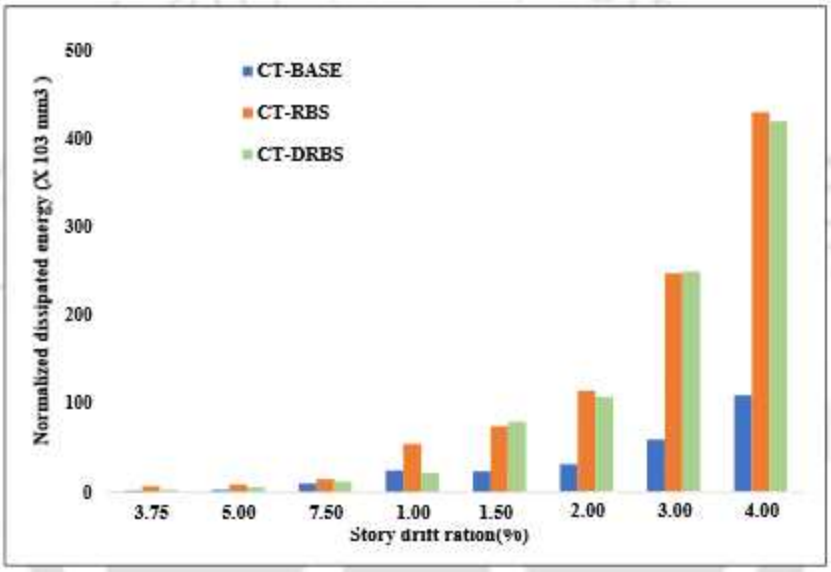

Fig. 2.8 Comparison of energy dissipation capacity for each story drift ratio [72]

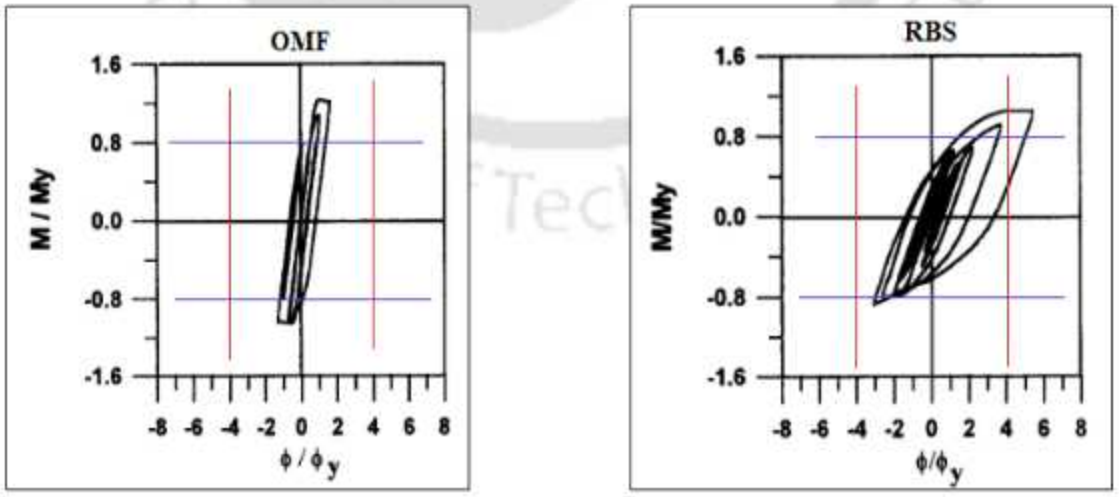

Fig. 2.9 Comparison with normalized M-ϕ curve [78]

Chen *et al.* [78] reported that ductility of the RBS-column connection much higher than normal beam-column connection because of large inelastic rotation in RBS connection. RBS-column connection enhanced the ductility capacity by achieving 0.04 rad rotation as shown in Fig. 2.9.

The shape of the RBS also greatly influences the overall performance of RBS-column connections. The seismic performance of different types RBS discussed in the following sub-sections.

In shaved cut RBS, two types of configurations have been the subject of various studies since 1994. Many pioneering research works have been carried out on RBS-column connections by researchers. The first experimental study was conducted on the constant cut RBS and the radius cut RBS. Seismic performance of shaved cut RBS is reviewed and reported here in the following paragraphs.

Plumier [5] performed the first experiments on constant cut RBS connections, using HEB 300 columns and HEA 260 beams. Moore *et al.* [80] reported that the constant cut RBS exhibited fracture due to the abrupt change in its geometry. Due to this reason, the constant cut RBS was not studied significantly. Pachoumis *et al.* [81] reported that the constant cut RBS performed poor in terms of energy dissipation, plastic rotation and steady decrease in strength capacity as compared to that of radius cut RBS.

Engelhardt *et al.* [82] reported that radius cut RBS minimize the stress concentrations in the panel zone area of the connections. Hence, it also reduces inelastic rotations and enhances the ductility. It was reported in literature that radius cut RBS performed better as compared to the constant cut RBS in terms of energy dissipation, plastic rotation and ductility capacity. Based on experimental and analytical studies, Deri *et al.* [83], reported that the radius cut RBS performs better than the polyline RBS. Morshedi *et al.* [84] reported that the radius cut RBS-column connection enhanced the ductility significantly. Design criteria for the radius cut RBS were introduced into FEMA 350, ANSI/AISC 341, EC-8 part-3, and Indian standards also. A beam-column connection with a radius-cut RBS must be designed to sustain a moment of at least 0.8 times the total plastic moment of the connected beam, according to Indian standard (IS 800:2007).

However, Rahnavard *et al*. [85] reported that higher out-of-plane deformation of the beam was observed in the case of radius cut RBS-column connection as compared to that of the other RBS due to the large depth of cut in the RBS zone.

The first study on the drilled cut RBS was performed in 2012. Recently, drilled cut RBS connection are becoming popular because of their good seismic performance. Limited nos. of experimental works have been carried out on these RBS connections. The first design of drilled cut RBS was proposed by Vetr *et al*. [86]. In addition to these two types of RBS, Vajdian *et al*. [87] studied the rhombus-shaped drilled cut RBS. The experimental study reported that drilled cut RBS has higher energy dissipation capacity, ductility and less out-of-plane deformation, less inelastic strain distribution in the flange as compared to radius cut RBS.

Fabrication of the drilled cut RBS is much easier as compared to the radius cut RBS. However, very few experimental studies have been conducted on constant drilled cut RBS connection. Experimental studies carried out by Fanaie *et al*. [88]; Parveri *et al*. [89] indicate that the constant drilled cut RBS-column connection can delay and reduce out-of-plane deformation and increase the energy dissipation capacity as compared to the radius cut RBS because of drilling in discrete location of the flange in the RBS zone. Fanaie *et al*. [88] reported that flange of drilled cut beam experienced maximum strain level in the range 2-3 times of the yield stain level. Maximum strain level in the drilled-cut RBS is low as compared to that of the radius cut RBS because of reduced drill size in the flange of RBS zone.

Limited studies are conducted on the varied drilled cut RBS-column connections by Rahnavard *et al*. [90]; Deri *et al*. [91]. It was reported that the varied drilled cut RBS ensured higher energy dissipation capacity, a lower magnitude of out of plane deformation, and good plastic deformation capacity as compared to these of the constant drilled cut RBS and radius cut RBS. Further, flange of the varied drilled cut beam experienced the buckling phenomena during experiments at higher rotational level in the range 0.05-0.07% rad as reported by Fanaie *et al*. [88].

The performance of conventional steel beam-column connection has been improved by introducing RBS. Brittle fractures of welded connections have been reduced using RBS. It has been reported that energy dissipation capacity, and ductility can be improved significantly as

compared to those parameters in the frame conventional welded steel frame. Varied drilled cut RBS is capable of delaying and reducing out-of-plane deformation, energy dissipation capacity and ductility as compared to those parameters of the constant drilled cut RBS. Furthermore, all RBS fulfilled the requirements of special moment resisting frames after attaining 0.04 rad rotation as specified by ANSI/AISC-341, 2016, clause G3-6 (b).

2.7 Numerical study on RBS-column connections

It may not be always possible to carrying out experimental works because of time or financial constraints. In that case, numerical simulation proved to be a useful tool for evaluating the seismic performance of steel MRFs. Using finite element software such as ABAQUS, OpenSees, and ANSYS, several numerical analyses of steel RBS-column connections were conducted. Based on different types of modelling assumptions, many researchers carried out several numerical analyses to understand the overall behaviour of RBS-column connections. Some of these numerical studies are discussed as follows:

Pachoumis *et al.* [81] performed finite element analysis on RBS-column connection using ABAQUS. Two types of numerical simulations were carried out here considering shell element and solid element. The first model was developed using two-dimensional four-noded thin shell elements (S4R) with reduced integration. Eight-noded solid elements (C3D8R) were used for the second model. Due to the biaxial symmetry of the specimens, only half model with the appropriate boundary conditions was simulated to reduce the computational time and for better viewing of the results. Numerical results based on eight noded solid elements showed similar trends as that obtained from the experimental studies.

Kulkarni and Vesmawala [71] carried out 3D finite element modelling in ANSYS to study the seismic behavior of the radius cut RBS-column connection. An element SOLID-45 from the ANSYS element library was used to model the subassemblies. A standard quasi-static loading was applied at the beam tip to performed the analysis. Results from the finite element study were almost similar with the experimental study. It was observed that conventional beam-column connection failed to shift the plastic hinge from panel zone as shown in Fig. 2.10. But connection with the

RBS effectively shift the formation of plastic hinge from the panel zone to the reduced zone of beam. This study experimentally proved that radius cut RBS are effective to control the damage of column.

Rahnavadh *et al.* [85] performed the numerical simulation on eight numbers of RBS-column connections considering four different types of RBS. Four different numerical parameters were calculated based on numerical study. Equivalent plastic strain (PEEQ), Rupture Index (RI), energy dissipation capacity and out of plane deformation were calculated for each RBS-column connection using ABAQUS software. It was observed that the varied drilled cut RBS ensured higher energy dissipation capacity as compared to that of the others RBS. RBS with varied hole has minimum out-of-plane deformation as compared to other RBS connections. It was recommended to use drilled cut RBS for moment resisting frames.

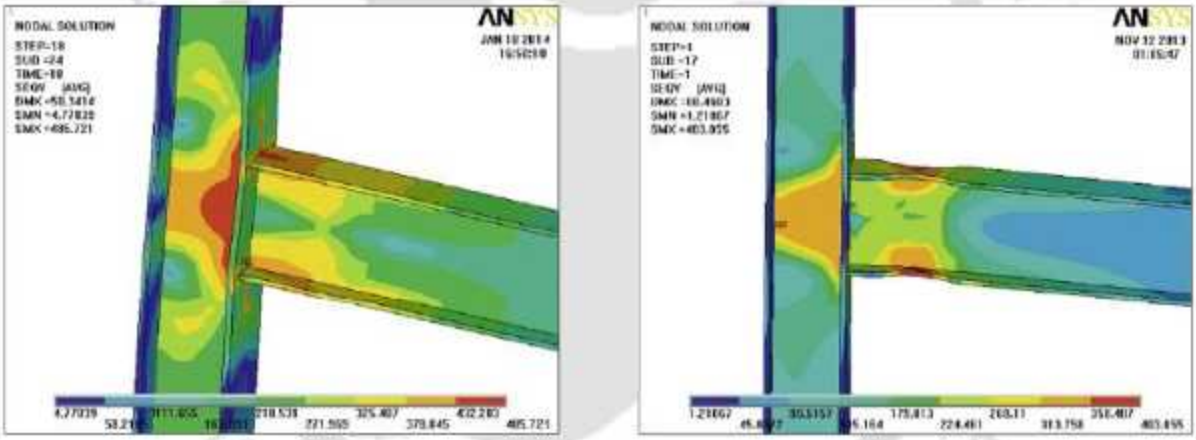

Fig. 2.10 stress contours: (a) Regular steel beam connection (b) RBS connection [71]

Morshedi *et al.* [84] carried out the numerical study on seismic behaviour of double reduced beam section (DRBS) subjected to cyclic loadings. These analyses suggest that connection ductility got enhanced in case of DRBS connection. The parametric study on the DRBS connection revealed that it increased the deformation capacity up to 40%, as compared to that of the common reduced beam section connection. Moreover, adding a second cut to ordinary RBS connection distributed the strains over the two reduced beam sections. It helps to reduce the equivalent plastic strain at the reduced sections. It was reported that the depth of cut of the RBS are the most influential geometrical design parameter, which effects the energy dissipation capacity and ductility.

Parvari *et al.* [89] studied first numerical study on drilled cut RBS using finite element software ABAQUS. Twenty-four nos. of numerical models were studied to find the different seismic parameters.

Based on the parametric study, it was reported that types and number of holes significantly affect the ductility of the connection and decrease stress concentration in the area of beam-column connection. It was reported nos. of hole effectively increased the plastic hinge length. The parametric study on the RBS connection also revealed that it increased the deformation capacity up to 10%, as compared to that of the common reduced beam section connection. Results of this paper proved that performance of drilled cut RBS better as compared to other RBSs.

Li *et al.* [92] proposed an analytical model for RBS-CFT using OpenSees. A simplified rotational spring were used to find the force displacement behaviour. The stiffness of rotational spring was calculated based on experimental results of simple beam-column connection. The results of numerical model showed that it can simulate the experimental results quite well.

Nia *et al.* [93] developed the 3D finite element models which were validated using two sets of experimental studies on sloping RBS. Based on the results, slope angle and beam depth were found to be the most significant factors influencing all the response variables. Both beam slope angle and beam depth inflenced the cyclic response characteristics. RBS connections with smaller beam slope angle and beam depth experience lower strain demands and potential for fracture.

Sofias *et al.* [77] performed the numerical simulation on two radius cut RBS specimens. Numerical study was conducted in order to provide a safe assessment for the RBS application in European steel profiles. Different parameters were calculated from the numerical results. It was found that experimental and finite element analysis results matched quite well.

Horton *et al.* [94] carried out an extensive parametric analysis on 90 number of different RBS specimens in order to find the geometrical parameters which effects the design parameters of RBS connections including, Yield Moment, Peak Moment, Ultimate Rotation, Ductility and Energy dissipated capacity. It was reported that the depth and width of the RBS cut are the most influential

geometrical design parameters, affecting up to 30% changes in the performance as compared to those of a full beams section. Finally, based on the results of this study, practical design equations are proposed to predict the seismic performance of RBS connections.

2.8 Research gaps

Implementation of RBS-CFT connection in moment resisting frames improved their overall seismic performance. However, the application of RBS concept is not very common in India. Therefore, the study related to different types of RBS-column connection are required for their installation in the steel moment resisting frames. Emphasizing advantages and usefulness of application of the RBS concept in the moment resisting steel frames are needed. Following gap areas are identified based on critical review of the previous research works.

- It was reported that higher out-of-plane deformation of the beam was observed in case of radius cut RBS, due to larger depth of cut, decreased the effectiveness of radius cut RBS. Therefore, it is necessary to develop new types of RBS in order to reduce the out-of-plane deformation and to ensure stable hysteretic behaviour with enhanced energy dissipation capacity.

- Experimental studies on varies types of RBS were conducted to evaluate the seismic performance. Most of these studies concentrated on seismic evaluation of either constant or radius cut RBS. The literature review indicated that although extensive experimental investigations were carried out to understand the behavior of shaved cut RBS, yet very few records could be found covering the experimental studies on drilled cut RBS.

- Majority of the connections have been made using various types of welding, stiffeners, and diaphragm. In almost all prior experiments, radius cut RBS was employed to connect *I* or *H*-shaped steel column. There is still lack of information on performance of RBS-CFT with bidirectional bolts for moment-resisting frames.

- Most of the available research classified regular steel beam- CFT connections as rigid. No RBS-CFT connection has been studied to determine if it was a rigid or semi-rigid connection. There are very limited studies on RBS-CFT semi-rigid connections using bidirectional bolts for achieving higher ductility under cyclic loading.

- FE analysis of RBS-CFT connection with bidirectional bolts are very challenging tasks. It requires proper modelling, including characterization of material and interaction properties. There were very limited studies on finite element modelling to simulate the hysteretic behaviour of RBS-CFT connections with bidirectional bolts under cyclic loading considering multiple interactions.

- Development of fragility curve are needed for the assessment of seismic vulnerability. Very few studies on seismic vulnerability were found for the MRFs where RBS was used.

2.9 Concluding Remarks

In this chapter, a large number of studies on steel moment resisting frames were reviewed critically. Different types of damages in the welded connections responsible for their poor performance during Northridge earthquake (1994) were highlighted. Modification of the connections for the overall improved performance during high intensity earthquake were studied. Benefits of CFT column were highlighted. Performance of the different types of connections (welded, bolted) were critically reviewed to understand their overall seismic behaviour. Large nos. of experimental and numerical studies on RBS, CFT and steel beam-CFT connection were critically reviewed. Efforts were made given to find the gaps in the state-of-the-art on bolted RBS-column connection. Finally, the gap area was identified based on the detailed studies of literature.

CHAPTER-3
Details of test specimens, Test setup and Instrumentation

CONTENTS

3.1 Introduction

In this chapter, characterization of material samples from steel tube, *I*- beam and bolts used for fabrication of RBS-CFT connection were discussed first. Design of concrete mix as well as evaluation of mechanical properties are crucial for design and fabrications of test specimens. The mix design was carried out as per provision of relevant standard codes. All the constituent materials such as cement, fine aggregates, coarse aggregates were tested. In order to evaluate the tensile strengths of steel beam, column and tube, standard coupons were made and the coupons were tested. Four different types of RBS specimens were designed as per provisions of relevant standard codes and papers. This RBS specimens were used for performance evaluation of RBS-CFT connections in this study. Geometrically scaled specimens of RBS-CFT connection with four different types of RBSs-CFT connections were tested in this experimental programme. Description of the test set-up along with details of instrumentation has also been furnished here.

3.2 Identification of specimen

It was observed that during severe earthquakes, the exterior connections had suffered more damage in comparison to the interior ones. Seismic performance of exterior RBS-CFT connection would

be evaluated in the present study. A typical exterior RBS-CFT connection of frame with location of points of inflexion found nearly at the mid-points of beams and columns under the action of lateral loading is shown in Fig. 3.1. It comprised of half of a column at top and bottom as well as half of a beam.

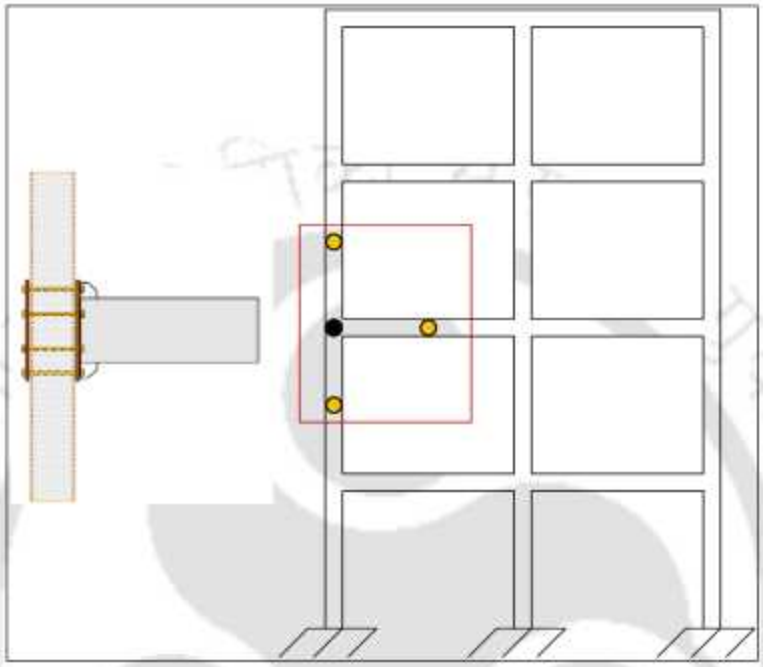

Fig.3.1 Isolated exterior RBS-CFT connection

Symmetric boundary condition was maintained at both the ends of column for isolation of a single unit of beam-column connection. In this study, a typical geometrically scaled model column for isolation identical building with floor to floor height as 2200 mm and the beam of 1000 mm effective span was considered. The present study was limited to seismic performance evaluation of an external beam-column connection as shown in Fig. 3.1.

3.3 Concrete mix for CFT

Concrete mix was used to fill the CFT column. Concrete mix designed was done as per IS: 10262-1982 [95] in order to arrive at the desired target cube strength. Ordinary Portland cement of 53 grade was used. Cement, fine aggregates and coarse aggregates were proportioned to achieve M30 grade of concrete. In this present study, target strength refers to the characteristic strength of the

concrete obtained from the 28 days compressive strength of concrete cubes of size 150 mm x 150 mm x 150 mm. Eighteen nos. of concrete cubes have been cast during fabrication of CFT. Compressive strength of the concrete (f_{ck}) is obtained from compression testing of the cubes. Elastic modulus (E_c) and tensile strength (f_t) of the concrete have been calculated using f_{ck} as per clause nos. 6.2.3.1 and 6.2.2 of IS 456 (2000) respectively. The values of elastic modulus and tensile strength are furnished in Table 3.1

Table 3.1: Material properties for M30 concrete (unit: MPa)

Grade of concrete	f_{ck}	E_c	f_t
M30 (Standard condition at 28 days)	32.57	2.8×10^4	3.99

Coarse aggregate size used for the concrete mix were 10 mm down. All the aggregates used were angular and well graded. Thus, three numbers of mix designs were done for target strength of 30 MPa. The sand used for making concrete conforming to zone-II as per IS: 383-2002 [96]. The details of material properties used in the mix designs are furnished in the Appendix A.

3.3.1 Cement tests

OPC 53 grade cement was used for casting the concrete specimens, and no chemical admixtures were used. The cement was tested for its standard consistency, initial setting time, specific gravity and compressive strength following relevant Bureau of Indian Standard (IS) codes. The details of test results are presented in the Appendix A. Further, compressive strength of the cement was determined as per provisions of IS: 4031(6) [97]. The values of compressive strength found from compression test as per IS:12269 [98] are shown in Appendix -A. It was ensured that the cement used satisfied the compressive strength criteria of 53 grade cement.

3.3.2 Fine aggregate tests

The fine aggregate (sand) was procured from a locally available source. The specific gravity of the sand was found to be 2.51 as per the provisions of IS: 2386(III) [99]. Further, the sieve analysis of

sand was carried out as per IS: 2386(1) [100]. The percentage weight retained in the sieves is shown in Appendix A. Finally, the zone to which sand sample belong was ascertained.

3.3.3 Coarse aggregate tests

The nominal sizes of well graded coarse aggregate used were 10 mm down for concrete specimens. The specific gravity of aggregate was found to be 2.62 as per the provisions of IS: 2386(III)-1963. The sieve analysis of aggregates was carried out as per IS: 2386(1) [101]. Results of typical sieve analysis is shown in Appendix-A. The fineness modulus of aggregate was found to be 8.06.

3.3.4 Concrete mix design

Concrete mixing was done using a horizontal pan concrete mixer. Details of three concrete mixes designed in this study are furnished in Table 3.2. CFT specimens were placed in the vertical position, and a high-frequency needle vibrator was used to consolidate the concrete during filling into the CFT column. The same mix proportion was used for all the specimens. The specimens and the compression cubes were left to cure in the ambient temperature and humidity.

Table 3.2 Details of concrete mixes

SL. No.	Target strength (N/mm)	Nominal size of coarse aggregates	Mix ratio	w/c ratio	Average compressive strength (N/mm)
1	30	10 mm down	1:1.72:2.69	0.57	32.6
2	30	10 mm down	1:1.72:2.69	0.57	32.2
3	30	10 mm down	1:1.72:2.69	0.57	31.6

3.4 Steel coupon tests

Tension tests were conducted using servo-controlled universal testing machine (UTM) of maximum capacity 250 kN and the stroke length of 160 mm (Make: BISS, Model: medium 250). Test coupons were prepared from the flanges and webs of the steel beams (NPB 250 x 125 x 6 x 9),

and tubes (SHS 220 x 220 x 6) and bolts (M16, 10.9 Grade) for evaluation of their tensile strength of steel. Fig. 3.2 showed the dimensions of a typical beam and tube coupon sample.

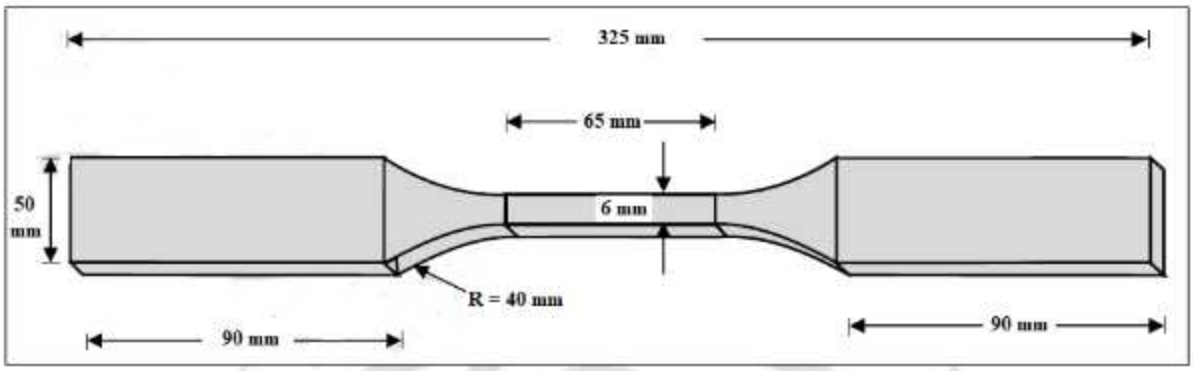

Fig.3.2 Details of the test coupon

Fig.3.3 Test set up for coupon test

The mechanical properties of the steel were calculated in accordance procedure prescribed in the ASTM E8/E8M-13a [102]. Test set up for the coupon test are shown in the Fig.3.3. Values of the yield strength (f_y), ultimate strength (f_u) and Young's Modulus (E_s) of the steel in each component were obtained by testing three coupons. The strain rate for the uniaxial tension test

was kept at 1mm/min. The photograph of the test setup is shown in Fig.3.3. Mechanical properties obtained from the coupons made from the different components of the RBS-CFT connections are furnished in the Table 3.3. Tensile stress-strain plots of bolts, beams and tube are shown in Fig. 3.4.

Table No.3.3: Mechanical properties of steel

Material Sample		Thickness	f_y	f_u	E_s	elongation
		(mm)	(MPa)	(MPa)	(MPa)	(%)
NPB 250	flange	9	352	471	2.02×10^5	10
	web	6	373	538	1.92×10^5	11
SHS 220	flange/web	6	376	665	1.96×10^5	14
10.9 Grade bolt M16	bolt	16	972	1119	2.09×10^5	16

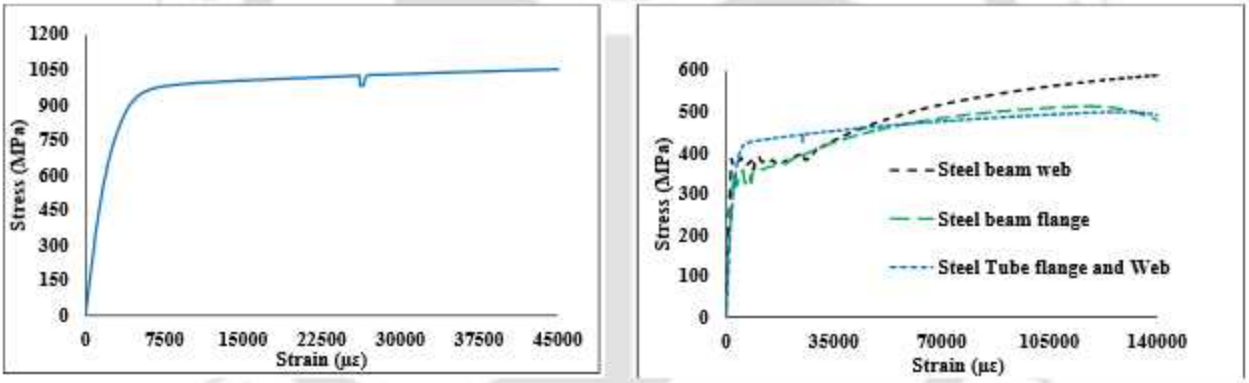

Fig.3.4 Stress-strain curves for: (a) bolt specimen (b) beam and tube specimen

3.5 Design principle of RBS specimens

RBS test specimens are designed to ensure formation of plastic hinges in beams of the steel frame buildings subjected to seismic loading. Conventional radius cut RBS are designed as per procedure prescribed by Engelharth et al. [7] and ANSI/AISC 358-16 [103]. Where as drilled cut RBS are designed as per guidelines prescribed by Vetr. et al. [6]

Linear profile of the proposed *V*-cut RBS is nearly similar to the variation of bending moment under lateral load in the RBS zone 1-3 as shown in Fig.3.5. This profile would ensure almost simultaneous yielding of 1-3 zone of the RBS for achieving higher plastic rotation. Further, this

unsymmetrical profile also needs lower depth-of-cut and hence lateral out-of-plane deformation of the beam is likely to reduce. Further, higher level of energy dissipation is expected in V-cut RBS-CFT connection as compared to that of the conventional radius cut RBS.

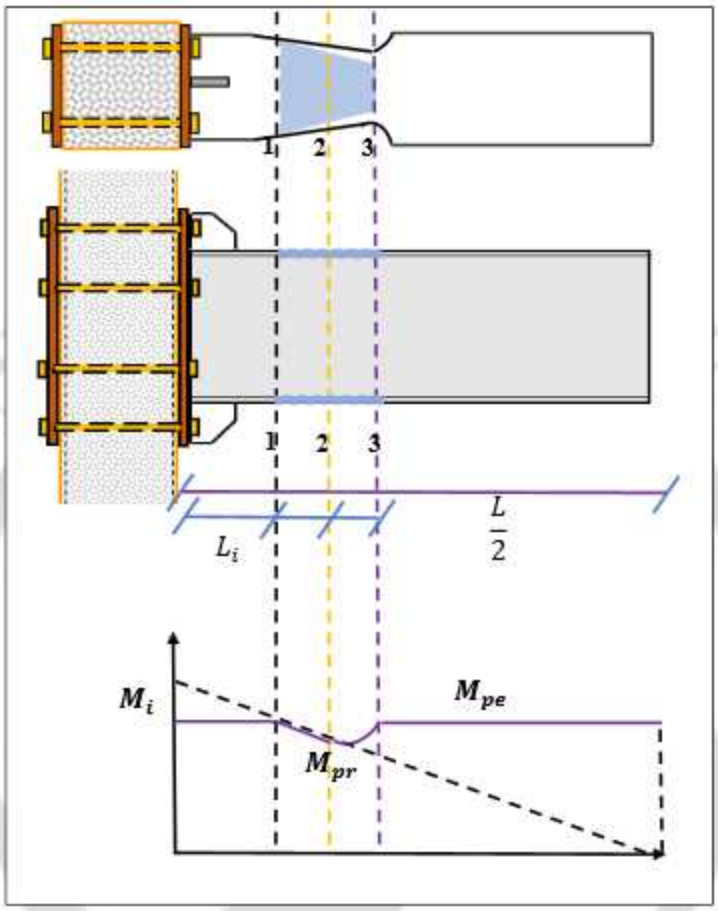

Fig.3.5 Moment gradient of *V*-cut RBS Connection.

Distribution of the flexural demand and capacity of the proposed *V*-cut RBS is shown in Fig.3.6 Ratio of bending moment M_i at any section in the RBS and corresponding section modulus which is used for estimation of depth of cut of the RBS can be expressed by the following equation.

$$\frac{M_1}{Z_1} \cong \frac{M_2}{Z_2} \cong \frac{M_3}{Z_3} \cong \frac{M_i}{Z_i} \tag{3.1}$$

$$M_i = \alpha M_{pr}\left(\frac{\frac{L}{2}-L_i}{\frac{L}{2}}\right) \tag{3.2}$$

$$M_{pr} = C_{pr} R_y F_y Z_e \tag{3.3}$$

$$C_{pr} = \frac{F_u + F_y}{2F_y} \leq 1.2 \tag{3.4}$$

$$Z_i = Z_p - 2D_i t_f (\text{d-}t_f) \tag{3.5}$$

where, $\alpha = 0.85$ to 1, R_y = ratio of the expected yield stress to the specified minimum yield stress; F_y = yield stress, D_i = depth of the cut at different section of the beam, Z_e = plastic section modulus at the location of plastic hinge, C_{pr} = Factor to account for peak connection strength, Z_p = plastic section modulus of steel beam, M_{pr} = Maximum moment of RBS section. F_u = ultimate stress, Z_i = Plastic section Modulus at different section, $L/2$ = length of the beam, d = beam depth, L_i = distance of different section from column end, t_f = thickness of flange, M_{pe} = Maximum moment of full beam section.

Panel zone of the CFT column was designed, to remain in elastic condition, as per recommendation of Wu et al. [17]. High strength friction grip (HSFG) bolts, used for semi-rigid bidirectional bolted connection, are also designed to remain in elastic condition. Thus, RBS-CFT connection was designed to facilitate yielding only in the RBS region.

3.6 Description of the specimens

In this experimental investigation, four sets of geometrically scaled RBS-CFT connections with bidirectional bolts were tested under cyclic loads for assessment of their seismic behaviour. Details of four sets geometrical scaled RBS-CFT exterior connections test models, considered in this study are shown in Fig. 3.6 to Fig. 3.9. First set of connection are fabricated with conventional radius cut RBS while second set of connection is made with new *V*-cut RBS. Third set and fourth set are constant drilled cut (*CD*-cut) and varied drilled cut (*VD*-cut) respectively.

Each connection is fabricated using a narrow parallel flanged beam, NPB250 (IS 12778), [104] with effective length of 1000 mm and a concrete filled square tubular column, SHS220 (IS 4923) [105] with effective length 2200 mm. *M*30 grade concrete was used to fill the tube. Geometrical details of shaved cut RBS and drilled cut RBS are given in Table 3.3 and Table 3.4 respectively. In each of these connections, CFT and RBS are connected using two end plates and bi-directional

bolts as shown in Fig. 3.6 to Fig. 3.9. One end plate is welded with one end of the beam using 6 mm fillet weld. High strength friction grip (HSFG) bolts of size *M*16 and grade 10.9 are used for connecting two components of the connections. Torque wrench, with appropriate specification, is used for tightening the bolts.

Table No.3.4: Geometrical details of the shaved cut specimens

RBS	Beam*	Column**	Geometrical details (mm)		
			a	*b*	*c*
Radius-cut-I/II	NPB 250 x 125 x 9 x6	SHS 220 x 220 x 6	$0.50b_f = 62.5$	$0.75d = 187.5$	$0.23b_f = 28.5$
V-cut-I/II	NPB 250 x 125 x 9 x6	SHS 220 x 220 x 6	$0.50b_f = 62.5$	$0.75d = 187.5$	$0.14b_f = 17.0$

*NPB-Narrow Parallel flanged beam (IS 12778-2004), **SHS section (IS 4923-1997). all dimensions are in mm

Table No.3.5: Geometrical details of the drilled cut specimen

RBS	Beam*	Column**	Drilling details (mm)		
			Sec 1-1	*Sec 2-2*	*Sec 3-3*
CD-cut	NPB 250 x 125 x 9 x 6	SHS 220 x 220 x 6	12 ϕ	12 ϕ	12 ϕ
VD-cut	NPB 250 x 125 x 9 x 6	SHS 220 x 220 x 6	10 ϕ	12 ϕ	14 ϕ

*NPB-Narrow Parallel flanged beam (IS 12778-2004), **SHS section (IS 4923-1997). all dimensions are in mm.

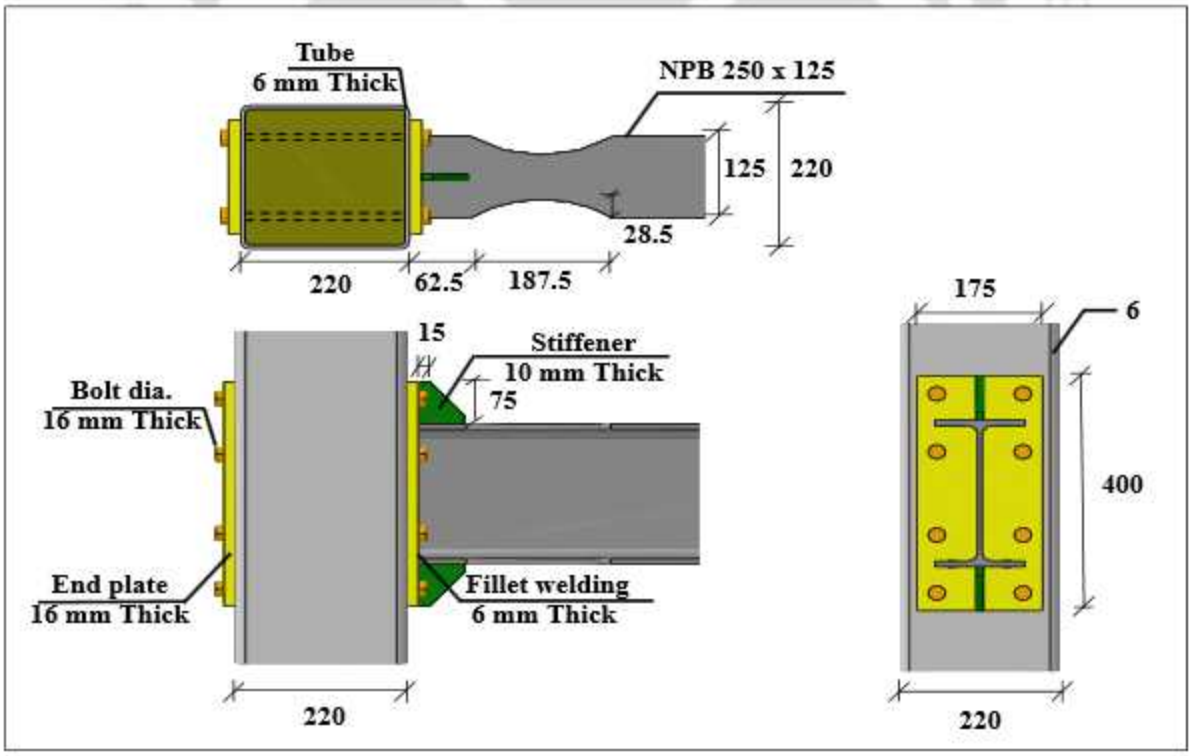

Fig.3.6 Radius cut RBS-CFT connection details

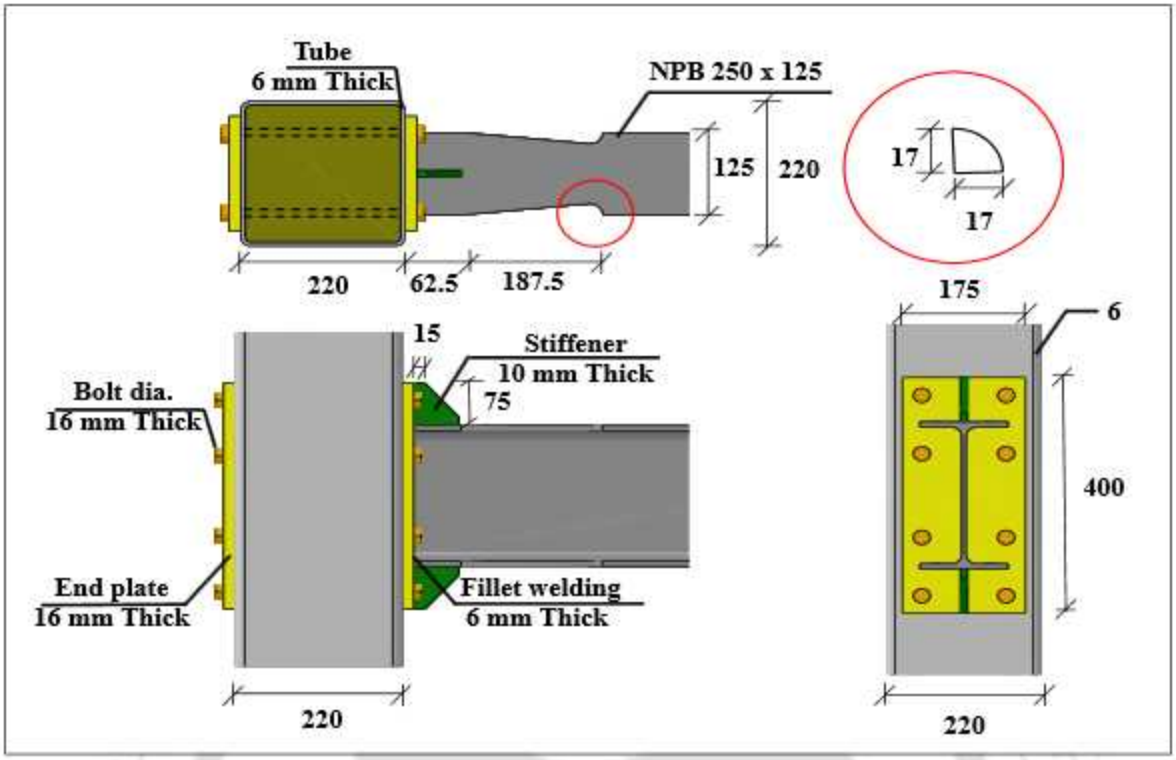

Fig.3.7 *V*-Cut RBS-CFT connection details

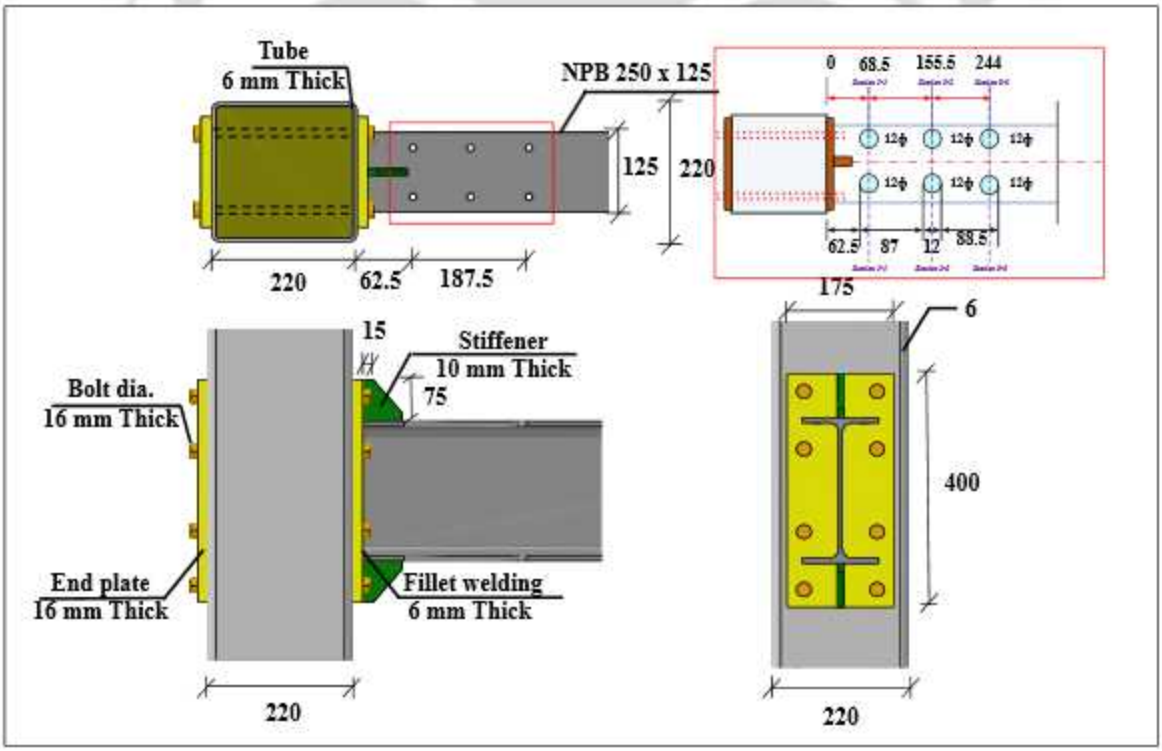

Fig.3.8 *CD*-Cut RBS-CFT connection details

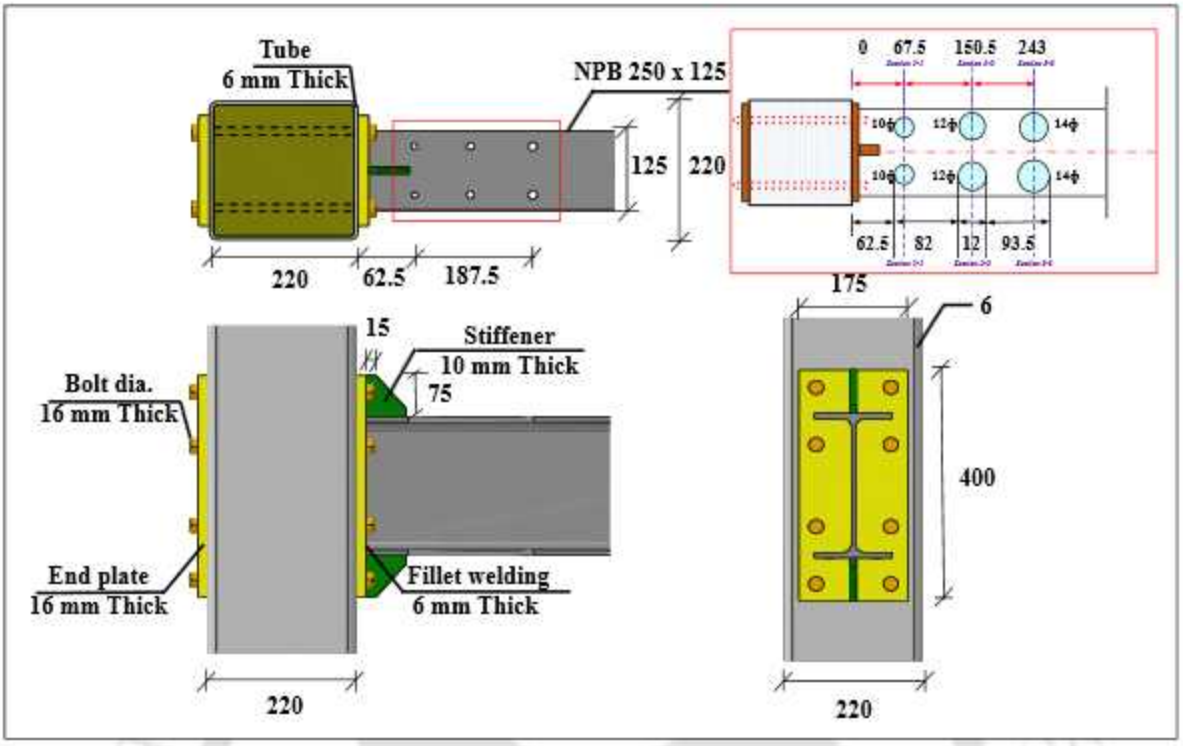

Fig. 3.9 *VD*-Cut RBS-CFT connection details

3.7 Test set up

Photograph of the test setup and schematic diagram of the test set-up used are shown in Fig. 3.10. MTS actuator (Make: MTS, USA, Model 244.31) of 250 kN capacity and ±250 mm stroke length fixed in vertical strong floor horizontally. "*A*" type of frame was fixed with horizontal strong floor to hold the hydraulic jack. Hydraulic jack was used to apply the axial load into the CFT column. The column was placed in horizontal position while the beam was placed in vertical position in the set-up. Two specially built steel post were placed on either side of the test specimen to avoid an accidental out-of-plane deformation of the RBS-CFT connections. An axial load of 10% of gross capacity of column was applied to the column to represent gravity load. Axial load on column was applied by a 500 kN capacity hydraulic jack. The jack was abutting against the "A" frame, which was fabricated for the required load carrying capacity. To simulate support condition at both ends of the column, roller supports were fabricated by making grooves inside mild steel plates. The servo-hydraulic actuator is of double ended and double stroke type which is equipped with internal load cell and LVDT for measurement of applied load and displacement respectively.

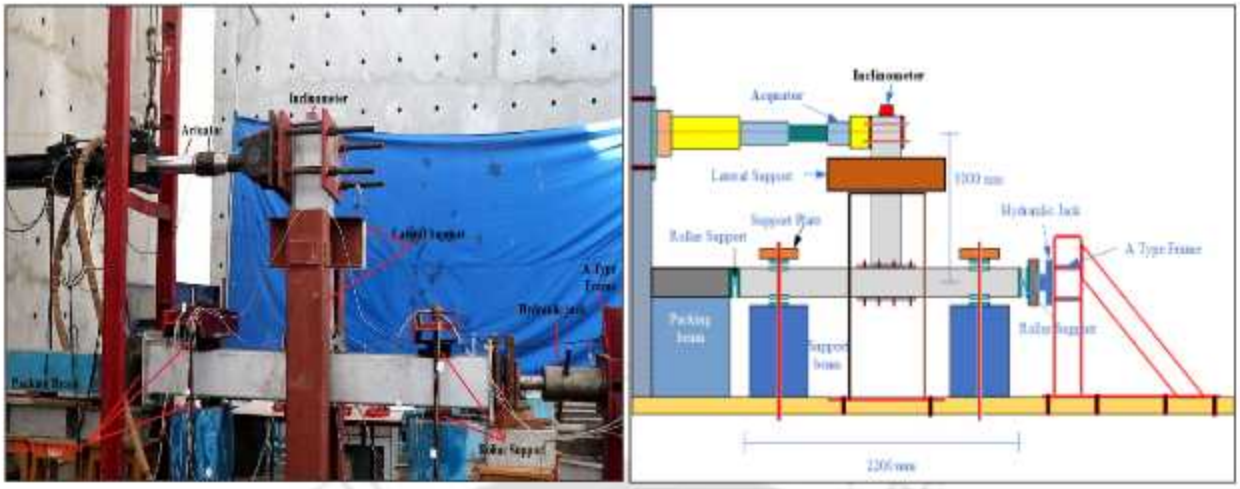

(a) (b)

Fig.3.10 Test set-up: (a) photograph, (b) schematic diagram

3.8 Instrumentation

Two types of strain gauges are used to measure the strain values at different locations of RBS-CFT connection during experimental study. An inclinometer was used to measure the beam rotation. Details of the all the sensors are described in following subsection.

3.8.1 Strain Transducer

Panel zone area of column (CFT) are instrumented with strain gauges to record the strain values during experiments. Four reusable strain transducers (make: BDI, USA, Model: ST-350) are attached to panel diagonally, as shown in Fig. 3.11. Specification of the strain transducer are given in Table 3.5.

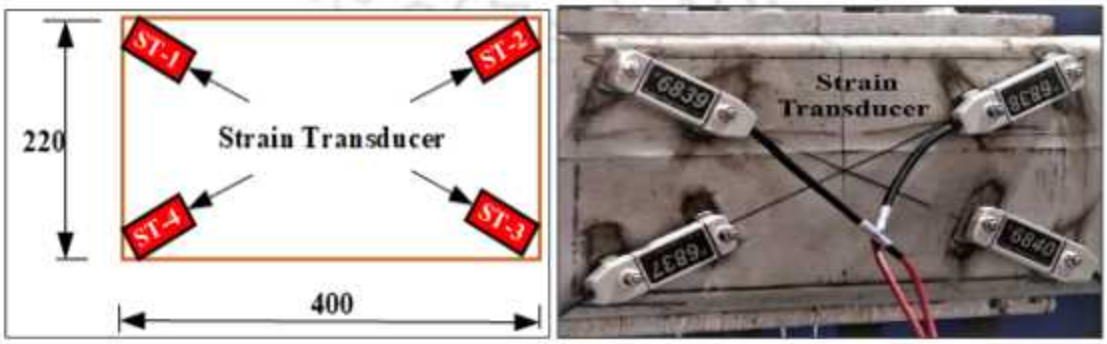

Fig.3.11 Strain transducer arrangement in CFT panel zone

3.8.2 Strain Gauge

Foil type electrical strain gauges were pasted to the test specimens. Detailed specifications of electrical strain gauge in the Table 3.5. Each strain gauges were connected to a "wheatstone" quarter-bridge configuration. Electrical resistance strain gages were pasted in the RBS zone of the connection along the longitudinal direction of the beam to record the distribution of strain along the length. Four nos. of electrical strain gauges (make: TML, Japan, Model: Type FLA-6-350-11-1L) having resistance 350 Ω and gauge length 6 mm are employed in radius cut RBS.

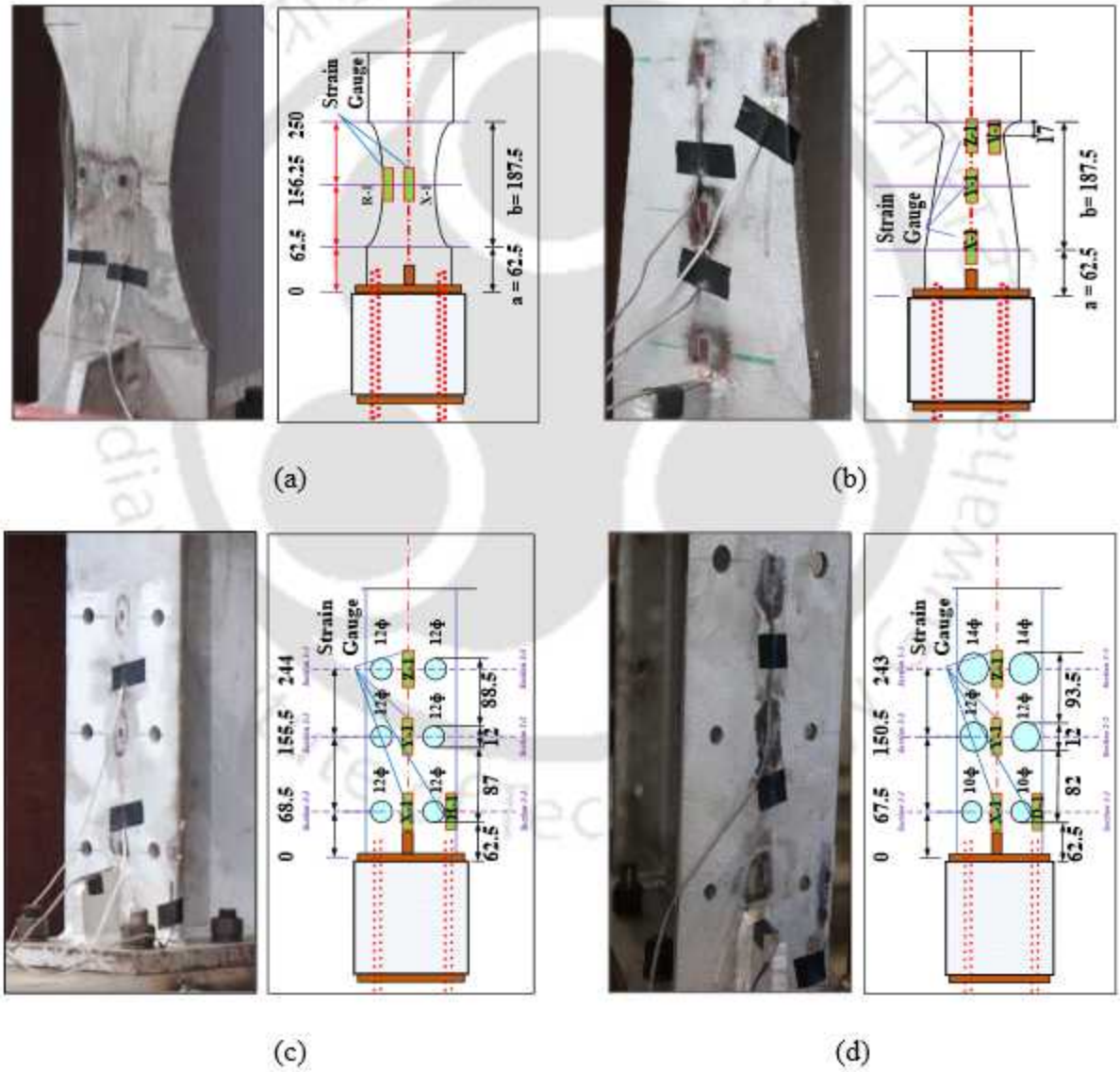

Fig. 3.12 Location of the strain gauge in RBS zone: (a) Radius cut RBS (b) *V*-cut RBS (c) *CD*-cut RBS (d) *VD*-cut RBS

Whereas eight nos. of strain gauges RBS are used for *V*-cut-RBS, *CD*-cut-RBS and *VD*-cut-RBS respectively. Locations of strain gauges, for all the radius cut RBS are shown in Fig.3.12. *X1, R1* represents locations of the strain gauges s in the front flange whereas *X2, R2,* represents locations of the strain gauges s in the back flange. Similarly, locations of all the strain gauges, for the front flange of *V*-cut RBS, *CD*-cut RBS, *VD*-cut RBS are also shown in Fig. 3.13. Acquisition of the strain values is carried out using a DAQ (make: HBM, Germany, Model: MGC plus) of 20-bit resolution. A sampling frequency of 100 Hz was considered for all the experiments.

Table 3.6: Specifications of different types of strain sensor

Sensor Types	Strain Transducer	Strain gauge
Manufacturer	BDI, USA	TML, JAPAN
Designation	ST 350	FLA-6-350-11-1L
Gage Length	76.20 mm	6 mm
Gage Factor	2.11±0.5%	2.13±1%
Resistance	350 Ω	350 Ω
Temperature Range	-50^0 C to + 80^0 C	-20^0 C to + 80^0 C
Strain Limit	±4,000 $\mu\varepsilon$	±50000 $\mu\varepsilon$

3.8.3 Inclinometer

An inclinometer (make: HBM, Germany, Model: MEAS, NS-5/P) was used to measure beam rotation. The rotational capacity of the inclinometer is ± 0.087rad ($\pm 5^0$). Photograph of inclinometer are given in Fig. 3.13.

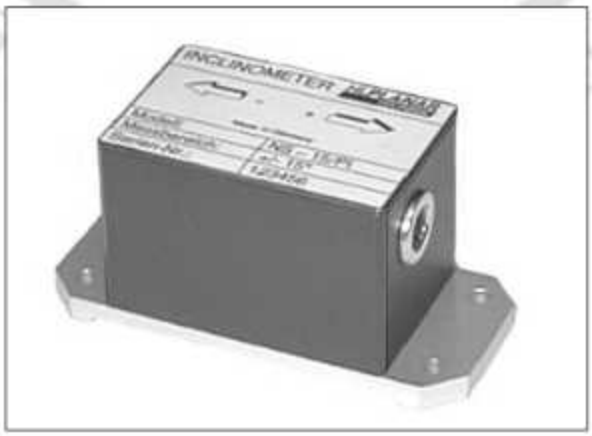

Fig.3.13 Inclinometer Photograph

3.9 Concluding remarks

In this chapter, experimental tests on cement, fine aggregate and coarse aggregate for evaluation of their mechanical properties are reported. Details of design of concrete mix of grades *M30* is also presented. A detailed description of the tensile test of all steel materials are furnished. Design principles of *V*-cut RBS specimens are outlined along with design procedure for radius-cut RBS, *CD*-cut RBS and *VD*-cut RBS. Detailed description and detailing of four different types of RBS-CFT connection with bidirectional bolts are presented. Details of the experimental test setup and specifications of different types of sensors used in this present study are also discussed. Finally, details of the test set-up used for cyclic test of RBS-CFT connection with bidirectional bolts under cyclic loading are highlighted.

CHAPTER-4

Experimental Study of Shaved cut RBS-CFT Connection with bidirectional bolts

CONTENTS

4.1 Introduction

The experimental results and discussion on behavior of two types of shaved cut RBS (radius cut, *V*-cut) and CFT connections with bidirectional bolts are reported in this section. Two specimens of each types of connections were tested under simultaneous action of axial load in CFT and cyclic load at the beam ends. A constant axial load of 10% of gross capacity of the column was applied during the application of cyclic displacements at the time of testing. The recorded data were used to study hysteresis behaviour, envelope curves, variation of stiffness, classification of connections, energy dissipation, ductility and damping with respect to rotation or displacements. Force-displacement hysteresis loops of both the specimens of each types are presented. The mechanical characteristics of both the specimen of each types are presented here. Detailed discussions on experimental behavior of both type of specimens are furnished in the following sub-sections. Comparisons of test results for radius cut and *V*-cut were made in term of all above-mentioned parameters and finally conclusions were drawn.

4.2 Cyclic test loading protocol

A horizontal loading protocol under displacement control mode, as shown in Fig. 4.1, was applied using a 250 kN capacity dynamic servo-hydraulic actuator (make: MTS Inc., USA, Model 244.31) having a stroke length of ± 250 mm. Applied displacement protocol, as prescribed by AISC 341-10, is a sequence of triangular cyclic displacement history with displacement amplitudes of U = ±3.75 mm, U = ±5 mm, U = ±7.5 mm repeated six times; displacement amplitude of U = ±10 mm repeated four times, and displacement amplitudes U = ±15 mm, ±20 mm, ±30 mm and ±40 mm repeated two times. Cyclic test was stopped as soon as the horizontal displacement amplitude of the beam reached 40 mm. Application of command protocol through the servo-hydraulic actuator and acquisition of feedback signal are carried out using the controller (make: MTS Inc., USA, Model: FlexTest-GT).

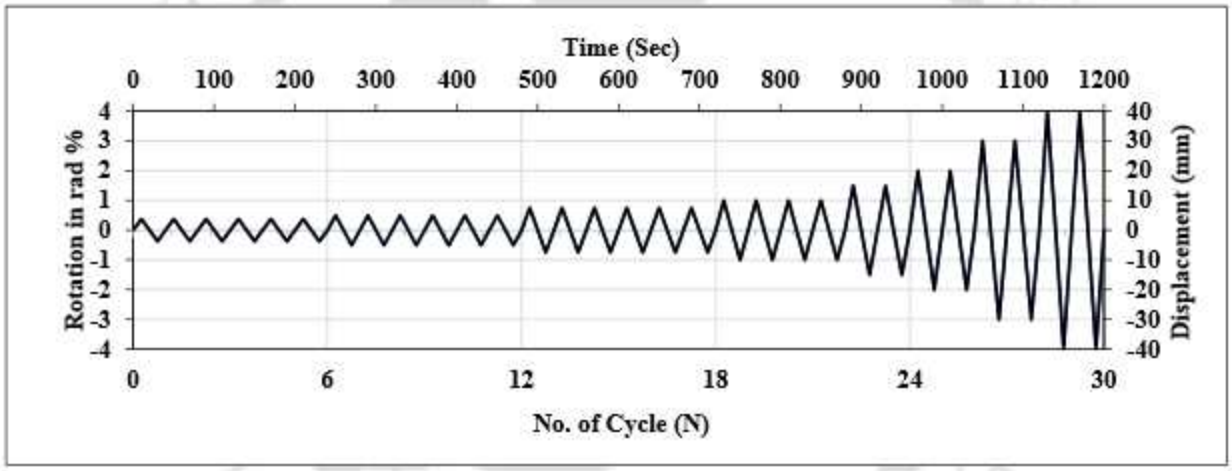

Fig. 4.1 Loading protocol in the experimental program.

4.3 General Observation

The experimental results and discussion on behavior of two types of RBS (radius cut, *V*-cut) and CFT connections with bidirectional bolts are reported in this section. Both types of the test specimens attained maximum rotation of 0.04 rad as per AISC 341(2016) criteria for composite special moment resisting frames. Force displacement hysteresis behavior of both types of specimens (radius cut, *V*-cut) exhibited stable ductile behavior during cyclic test. The plastic hinges are formed in the RBS region as expected. The column and panel zone area remained

elastic at all times. Therefore, same CFT was used in all the test specimens. Detailed discussions on experimental behavior of both type of specimens are furnished in the following sub-sections.

4.3.1 Visual Observation of Radius-cut RBS-CFT connection

The test arrangement of RBS-CFT connection of radius cut and *V*-cut RBS specimens are already shown in chapter 3. A close view of the damaged specimens at end of cyclic test of radius cut RBS are shown in Fig.4.2. Load-displacement hysteretic loops of both radius cut specimens are shown in Fig.4.3 and Fig.4.4. The plastic hinge formed mainly in the radius cut RBS region away from the column and panel zone. The specimen yielded at a rotational angle of 0.015 rad. Plastic hinges were formed on both the flanges during the 23rd and 24th loading cycle after beam rotation of 0.015 radians. Flakes of the silver colour paint got separated from narrowest part of flange first at 0.015 rad rotation as shown in Fig.4.2. It was observed that yielding spread to adjoining region of reduced zone at rotation of 0.02 rad. The strain gauge data, as indicated in the section 4.8, also confirmed these observations. The loading was stopped at 40 mm displacement corresponding to beam rotation of 0.04 rad.

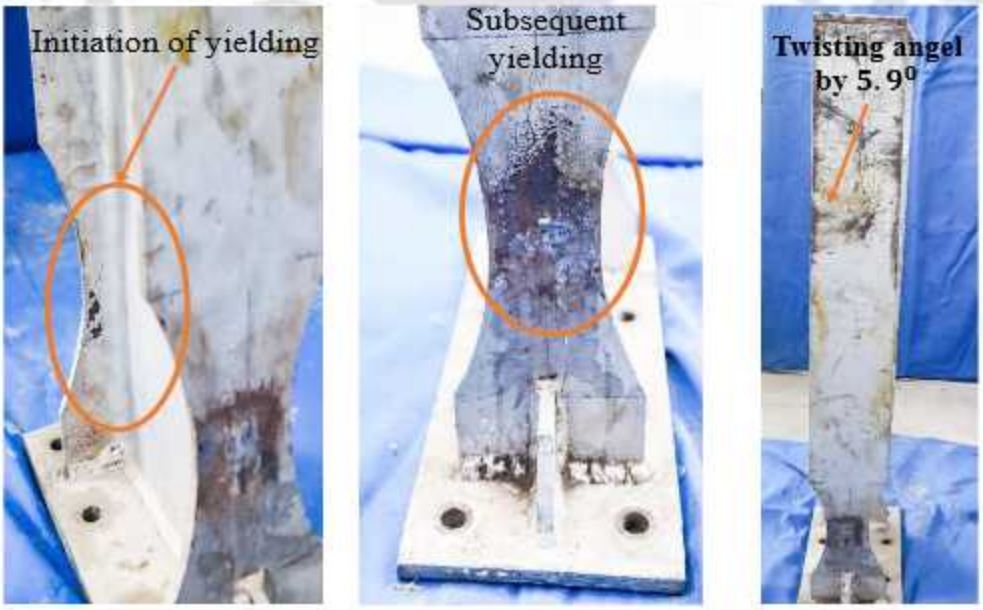

(a) (b) (c)

Fig. 4.2 Visual observation of different damage states for Radius-cut RBS at various rotation: (a) 0.015 rad (b) 0.02 rad (c) 0.04 rad

It was observed that the radius cut RBS experienced residual twist of 6° about longitudinal axis of the beam. Twisting of beam, due to eccentricity between line of action of cyclic load and center line of the web, could not be restrained by the lateral supports. However, there is no apparent yielding to the CFT and bolts during the entire test. Thus, formation of plastic hinge in the radius cut RBS-CFT connections is observed only in the reduced beam section.

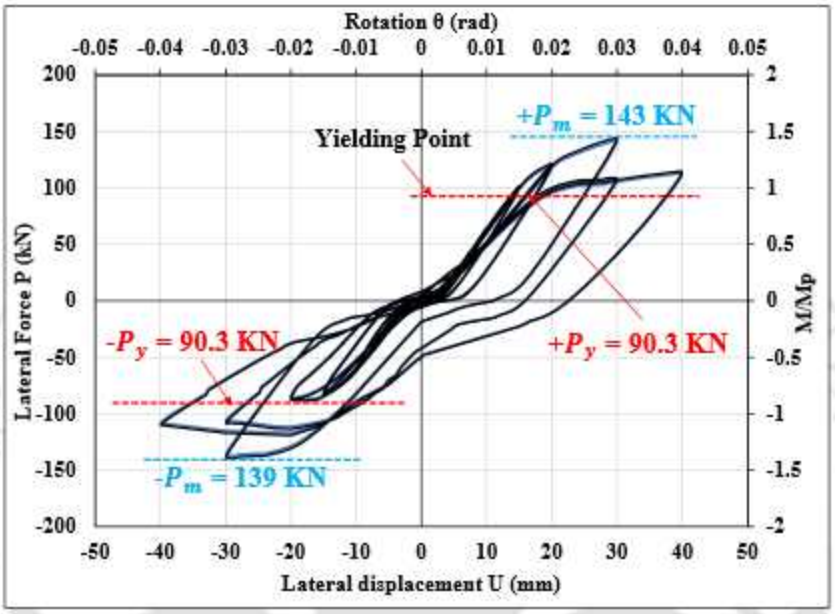

Fig. 4.3 Hysteresis loops of radius cut-I RBS-CFT connection

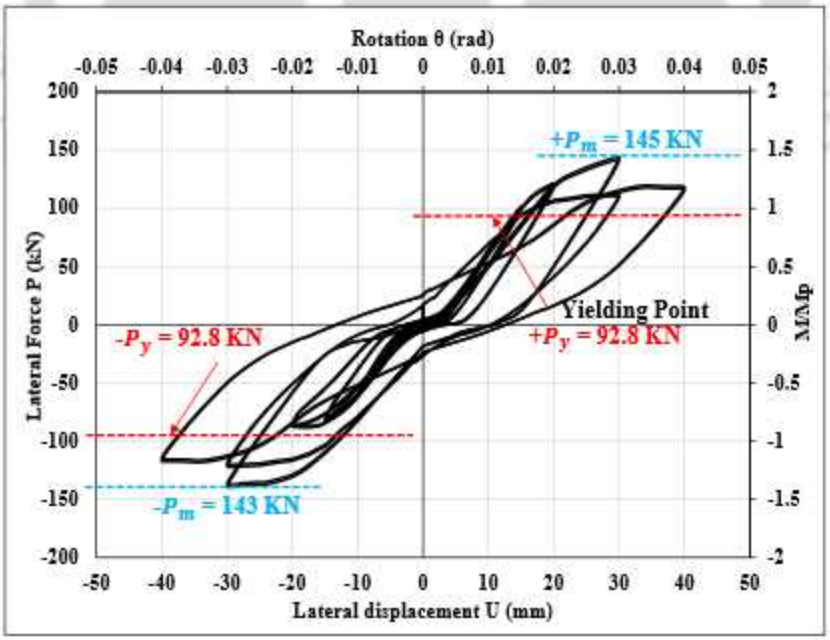

Fig. 4.4 Hysteresis loops of radius cut-II RBS-CFT connection

4.3.2 Visual Observation of *V*-cut RBS-CFT Connection

The damage specimens at end of cyclic test *V*-cut RBS are shown in Fig.4.5. Load-displacement hysteretic loops of both the *V*- cut specimens are shown in Fig.4.6 and Fig.4.7. The plastic hinge formed mainly in the *V*- cut RBS region away from the column and panel zone. The specimen yielded at a rotational angle of 0.015 rad. Plastic hinges were formed on both the flanges during the 23rd and 24th loading cycle after beam rotation of 0.015 radians. Flakes of the silver colour skins got separated from reduced part of flange first corresponding to 0.015 rad rotational angle as shown in Fig.4.6. The strain gauge data, as indicated in the section 4.8, also confirmed these observations. It was observed that minor cracks originated between endplate and beam at a rotational angle of 0.02 rad. The loading was stopped at 40 mm displacement corresponding to beam rotation of 0.04 rad. The final angle of twist for *V*-cut beams is about 2°. Due to the smaller depth of cut, the angle of twist of this specimen is observed to be lesser than that in the beam with radius cut RBS. Twisting of beam due to eccentricity between line of action of cyclic load and center line of the web, could not be restrained by the lateral supports. However, there is no apparent

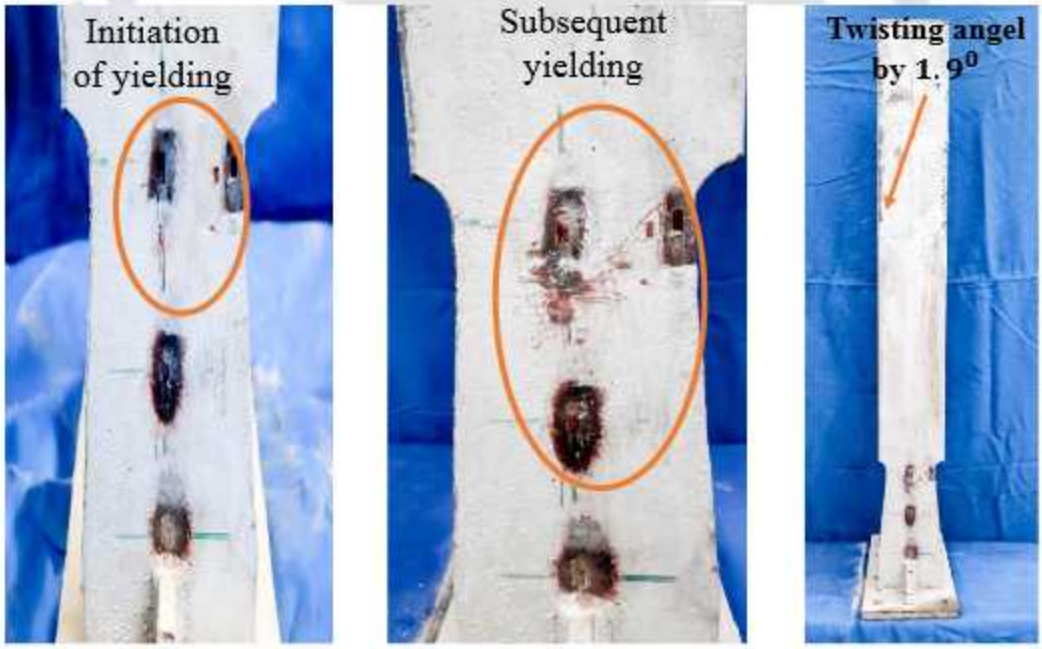

(a) (b) (c)

Fig. 4.5 Visual observation of different damage states for *V*-cut RBS at various rotation:

(a) 0.015 rad (b) 0.02 rad (c) 0.04 rad

yielding to the CFT and bolts during the entire test. Thus, the failure of the *V*-cut RBS and CFT connections is observed only in the reduced beam section. Photograph of the disassembled CFT member, used in all the specimens, after completion of the test program is shown in Fig. 4.8.

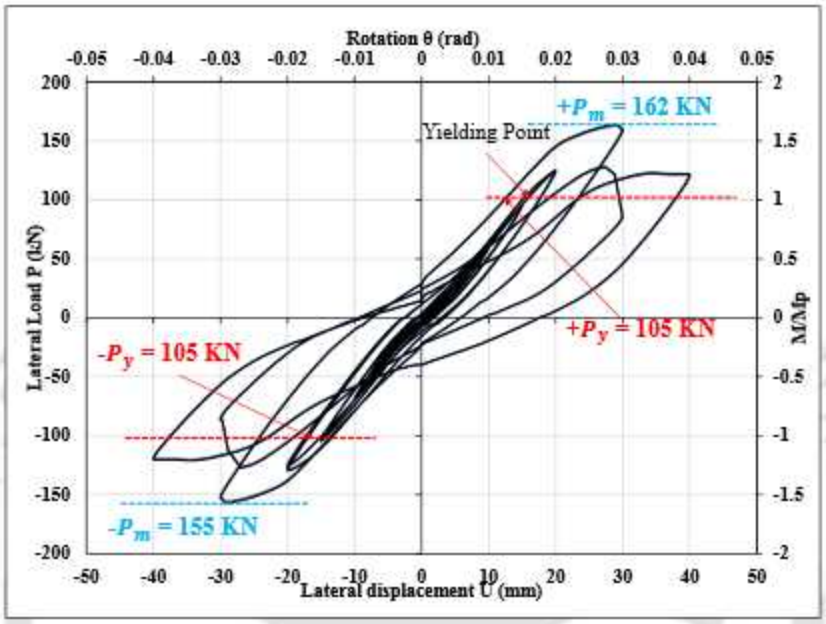

Fig. 4.6 Hysteresis loops of *V*-cut-I RBS-CFT connection

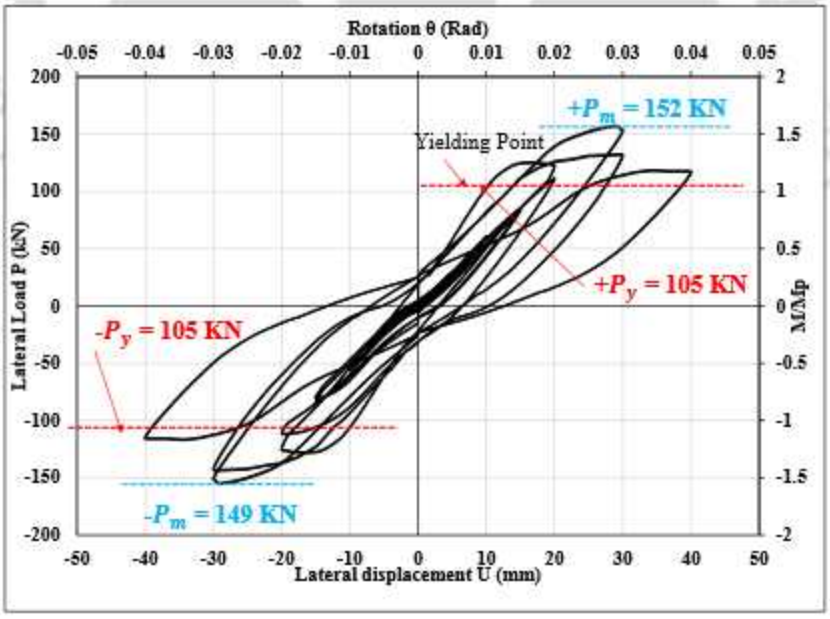

Fig. 4.7 Hysteresis loops of *V*-cut-II RBS-CFT connection

Fig. 4.8 Visual observation on panel zone and CFT column

4.4 Envelope curves

Envelope curve obtained from the load-displacement hysteretic curves are shown in Fig.4.9. In this figure, plastic moment (M_p) capacity is also indicated for both radius cut and V-cut RBSs are also indicated. Plastic moment (M_p) was computed using the material properties obtained from the coupon test. The load displacement curves are linear for both the specimens till 15 mm displacement. V-cut RBS has higher load carrying capacity as compared to that of the radius cut RBS in the displacement range 15 mm to 40 mm.

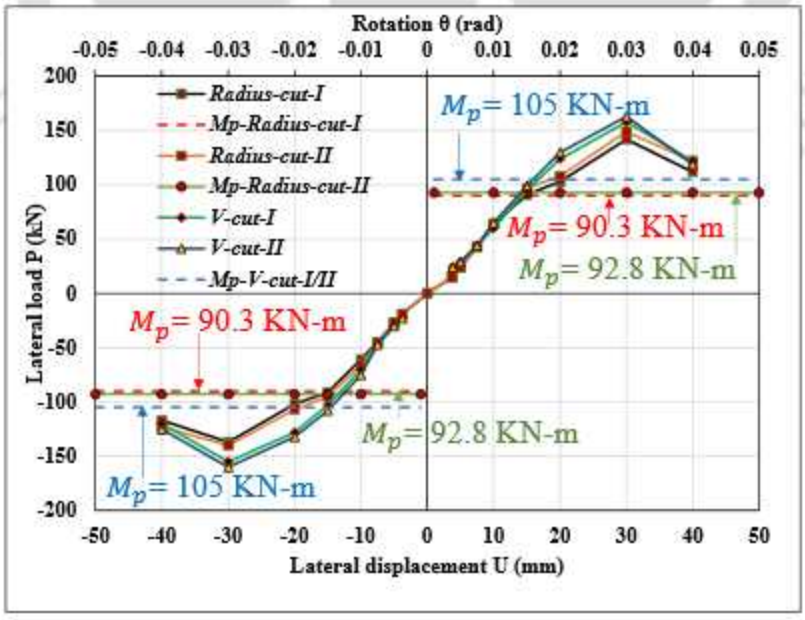

Fig. 4.9 Envelope curves of shaved-cut RBS-CFT connections

The connection can be categorized as full-strength or partial-strength based on the ratio of its maximum bending moment (M_m) to the plastic moment of the beam (M_p).

Radius cut and *V*-cut RBS connections can be considered as full-strength connections since the maximum bending moment (M_m) prior to failure is 50% to 60% greater than of the beam plastic moment (M_p) as indicated in Table 3. This implies exitance of considerable strain hardening in both the specimens. In addition, at 4% story drift the bending moment capacity (M) of radius cut and *V*-cut RBS, are 80% higher than the beam full plastic moment (M_p). Thus, satisfying the specification for special moment frames (SMF) in ANSI/AISC 341.

4.5 Classification of connections

RBS-CFT connection can be classified as fixed, semirigid, or nominally pinned as per Eurocode 3: Part 1-8 1992 [106]. To identify typology of RBS-CFT connection with bidirectional bolts, normalized moment and rotation plots are extracted from experimental data.

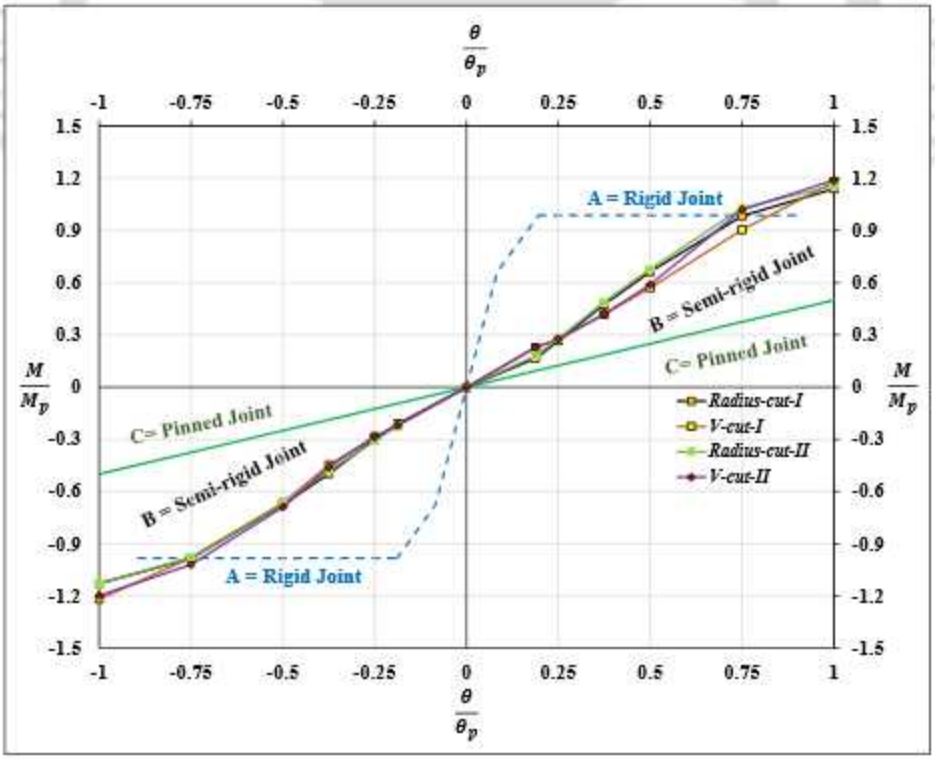

Fig. 4.10 Classification of shaved-cut RBS-CFT connection

The relationship between $\frac{M}{M_p}$ and $\frac{\theta}{\theta_p}$ is used to identify the joint typology [107]. Plastic rotation of the beam θ_p is expressed as:

$$\theta_p = \frac{2LM_p}{EI_n} \tag{4.1}$$

where M_p= plastic moment of beam, θ_p = plastic rotation of beam, L = beam length, E = elastic modulus of steel, and I_n = moment of inertia of beam.

Bending moment (M) is determined multiplying force P by span of beam L; θ is the rotation of the steel beam, which is measured with the inclinometer. The beam-to-column connection is classified as rigid, if the normalized M-θ curve is above the red line and pinned, if the normalized M-θ curve is below the green line as shown in Fig.4.10. Experimentally generated normalized M-θ curves of both the connections lies between the limiting boundary line of fixed joint and pinned joint. Therefore, both these connections are classified as semi-rigid.

4.6 Ductility

The maximum strength P_m of the RBS-CFT connection is defined by the peak load of the envelope curve, and the ultimate strength P_u is defined by 85% of P_m as shown in Fig.4.11. The displacement corresponding to P_u is ultimate displacement U_u.

The displacement ductility coefficient μ_u is defined as the ratio of the ultimate displacement U_u to yield displacement U_y.

$$\mu_u = \frac{U_u}{U_y} \tag{4.2}$$

Table 4.1 presents the displacement ductility coefficients for the tested connections. The displacement ductility of the V-cut RBS is 7% higher as compared that of the radius cut RBS. This indicates that the V-cut RBS marginally better plastic deformation capacity as compared that of the radius cut RBS.

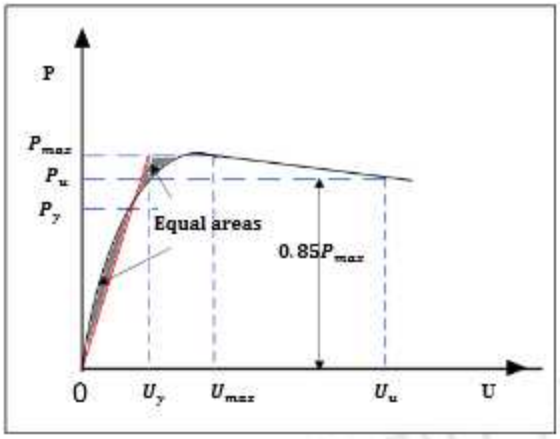

Fig. 4.11 Method of determining U_u

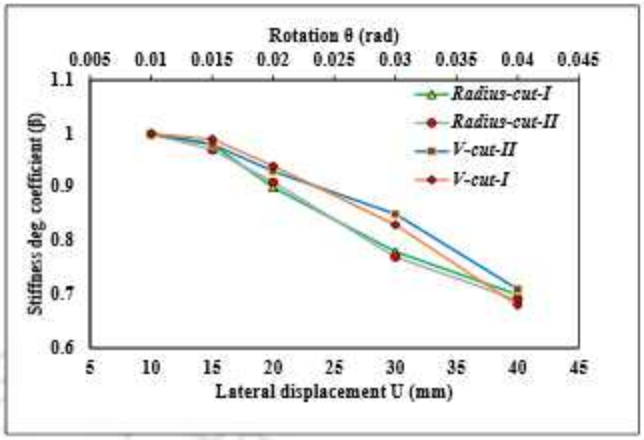

Fig. 4.12 Stiffness degradation ratio of RBS-CFT connection

4.7 Stiffness degradation ratio

The stiffness degradation ratio (β) is defined as ratio of secant stiffness to initial stiffness.

$$\beta = \frac{K_i}{K_o} \tag{4.3}$$

The deterioration of the stiffness of the connections is measured using secant stiffness. Secant stiffness at each displacement amplitude imposed on the specimens corresponding to different displacement cycles is expressed as:

$$K_i = \frac{|+P_i|+|-P_i|}{|+U_i|+|-U_i|} \tag{4.4}$$

where, $+P_i$ and $-P_i$ are the positive and negative peak loads corresponding to the imposed positive and negative displacement amplitudes $+U_i$ and $-U_i$ respectively, K_o= initial stiffness.

The stiffness degradation plots for both specimens are shown in Fig. 4.12. Stiffness coefficients for both specimens remained nearly same as their initial value up to 15 mm displacement. However, this parameter for both the specimens decreased approximately linearly with the increase of the lateral displacement thereafter. Stiffness degradation of *V*-cut RBS is marginally lower as compared to that of the radius cut RBS, which is evident from the Fig. 4.12, in the displacement range 15 mm to 40 mm.

4.8 Strain distribution in RBS and panel zone

The strain distributions for radius-cut RBS and *V*-cut RBS along the length of beam flange are shown from Fig.4.13 to Fig. 4.16 respectively. The yield strain (ε_y) of the beam flange is 1750$\mu\varepsilon$, which was calculated using material properties obtained from the coupon tests. The strain distributions in the positive and negative loading conditions are nearly symmetrical. All the strain gauges in the both types of RBS region reached their yield strain at the rotation of ±0.015 radians. Initially strains increase linearly with rotation up to ±0.015 radians. All strains measured in RBS zone varies the nonlinearly with increase in rotation after attaining yield strain.

Table No.4.1: Summary of the test results for shaved cut RBS-CFT connection

Connection Type		P_y	U_y	P_u	U_u	θ_y	M_s	$\frac{M_m}{M_p}$	θ_u	μ_u	E_t	ξ_{eq}
		kN	mm	kN	mm	rad	kN-mm		rad		KJ	%
Radius-Cut-I	+	92.2	15.04	122	31.88	0.015	112	1.58	0.0318	2.11		
	−	88.4	15.86	118	34.10	0.014	118	1.53	0.0341	2.15	13639	0.16
	Avg.	90.3	15.45	120	32.99	0.0149	115	1.56	0.0330	2.13		
Radius-Cut-II	+	93.6	15.04	123	31.98	0.0151	116	1.32	0.0322	2.13		
	−	92.0	15.96	121	34.15	0.0159	115	1.30	0.0362	2.27	13850	0.16
	Avg.	92.8	15.50	120	33.07	0.0155	115.5	1.31	0.0342	2.20		
V-Cut-I	+	108	15.20	137	34.20	0.015	122	1.54	0.0342	2.25		
	−	102	15.84	132	36.60	0.0154	120	1.47	0.0366	2.31	15378	0.17
	Avg.	105	15.52	135	35.40	0.0152	121	1.50	0.0354	2.28		
V-Cut-II	+	110	15.30	130	34.30	0.0156	115	1.44	0.0343	2.26		
	−	100	15.75	127	36.50	0.0154	111	1.41	0.0365	2.28	15245	0.17
	Avg.	105	15.53	128	35.40	0.0155	113	1.42	0.0354	2.27		

P_y = the yield load; P_u = the ultimate load; u_y = yield displacement; u_u = ultimate displacement; μ_u = ductility; M_m = peak moment; M_p = plastic moment; M_s = Moment at 4% drift; θ_u = ultimate rotation; θ_y = yield rotation; E_t = Total energy dissipation; ξ_{eq} = viscous damping of 29th cycle.

Formation of plastic hinge in RBS zone was observed from the recorded strain values by the gauges *R*1, *R2* and *X1, X*2 for radius cut RBS. Yielding in flanges was observed simultaneously in the strain gauges *X1, X2, Y1, Y2, Z1, Z2* and *V*1, *V2* at rotation ±0.015 radians for *V*-cut RBS. This would ensure increase in plastic hinge length and in turn increase in plastic rotation in *V*-cut RBS in spite lesser depth of cut. It is observed that relatively larger strains were developed in radius cut RBS as compared to that in the *V*-cut RBS. Further, strain distributions in the flanges of radius cut RBS are asymmetric at higher rotations because of higher twisting of beam.

In the panel zone, strains in both the specimens were measured by four reusable strain transducers indicated that the behavior of the panel zone region was well within the elastic range for the both

the specimens. The variation of strains recorded by four strain transducers along two diagonals in the panel zones of the RBS-CFT connection with rotation are shown in Fig.4.17 and Fig.4.18. The yield strains (ε_y) of the steel tube is 1550$\mu\varepsilon$. It is observed that measured strains are substantially lower than the yield strain of the steel tube. Therefore, it can be concluded that the panel zone of both the connection remain elastic. Thus, it may be concluded that the connections with both radius cut and *V*-cut RBS have achieved the design objective of plastic hinge formation only in RBS zone without any damage in the panel zone of the CFT.

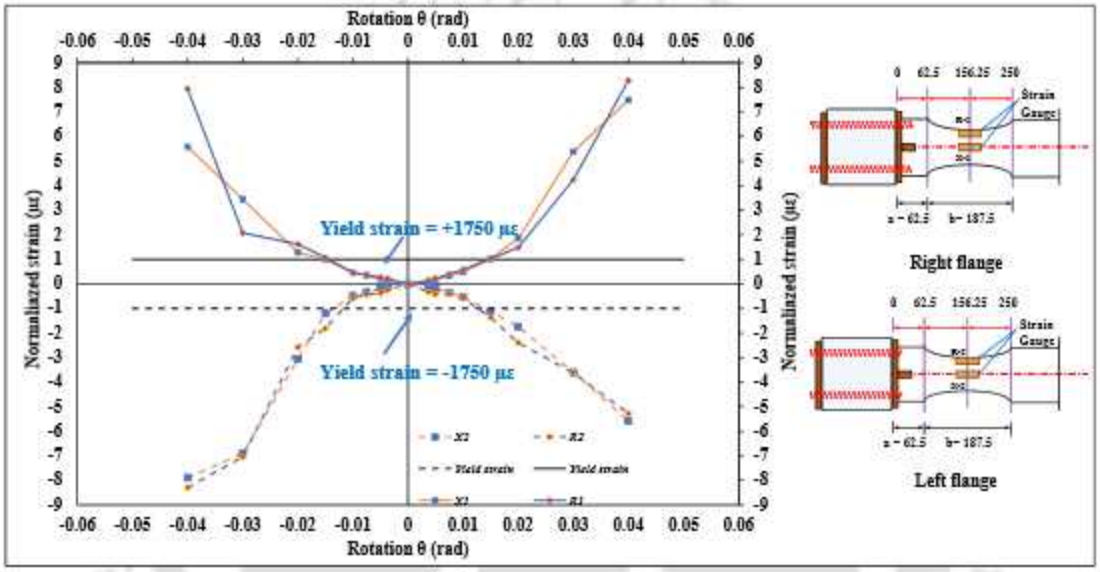

Fig.4.13 Strain vs rotation plot along the length of Radius-cut-I RBS

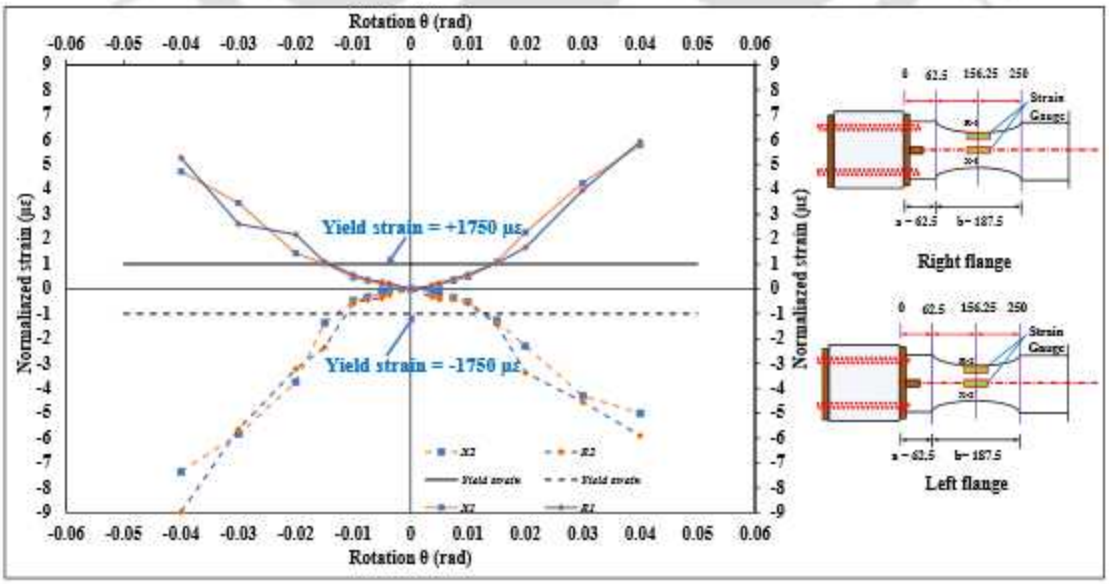

Fig.4.14 Strain vs rotation plot along the length of Radius-cut-II RBS

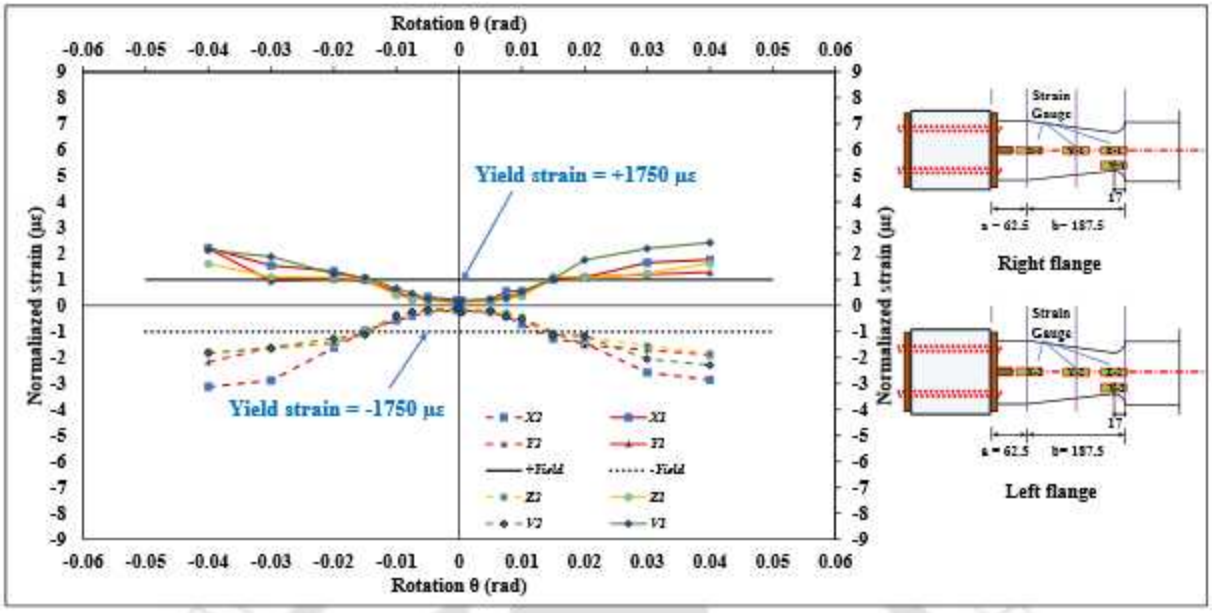

Fig.4.15 Strain vs rotation plot along the length of *V*-cut-I RBS

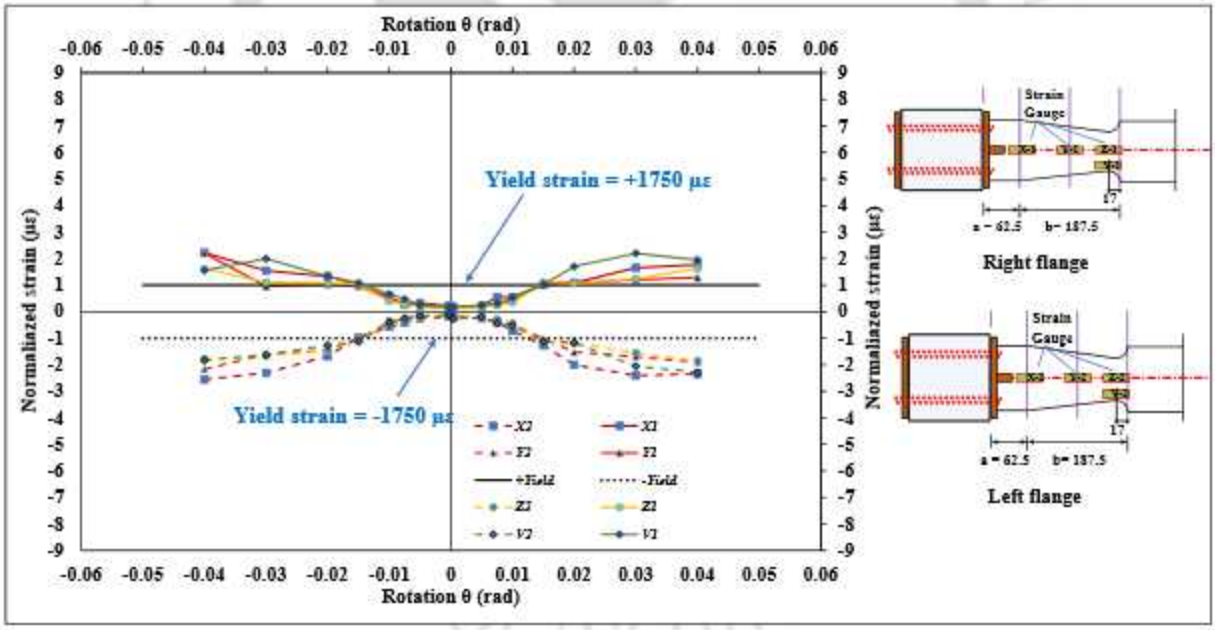

Fig.4.16 Strain vs rotation plot along the length of *V*-cut-II RBS

4.9 Energy dissipation capacity

Energy dissipation capacity of a structure play a crucial role in enhancing its performance during high intensity earthquakes. Area of the force-displacement hysteretic curve was used to calculate the dissipated energy. Fig. 4.19 shows the average energy dissipated in each of the applied displ - acement amplitudes from step-1 to 8.

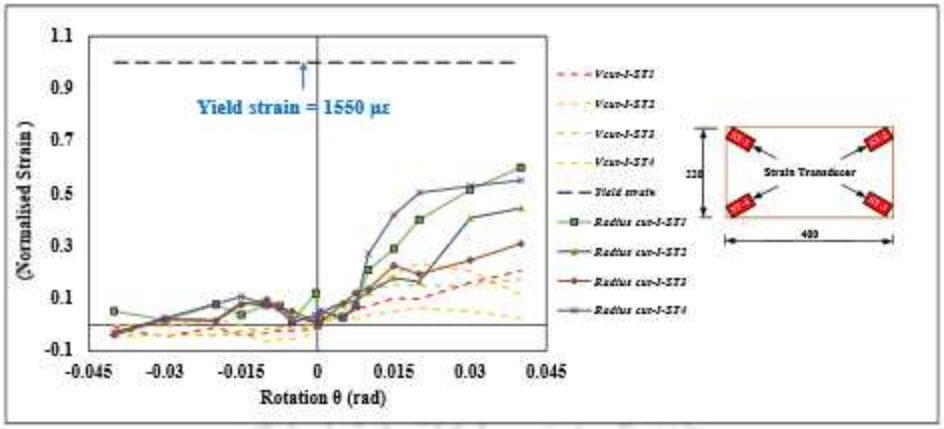

Fig.4.17 Strain vs rotation plot along the diagonals of Panel Zone for Radius cut-I and *V*-cut-I

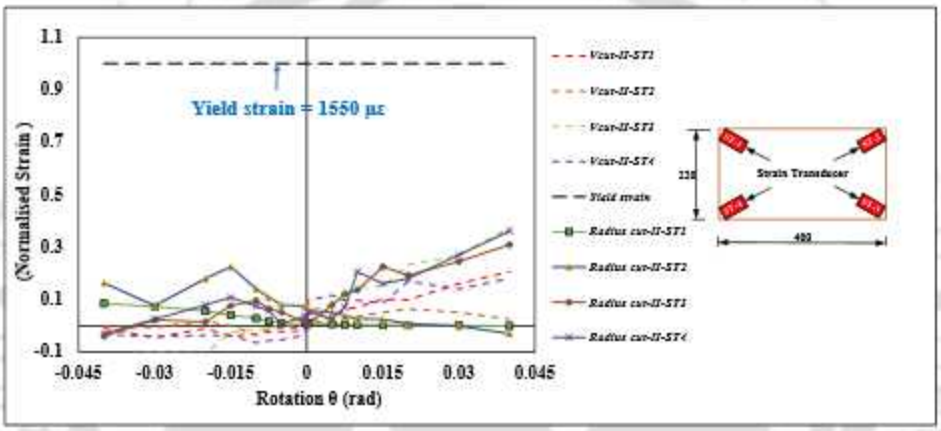

Fig.4.18 Strain vs rotation plot along the diagonals of Panel Zone for radius cut-II and *V*-cut-II

It is observed that energy dissipation is not significant between cycle 1 and 4, which implies that both the RBSs were in an elastic state. However, energy dissipation capacity improved significantly for both the RBSs with the increase in displacement amplitudes after cycle -5 onward. It is observed that the total energy dissipation capacity of *V*-cut RBS is 12-13% higher as compared to that of the radius cut RBS in the displacement cycles 7-8, because of increase in plastic hinge length in the RBS regions. It may also be mentioned that energy dissipation in the RBS-CFT connections is mainly due to the plastic hinge formation in RBS zone.

Equivalent viscous damping coefficient factor (ξ_{eq}) for both the connections is given by [108]

$$\xi_{eq} = \frac{1}{2\pi} \frac{\text{area of the hysteresis loop ABCDA}}{(\text{area of the triangle OBE} + \text{area of the triangle ODF})} \tag{4.5}$$

where, area of the hysteresis loop ABCDA, area of the triangle OBE and the area of the triangle ODF shown in Fig. 4.20.

The equivalent viscous damping factor ξ_{eq} for all displacement amplitudes are shown in Fig.4.21 and Fig. 4.22, and it is increasing with displacement. It is observed that the equivalent damping factor for *V*-cut RBS at highest displacement amplitude is about 17% which is about 1% higher than that of the radius cut RBS. Thus, ξ_{eq} for the *V*-cut RBS is marginally higher as compared to that of the radius cut RBS in spite of experiencing low strain level due to lower depth of cut.

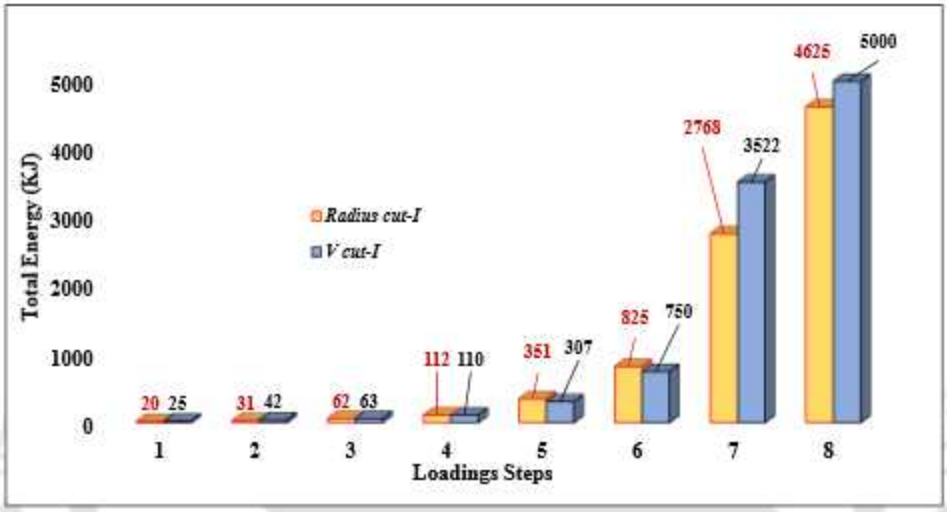

(a)

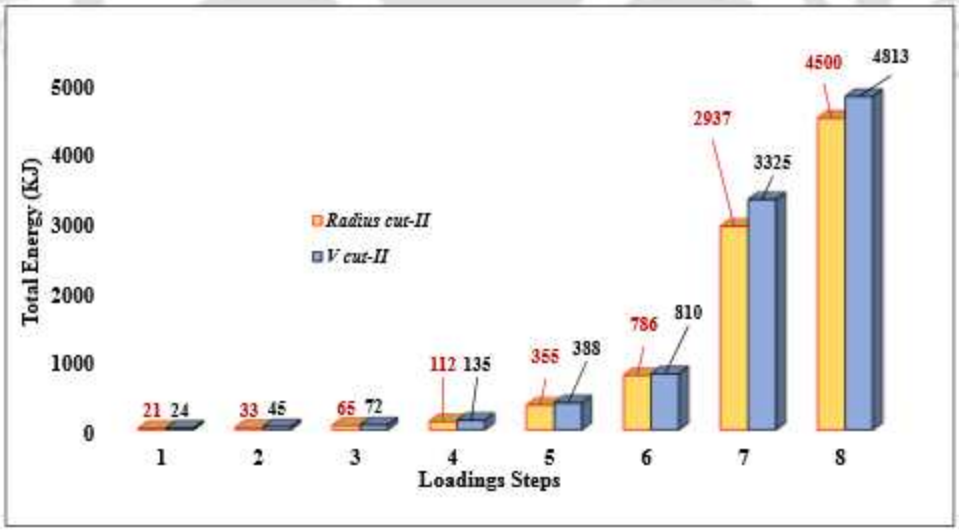

(b)

Fig.4.19 Comparisons of the dissipated energy in RBS-CFT connections: (a) Radius cut-I vs *V*-cut-I (b) Radius cut-II vs *V*-cut-II

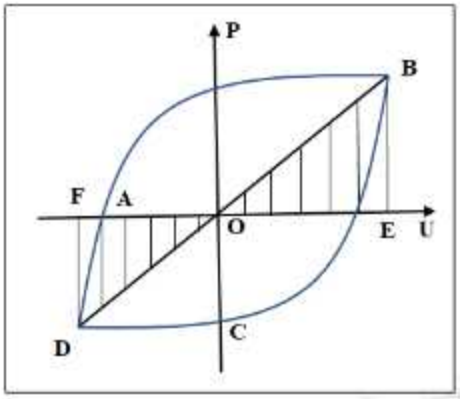

Fig. 4.20 Estimation of equivalent (ξ_{eq})

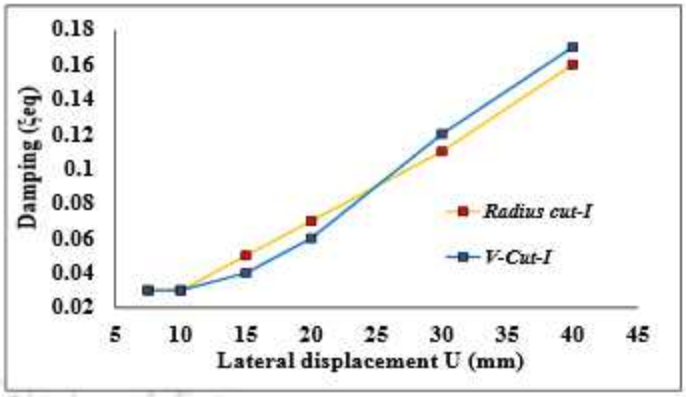

Fig.4.21 Equivalent damping factor (ξ_{eq}) for radius-cut-I and *V*-cut-I RBS

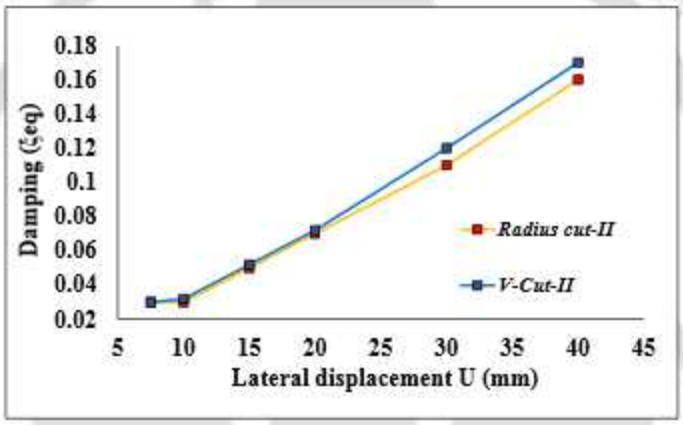

Fig.4.22 Equivalent damping factor (ξ_{eq}) for radius-cut-II and *V*-cut-II RBS

4.10 Concluding remarks

In this chapter, the experimental results of radius cut and *V*-cut RBS-CFT connections with bidirectional bolts were analyzed and various mechanical characteristics are evaluated to understand the behaviour of the connections. Based on analysis of the experimental results reported in this chapter following conclusions are drawn:

1. *V*-cut RBS-CFT connection have higher plastic moment capacity and marginally higher displacement ductility capacity as compared to those parameters of conventional radius cut RBS.
2. In both types of connections, hysteretic energy dissipation was confined in the RBS zone due to plastic hinge formation there. Energy dissipation capacity was 12-13% more in *V*-

cut RBS, due to the increase of plastic moment capacity and plastic rotation capacity, as compared to those of the conventional radius cut RBS.

3. Stiffness degradation ratio was found to be higher in case of *V*-cut RBS due to lesser depth of cut as compared to those of the conventional radius cut RBS for all drift levels.
4. Both types of the RBS-CFT connections were found to be semi-rigid in nature and this would ensure their ductile behavior.
5. Residual torsional deformation is less for *V*-cut RBS due to the less depth of cut as compared to that of the radius cut RBS.

CHAPTER-5

Experimental Study of drilled cut RBS-CFT Connection with bidirectional bolts

CONTENTS

5.1 Introduction

This chapter describes the results of experimental results and discussion on behavior of two types of drilled cut RBS and CFT connections with bidirectional bolts. One specimens of each types of connection were tested under simultaneous action of axial load in CFT and cyclic load at the beam ends. A constant axial load of 10% of gross capacity of the column was applied during the application of cyclic displacements at the time of testing. Force-displacement hysteresis loops of constant drilled cut (*CD*-cut) and varied drilled cut (*VD*-cut) specimens are presented. All the mechanical parameters of both types of RBS-CFT connections are presented. Detailed discussions on experimental behavior of both type of specimens are furnished in the respective sections. Finally, comparisons of test results for constant drilled cut (*CD*-cut), varied drilled cut (*VD*-cut) were made in term of mechanical parameters.

5.2 Cyclic loading protocol

A horizontal loading protocol under displacement control mode, as shown in Fig.5.1, was applied through a 250 kN capacity dynamic servo-hydraulic actuator (make: MTS Inc., USA, Model

244.31) having a stroke length of ± 250 mm. Applied displacement history, as prescribed by AISC, is a sequence of triangular cyclic displacement history with displacement amplitudes of U = ±3.75 mm, U = ±5 mm, U = ±7.5 mm repeated six times; displacement amplitude of U = ±10 mm repeated four times, and displacement amplitudes U = ±15 mm, ±20 mm, ±30 mm and ±40 mm repeated two times. Cyclic test was stopped as soon as the rotational displacement amplitude of the beam reached 0.04 rad or at the failure of specimens. Application of command protocol through the servo-hydraulic actuator and acquisition of feedback signal are carried out using built-in DAQ of the controller (make: MTS Inc., USA, Model: FlexTest-GT).

5.3 General Observation

The experimental results and discussion on behavior of *CD*-cut RBS-CFT and *VD*-cut RBS-CFT connections with bidirectional bolts are reported in this section. Both the test specimens attained maximum rotation of 0.04 rad as per AISC (2010) criteria for composite special moment resisting frames. Force displacement hysteresis behavior of both types of specimens (*CD*-cut, *VD*-cut) exhibited ductile behavior during cyclic test. The plastic hinges are formed in the drilled region of the beam as expected. The column and panel zone area remained elastic at all times. Therefore, same CFT was used in all the test specimens. Detailed discussions on experimental behavior of both type of specimens are furnished in the following sub-sections.

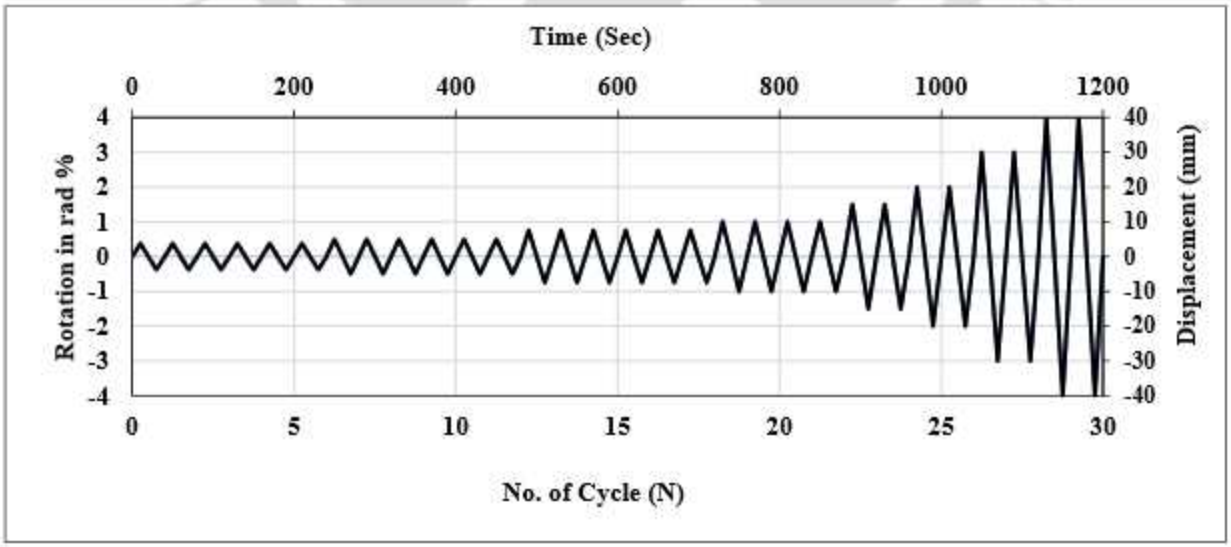

Fig. 5.1 Loading protocol in the experimental program.

5.3.1 Visual Observation of *CD*-cut RBS-CFT connection

The test arrangement of RBS-CFT connection of *CD*-cut and *VD*-cut RBS specimens are shown in chapter 3. A close view of the damaged specimens at end of cyclic test of *CD*-cut RBS are shown in Fig.5.2. The damage states of the *CD*-cut RBS specimens at 0.015 rad, 0.030 rad and 0.04 rad are shown in Fig. 5.2. Load-displacement hysteretic loops of *CD*-cut specimens are shown in Fig.5.3. Silver colour paint flakes got separated from the narrowest part of the flange of this specimen nearly at 0.015 rad rotational angle. This indicates initiation of plastic hinge got started at 1-1 section of the RBS nearly at a rotation of 0.015 rad (corresponds to 23rd and 24th loading cycle). Subsequently, yielding spreaded to the adjoining region of RBS zone (section 2-2 and section 3-3) at higher rotation level in the range of 0.02 rad to 0.03 rad and yielding is confined only in the RBS zone of the beam away from the column and panel zone. The strain gauge data, as indicated in the section 5.8, also confirmed these observations.

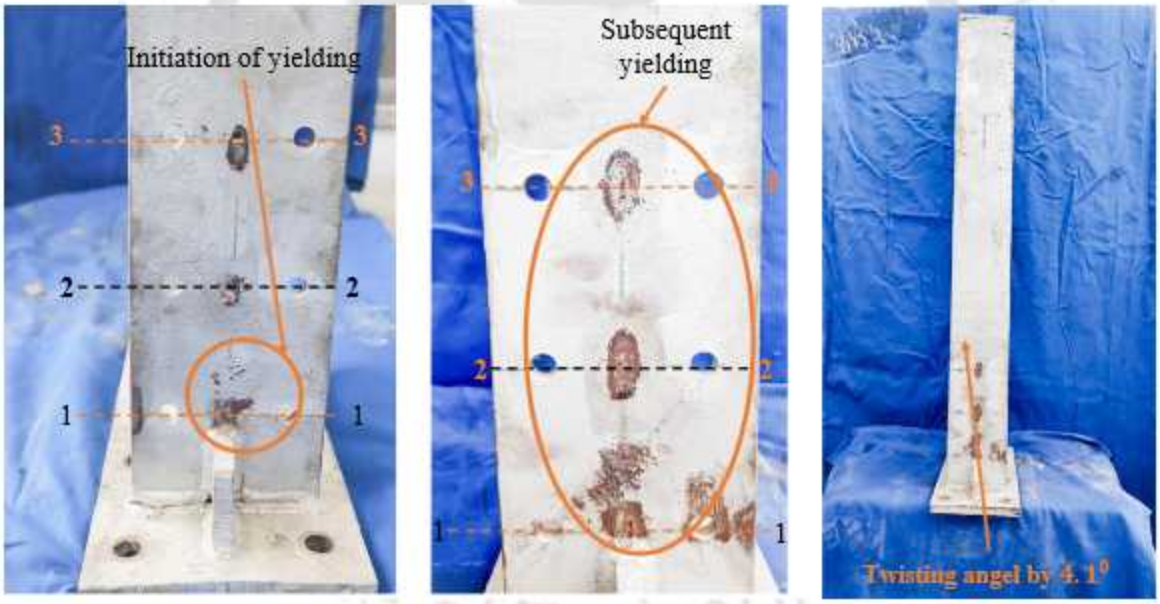

(a) (b) (c)

Fig. 5.2 Visual observation of different damage states for *CD*-cut RBS at various rotation:

(a) 0.015 rad (b) 0.03 rad (c) 0.04 rad

The loading was stopped at 40 mm displacement corresponding to beam rotation of 0.04 rad. It was observed that the *CD*-cut RBS experienced residual twist of 4.1° about longitudinal axis of the beam. Twisting of beam, due to eccentricity between line of action of cyclic load and center

line of the web, could not be restrained by the lateral supports. However, there is no apparent yielding to the CFT and bolts during the entire test. Thus, formation of plastic hinge in the *CD*-cut RBS-CFT connections is observed only in the reduced beam section.

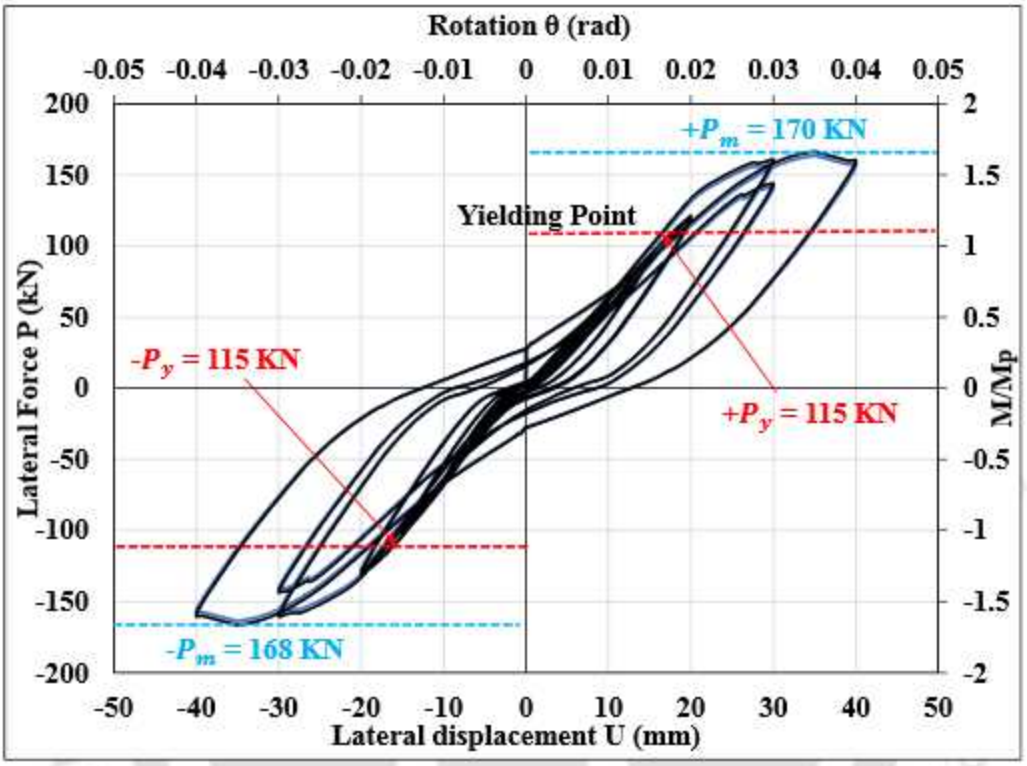

Fig. 5.3 Hysteresis loops of *CD*-cut RBS-CFT connection

5.3.2 Visual Observation of *VD*-cut RBS-CFT Connection

A close view of the damaged specimens at end of cyclic test of *VD*-cut RBS are shown in Fig.5.4. The damage states of the *VD*-cut RBS specimens at 0.015 rad, 0.030 rad and 0.04 rad are shown in Fig. 5.5. Load-displacement hysteretic loops of both the *VD*- cut specimens are shown in Fig.5.5. The plastic hinge formed mainly in the *VD*- cut RBS region away from the column and panel zone. The specimen yielded at a rotational angle of 0.015 rad. Flakes of the silver colour paint separated first around the drilled hole section 1-1 in the flange for this specimen at 0.015 rad rotational angle. Thus, development of plastic hinge got initiated at the drilled hole section 1-1 region for *VD*-cut

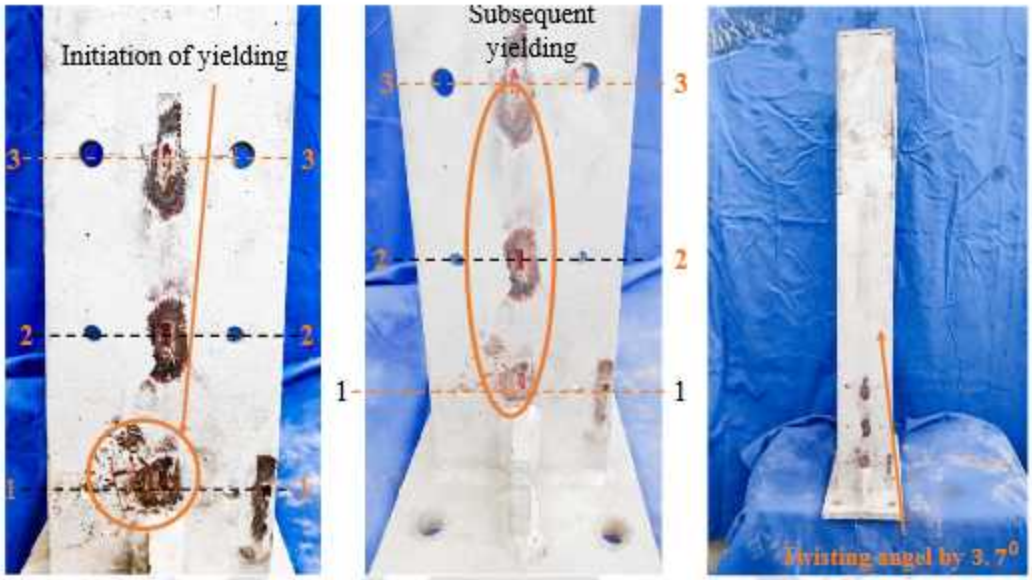

Fig. 5.4 Visual observation of different damage states for *VD*-cut RBS at various rotation

(a) 0.015 rad (b) 0.03 rad (c) 0.04 rad

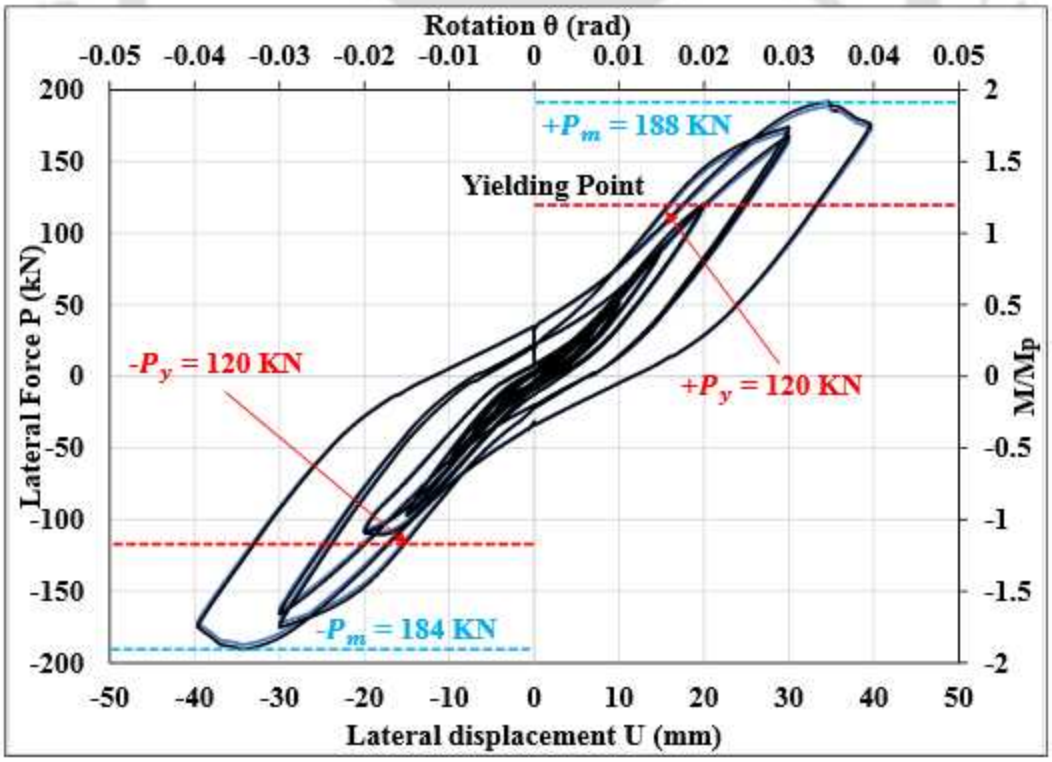

Fig. 5.5 Hysteresis loops of *VD*-cut RBS-CFT connection

Fig. 5.6 Visual observation on panel zone and CFT column

RBS, which is away from the column face and panel zone. Thereafter, yielding spread in the RBS zone between drilled hole section 1-1 and 3-3 at higher rotation in the range of 0.02 rad to 0.03 rad. The strain gauge data, as indicated in the section 5.8, also confirmed these observations. Finally, test was stopped for the specimens after attaining 0.04 rad rotation corresponding to 40 mm displacement. The final angle of twist for *VD*-cut RBS is about 3.7°. Due to the smaller drilling size, the angel of twist of this specimen is observed to be lesser than that in the beam with *CD*-cut RBS. Twisting of beam due to eccentricity between line of action of cyclic load and center line of the web, could not be restrained by the lateral supports. However, there is no apparent yielding to the CFT and bolts during the entire test. Thus, the failure of the *VD*-cut RBS-CFT connections is observed only in the reduced beam section. Photograph of the disassembled CFT member, used in both the specimens, after completion of the test program is shown in Fig. 5.6.

5.4 Envelope curves

Envelope curve obtained from the load-displacement hysteretic curves are shown in Fig.5.7. In this figure, plastic moment (M_p) capacity for both *CD*-cut RBS and *VD*-cut RBS are also indicated. Plastic moment (M_p) was computed using the material properties obtained from the coupon test. The load displacement curves are linear for both the specimens till 15 mm displacement. *VD*-cut RBS has higher load carrying capacity as compared to that of the *CD*-cut RBS in the displacement range 15 mm to 40 mm. The connection can be categorized as full-strength or partial-strength based on the ratio of its maximum bending moment (M_m) to the plastic moment of the beam (M_p).

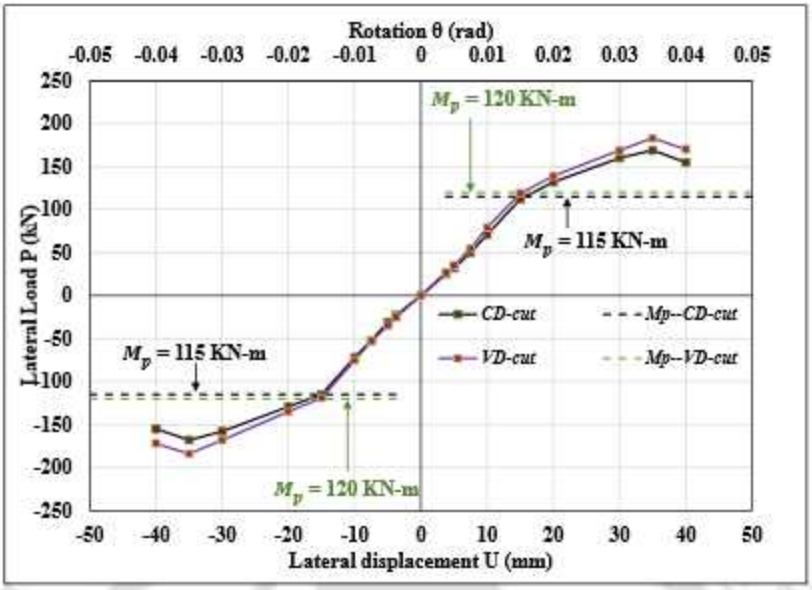

Fig. 5.7 Envelope curves of drilled-cut RBS-CFT connections

CD-cut and *VD*-cut RBS connections can be considered as full-strength connections since the maximum bending moment (M_m) prior to failure is 40% to 50% greater than of the beam plastic moment (M_p) as indicated in Table 5.1. This implies exitance of considerable strain hardening in both specimens. In addition, flexural strength (M_s) of *CD*-cut RBS and *VD*-cut RBS, at 4% story drift are 80% higher than beam full plastic moment (M_p). Thus, satisfying the specification for special moment frames (SMF) in ANSI/AISC 341.

5.5 Classification of connections

In this chapter, classification of RBS-CFT connections was made using non-dimensional $\frac{M}{M_p}$ and $\frac{\theta}{\theta_p}$ relationship. Eq.4.1 defining relationship between plastic moment (M_p) and plastic rotation (θ_p) used to calculate the plastic rotation.

Bending moment (M) is determined multiplying force P by span of beam L; θ is the rotation of the steel beam, which is measured with the inclinometer. The beam-to-column connection is classified as rigid if the normalized M-θ curve is above the blue line and pinned, if the normalized M-θ curve is below the green line as shown in Fig.5.8. Experimentally generated normalized M-θ curves of

both the connections lies between the limiting boundary line of rigid joint and pinned joint. Therefore, both these connections are classified as semi-rigid.

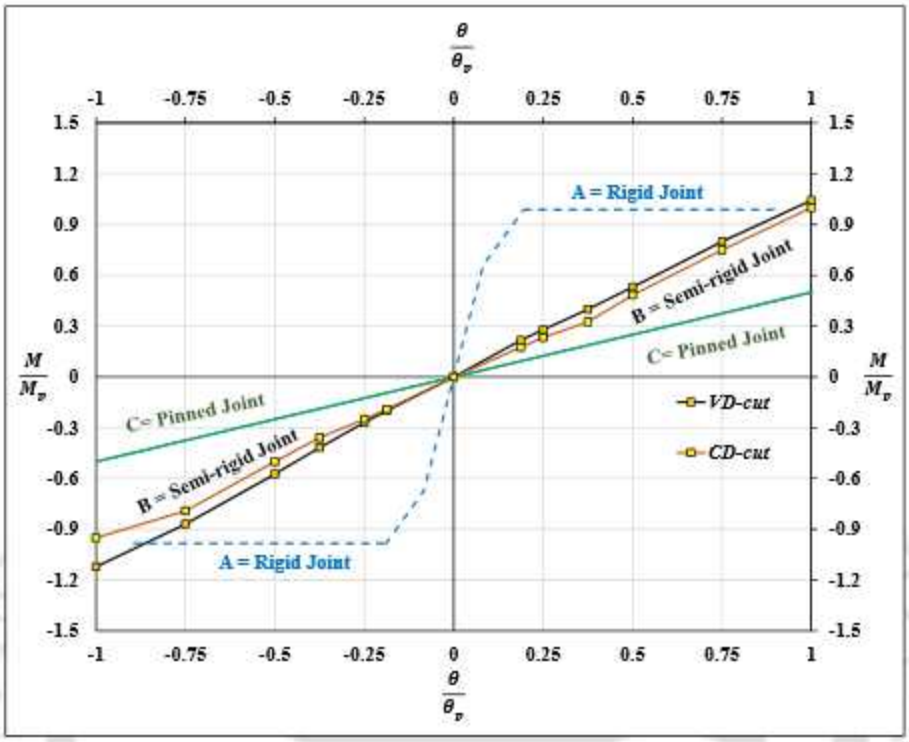

Fig. 5.8 Classification of drilled-cut RBS-CFT connection

5.6 Ductility

Generally, the ultimate strength (P_u) of the connection is defined from the envelope curve, and it is considered as 85% of maximum strength (P_m) as shown in Fig. 4.11 in chapter 4. Here sufficient degradation of strength was not observed from the envelope curve shown as in Fig. 5.8 after achieving the maximum strength corresponding to the displacement of 35 mm (0.035 rad). Thus, ultimate displacement (U_u) is not obtained from the envelope curve. Due to these reason 40 mm displacement is considered here as ultimate displacement (U_u). Table 5.1 presents the displacement ductility co-efficient for the tested specimens.

5.7 Stiffness degradation ratio

The stiffness degradation of RBS-CFT connections was defined using by non-dimensional stiffness ratio β. The Eq. 4.2 and Eq. 4.3 were used for calculation of β.

The stiffness degradation plots for both specimens are shown in Fig. 5.9. Stiffness coefficients for both specimens remained nearly same as their initial value up to 15 mm displacement. However, this parameter for both the specimens decreased approximately linearly with the increase of the lateral displacement thereafter. Stiffness degradation of *VD*-cut RBS is marginally higher as compared to that of the *CD*-cut RBS, which is evident from the Fig. 5.9, in the displacement range 15 mm to 40 mm.

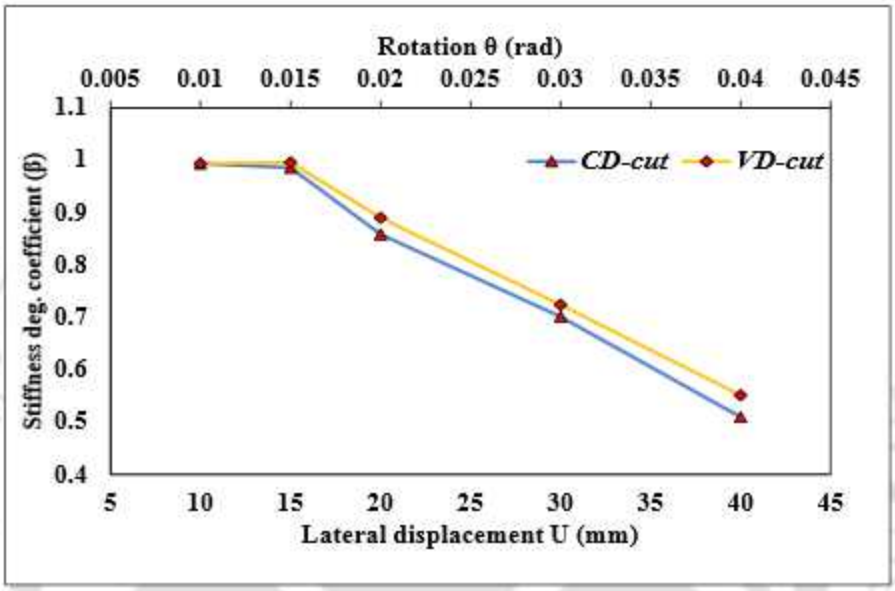

Fig. 5.9 Stiffness degradation ratio of RBS-CFT connection

5.8 Strain distribution in RBS and panel zone

The strain distributions for *CD*-cut RBS and *VD*-cut RBS along the longitudinal direction of beam flange are shown in Fig.5.10 and Fig. 5.11 respectively. The yield strain (ε_y) of the beam flange is 1750$\mu\varepsilon$, which was calculated using material properties obtained from the coupon tests. The strain distributions in the positive and negative loading conditions are nearly symmetrical. During visual inspections, it was also observed that flakes of silver colour paint come out of the surface of the steel flanges of RBS zones at a rotation of 0.015 radians, indicating onset of yielding. All the strain gauges in the both types of RBS region reached their yield strain at the rotation of ±0.015 radians. Initially strains increase linearly with rotation till its value is ±0.015 radians. All strains measured in RBS zone varies the nonlinearly with increase in rotation after attaining yield strain. Formation of plastic hinge in RBS zone was observed from the recorded strain values by the gauges

D1, *D2* and *X1*, *X2*, *Y1*, *Y2*, *Z1*, *Z2* for *CD*-cut RBS. Yielding in flanges was observed simultaneously in the strain gauges *X1*, *X2*, *Y1*, *Y2*, *Z1*, *Z2* and *H1*, *H2* at rotation ±0.015 radians for *VD*-cut RBS. This would ensure increase in plastic hinge length and in turn increase in plastic rotation in *VD*-cut RBS in spite less drill in size. It is observed that relatively larger strains were developed in *CD*-cut RBS as compared to that in the *VD*-cut RBS. Further, strain distributions in the flanges of *CD*-cut RBS are asymmetric at higher rotations because of higher twisting of beam.

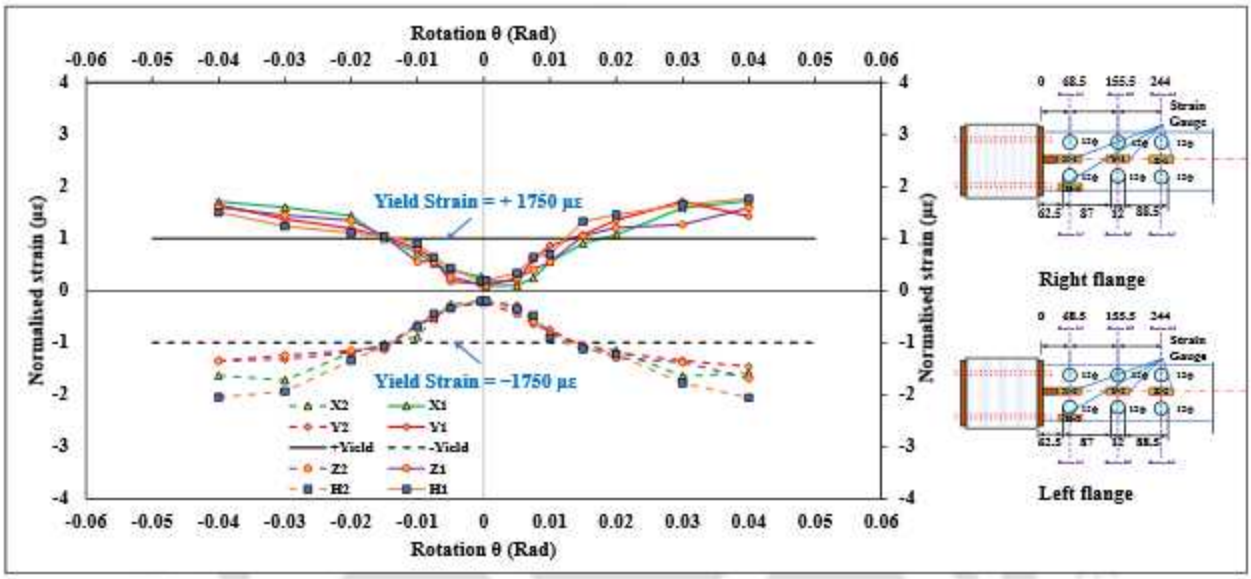

Fig.5.10 Strain vs rotation plot along the length of *CD*-cut RBS

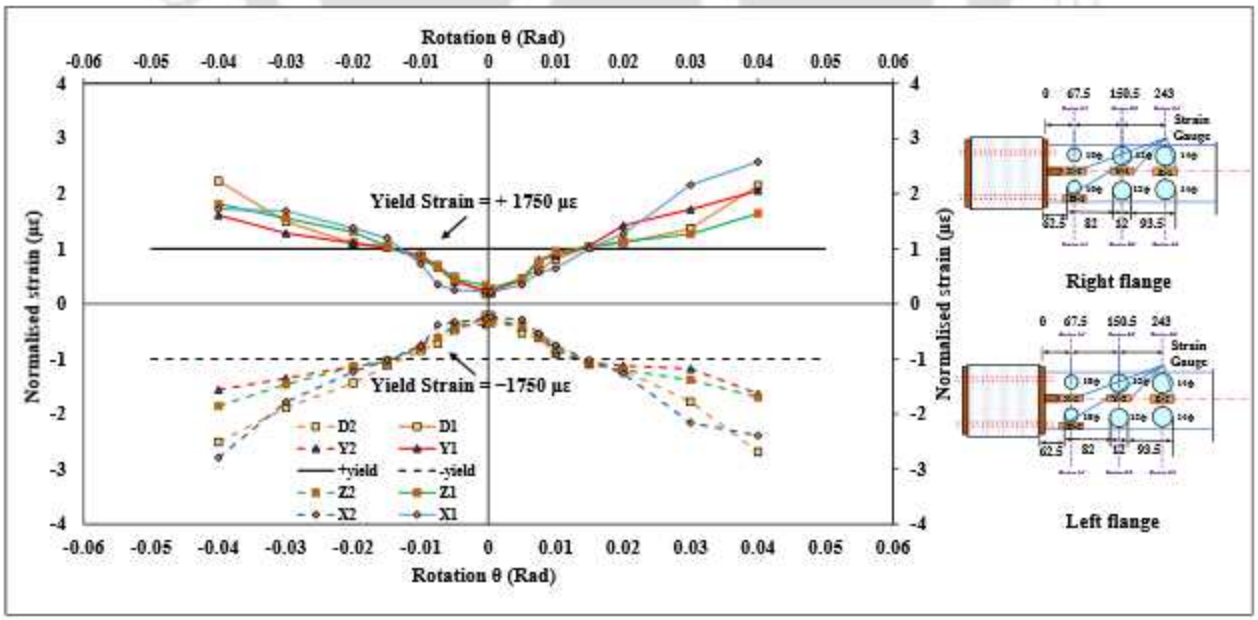

Fig.5.11 Strain vs rotation plot along the length of *VD*-cut RBS

In the panel zone, strains were measured by four reusable strain transducers for both the specimen. It was observed that the behavior of the panel zone region was well within the elastic range for the both the specimens. The variation of strains recorded by four strain transducers along two diagonals in the panel zones of the RBS-CFT connection with rotation are shown in Fig.5.12. The yield strains (ε_y) of the steel tube is 1550$\mu\varepsilon$. It is observed that measured strains are substantially lower than the yield strain of the steel tube. Therefore, it can be concluded that the panel zone of both the connection remain elastic.

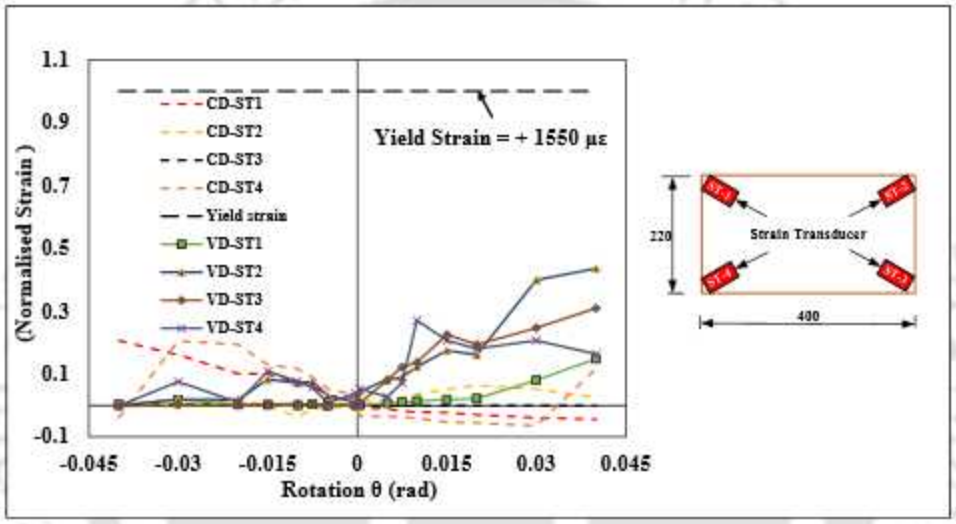

Fig.5.12 Strain vs rotation plot along the diagonals of panel zone

Thus, it may be concluded that the connections with both *CD*-cut and *VD*-cut RBS have achieved the design objective of plastic hinge formation only in RBS zone without any damage in the panel zone of the CFT.

5.9 Energy dissipation capacity

Energy dissipation capacity of a structure play a crucial role in enhancing its performance during high intensity earthquakes. Area of the force-displacement hysteretic curve was used to calculate the dissipated energy. Fig. 5.13 shows the average energy dissipated in each cycle with any applied displacement amplitudes from step-1 to 8. It is observed that energy dissipation is not significant

between cycle 1 and 4, which implies that both the RBSs were in an elastic state. However, energy dissipation capacity increased significantly for both the RBSs with the increase in displacement amplitudes after cycle -5 onward. It is observed that the total energy dissipation capacity of *VD*-cut RBS is 1-2% higher as compared to that of the *CD*-cut RBS in the displacement cycles 7-8, because of increase in plastic hinge length in the RBS regions. It may also be mentioned that energy dissipation in the RBS-CFT connections is mainly due to the plastic hinge formation in RBS zone. Equivalent viscous damping coefficient factor (ξ_{eq}) for both the connections is calculated using Eq.4.4 [108].

Cumulative energy dissipation at any particular displacement amplitude can be calculated by summing the areas corresponding to the preceding displacement amplitudes with energy dissipation of that displacement amplitude. Fig.5.13 shows that the cumulative energy dissipation, are nearly same for both the RBS-CFT connections.

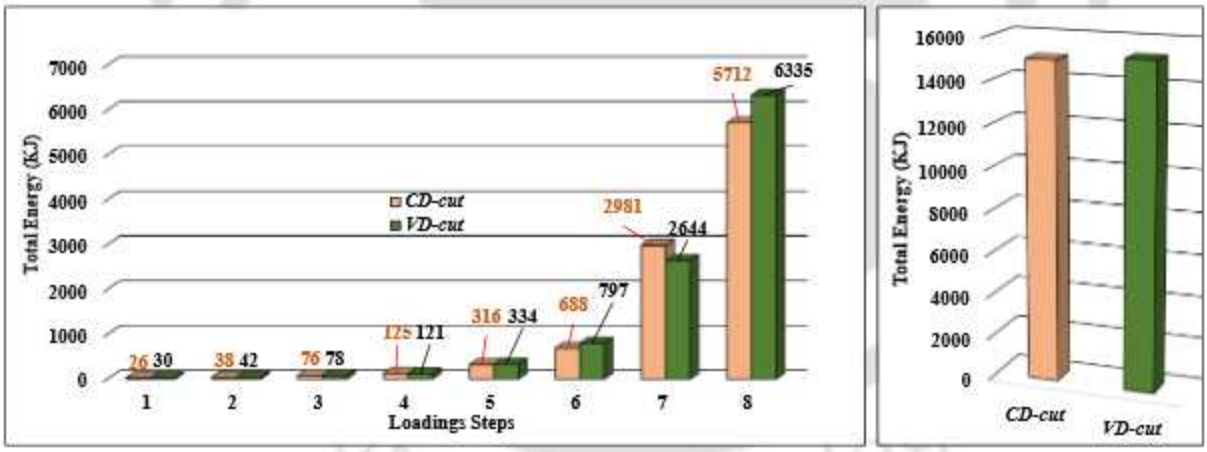

(a) (b)

Fig.5.13 Comparisons of the dissipated energy in RBS-CFT connections: (a) average (b) cumulative

The equivalent viscous damping factor ξ_{eq} for all displacement amplitudes are shown in Fig.5.14. It is observed that ξ_{eq} is increasing with increase in displacement. Equivalent damping factor for *VD*-cut RBS at highest displacement amplitude is about 15% which is same as of the *CD*-cut RBS. Thus, ξ_{eq} for the *VD*-cut RBS is same as compared to that of *CD*-cut RBS in spite of experiencing low strain level due to lesser drilling size.

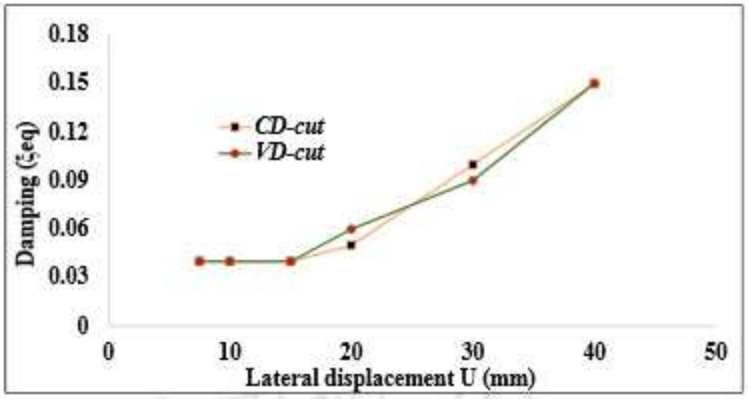

Fig.5.14 Equivalent damping factor (ξ_{eq}) for *CD*-cut and *VD*-cut RBS

5.10 Concluding remarks

In this chapter, the experimental results of *CD*-cut and *VD*-cut RBS-CFT connection with bidirectional bolts specimens were analyzed and various parameters are calculated to understand the behaviour of the joints. The failure modes, hysteresis curve, envelope curve, typology of the connection, the stiffness, energy dissipation, damping and strain distribution of the specimens were analyzed. Based on experimental study reported in this chapter following conclusion are drawn:

Table No.5.1: Summary of the test results for drilled cut RBS-CFT connection

Connection Type		P_y	U_y	M_m	U_u	θ_p	M_s	μ_u	$\frac{M_m}{M_p}$	E_t	ξ_{eq}
		kN	mm	kN-m	mm	rad	kN-m			KJ	%
CD-Cut	+	118	15.62	169	40	0.0156	155	2.56	1.46	15022	0.15
	−	112	15.08	167	40	0.0150	155	2.65	1.45		
	Avg.	115	15.35	168	40	0.0153	155	2.60	1.455		
VD-Cut	+	122	15.82	183	40	0.0158	170	2.52	1.52	15269	0.15
	−	118	15.18	181	40	0.0156	172	2.63	1.50		
	Avg.	120	15.50	182	40	0.0157	171	2.58	1.51		

P_y= the yield load; u_y= yield displacement; M_m= peak moment; M_p= plastic moment; M_s= flexural strength at 4% drift; θ_p= yield rotation; E_t = Total energy dissipation; ξ_{eq}= viscous damping of 29th cycle; u_u= Ultimate displacement; μ_u = ductility

1. *VD*-cut RBS connection has higher plastic moment capacity than *CD*-cut RBS connection.
2. Cumulative energy dissipation capacity of *VD*-cut RBS is marginally higher as compared to the *CD*-cut RBS. However, equivalent damping factor for *VD*-cut RBS is almost of the same order as that of the *CD*-cut RBS.
3. Stiffness degradation ratio for all drift levels was found to be higher in case of connection with *VD*-cut RBS as compared to with the *CD*-cut RBS due to smaller drilling size of the beam flange.
4. Residual lateral torsional deformation is lower for *VD*-cut RBS due to less drilling size at section 1-1 as compared to that of the *CD*-cut RBS.
5. Both the connections ensure ductile behavior because of their semi-rigid nature of the RBS-CFT connections.

CHAPTER-6

Numerical study of RBS-CFT Connection with bidirectional bolts

CONTENTS

6.1 Introduction

In this chapter, FE based numerical simulation of force-displacement characteristics of RBS-CFT connection using ABAQUS (v 6.6-1, 2006) [109] is presented first. Force displacement back-bone curves for the model RBS-CFT connections are simulated and the same are compared with the experimental force-displacement back-bone curves. Numerical modelling of RBS-CFT connections with bidirectional bolts, are very challenging task, in view of multiple interactions amongst various load effects. Therefore, a simplified numerical modelling of RBS-CFT connections is also proposed in OpenSees (v.17.7.3, 2006) [110] platform for simulation of their force-displacement hysteretic behaviour. Simulated force-displacement behaviour of the RBS-CFT connections are compared with the experimental force-displacement relationship for validation of the numerical models.

6.2 Detailed numerical modelling

Three-dimensional finite element models of the RBS-CFT connections with bidirectional bolts were developed using the general-purpose FE software ABAQUS and details of the modelling procedure are reported in this section. These numerical models consist of a combination of various types of element. The models consider material nonlinearity, contact issues, surface interactions

along with constraint conditions. This advanced modelling approach are intended for realistic understanding of the overall behaviour of the connections, including the location of the damage and load displacement characteristics.

6.2.1 Simulation for validation of the modelling approach

A specimen, designated as EEP, of steel beam-column connection studied by Elflah et al. [111] is modelled using ABAQUS finite element software as shown in Fig.6.1. The specimens are analyzed under the increasing monotonic load and the numerical results are compared with experimental ones. All components of the specimen are modelled by using the continuum three-dimensional eight noded solid element with reduced integration technique (C3D8R). Table 6.1 shows the materials properties used in the analysis. Several mesh densities were considered for the sensitivity analysis. The contact between the various non-welded components of the joint was modelled by using the *surface to surface* contact definitions available in ABAQUS. Surfaces discretized with course meshes were selected as master surfaces, while the more finely discretized surfaces were selected for salve surfaces.

The contact pressure-clearance relationship was defined as *hard contact* for the all cases to allow full transfer of the compression loads and separation after contact. The penalty method with a friction coefficient of 0.3 was defined for the tangential response of all contact surfaces. Finite sliding contact formulation was employed for all other contact pairs.

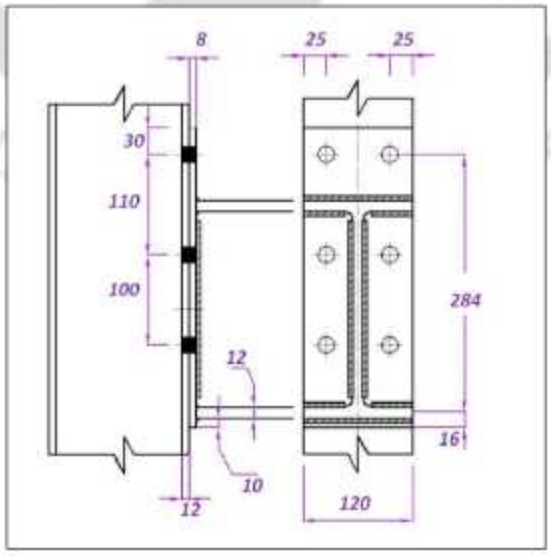

Fig. 6.1 Connection details [111]

Table No. 6.1 Material properties of beam-column connection [111].

Specimen	E MPa	$\sigma_{0.2}$ MPa	$\sigma_{0.1}$ MPa	σ_u MPa	ε_f (%)
***I*-240x120x12x10-flange**	196500	248	306	630	66
***I*-240x120x12x10-web**	205700	263	320	651	65
End plate	198000	282	343	655	54
***M 16* bolt (A4-80)**	191500	617	703	805	12

A monotonically increasing displacement upto 40 mm was applied to the end of the beam. The moment-rotation response obtained from both numerical and experimental studies were plotted. Numerically simulated and experimental moment-rotation curves for the connection were found to be in good agreement as shown in Fig. 6.2. It may be observed that both simulated and experimental failure modes of the connections were found to be in reasonably good agreement. Simulated failure modes and experimental failure modes are shown in the Fig. 6.3. Validation of this numerical model established that interaction properties, mesh size, mesh types, and boundary conditions of the simulated specimen are good enough to replicate the results obtained by experimental work. Hence, a similar modelling method can be adapted for computation of response of the sample model RBS-CFT connections with bidirectional bolts using ABAQUS finite element programme.

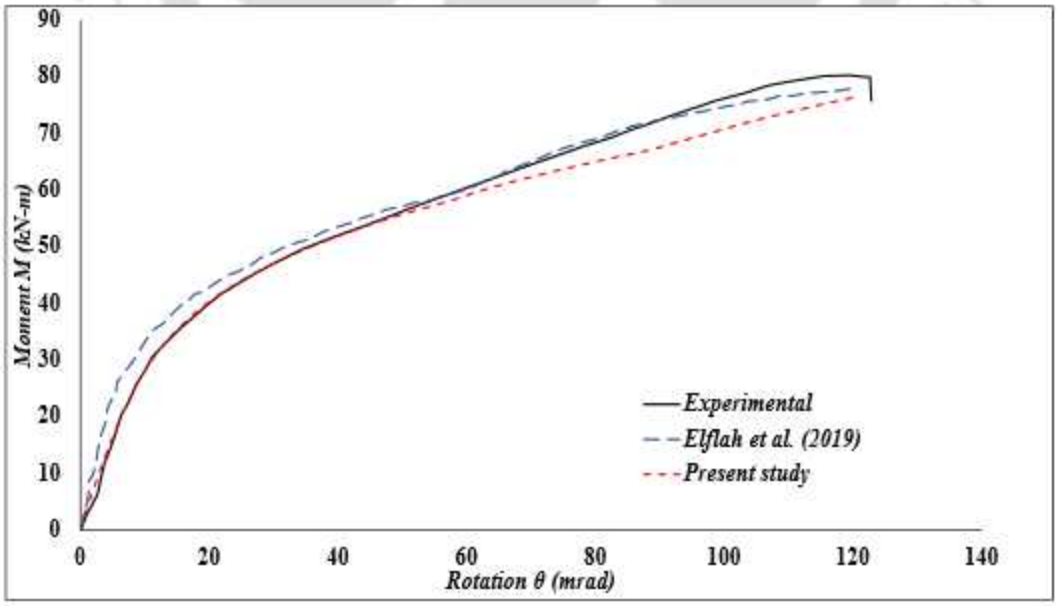

Fig. 6.2 Validation of numerically simulated *M-θ* curve

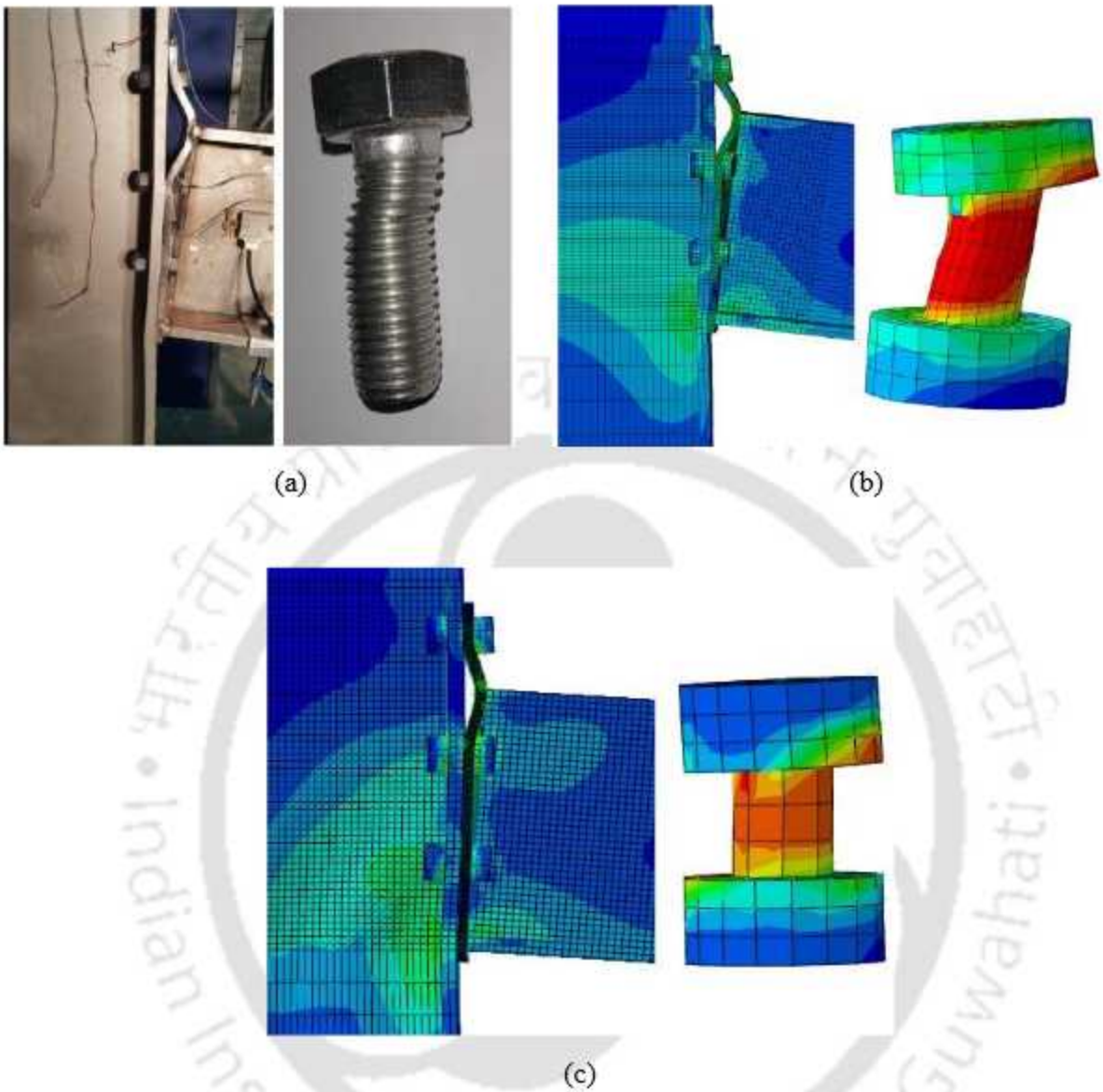

Fig. 6.3 Failure modes between tests and FE simulation adopted for present study (a) Experimental failure modes [111] (b) Numerical failure modes [111] (c) Numerical failure modes (present study)

6.2.2 Modelling of RBS-CFT connection

The numerical models of RBS-CFT connections with bidirectional bolts consisted of a combination of solid elements and constraints conditions. These were refined 3D solid elements incorporating the nonlinear material properties, contact elements, surface interaction with friction. These advanced modeling methods were intended to provide a detailed and accurate understanding of the overall behavior of the connections, including the stress distributions in the RBS zone and identification of damage location of the connection.

Finite Element Modelling: Three dimensional (3D) deformable solid types of elements were chosen for the modelling of different components. The six basic components (concrete core, steel tube, bolts, endplate, stiffener, beam) are shown as assemblies of 3D solid elements in Fig.6.4. Cross-section of each section was first created and then extruded to provide the desired length. For generating bolt parts, the *revolution* technique was used, in which a section of the bolt was created first and then rotated by 360°. Close-up view of the corresponding RBS connection areas is also shown in Fig. 6.4.

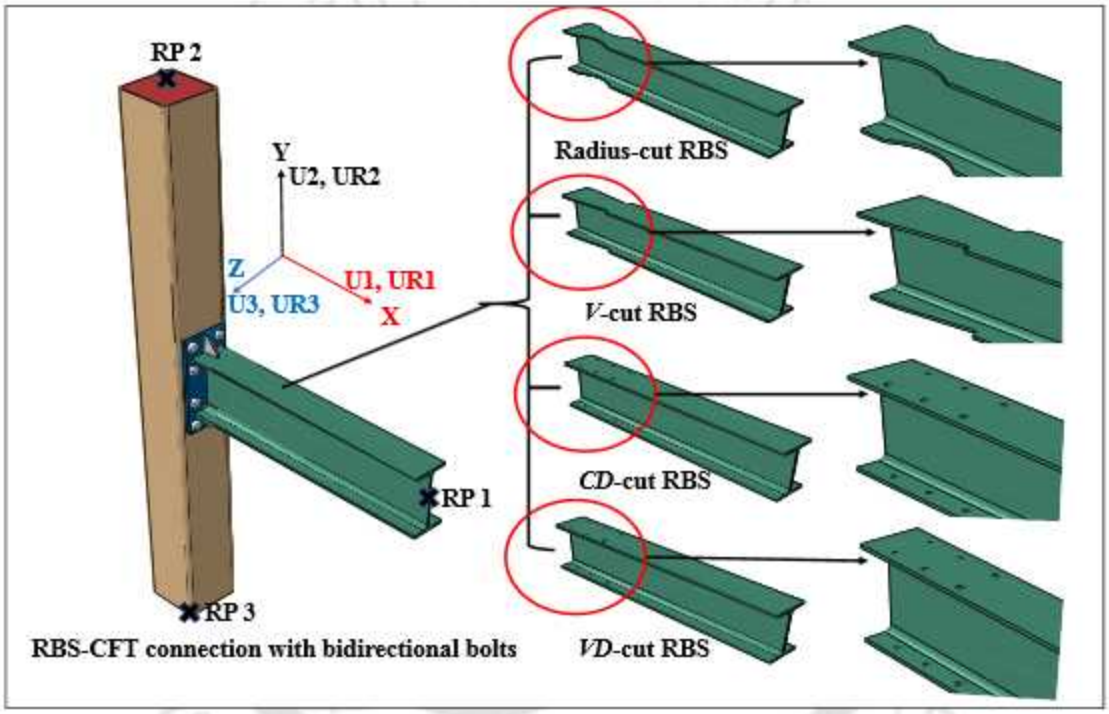

Fig. 6.4 3D models for all RBS-CFT connection

In these figures, C3D8R (Continuum three dimensional eight noded brick element with reduced integration) elements are adopted for the end-plate, stiffeners and beam. C3D6 (Continuum three dimensional six noded linear prism) element were used for the bolt specimen also shown in Fig.6.4 on the top-right. These elements provide reduction in the number of elements and enhanced associated computational efficiencies. C3D8R elements are adopted for concrete core and steel tube. Several mesh densities were considered for the sensitivity analysis. Sensitivity analysis was carried out to choose optimum size of elements. It was observed that at least two elements needed along the thickness of thin-walled components such as end plates, flanges and webs of the beam

to accurately capture their flexure behavior and avoid shear locking. A sufficiently good member of elements is considered to simulate the realistic failure of the connection. Detailed meshing of different RBS-CFT connection are shown in Fig. 6.5 to Fig. 6.8.

Material Properties: Material properties for each component were kept similar. The steel material properties for each component members were modeled with fully nonlinear isotropic characteristics coupled with von-Mises yield criterion. The Young's modulus values characterizing the elastic material response and the stress-strain values used to define the plasticity model were derived from the tensile coupon tests reported in chapter 3. For the material property of these components, different grade of steel was chosen with the modulus of elasticity and Poisson's ratio as 210000 N/mm^2 and 0.3 respectively. The density value was kept as 7.85e^{-9} ton/mm^3. Stress-strain curve for different grade of steel components were used in the study with calibrations. The material stress-strain data was then converted to true stress and plastic strain. The concrete was modelled as an elastic material because of no damage in the panel zone was observed during the experimental study.

***Constraint and Interaction properties*:** The welds between the beams and endplates were not explicitly modelled, since their response are rigid and no weld failure occurred during testing. The *Tie* constraint was used to connect the beam and endplate for the simulation. Here *Tie* constraint ties two separate surfaces i.e. endplate and beam together so that there is no relative motion between them. Different types of interaction are considered for defining the interactions between various components like concrete-tube, endplate-tube, bolt head-end plate, and bolt shank-bolt hole. Interactions provided between different contact surfaces are: *i*) surface 1: outer surface of filled core concrete and the inner surface of steel tube, *ii*) surface 2: Outer surface of steel tube and the inner surface of endplates, *iii*) surface 3: Outer surface of endplates and the surface of bolt heads, *iv*) Surface 4: Surface of bolt shank and the surface of bolt holes. The interface interaction between different components of the model were defined by the *surface to surface* algorithm available in ABAQUS. The surfaces discretized with finer meshing were selected as the *Slave* surface and the surfaces discretized with coarse meshing were selected for the *Master* surface. *Hard* contact pressure-overclosure with allowed separation after contact relationship was defined as normal behavior. Here this option would allow surfaces to transfer full bearing pressure and separation

after contact. For behavior in the tangential direction, *Penalty* friction formulation was used with the value of the coefficient of friction as 0.3. For interaction between filled core concrete and steel tube, the value of the coefficient of friction was taken as 0.6.

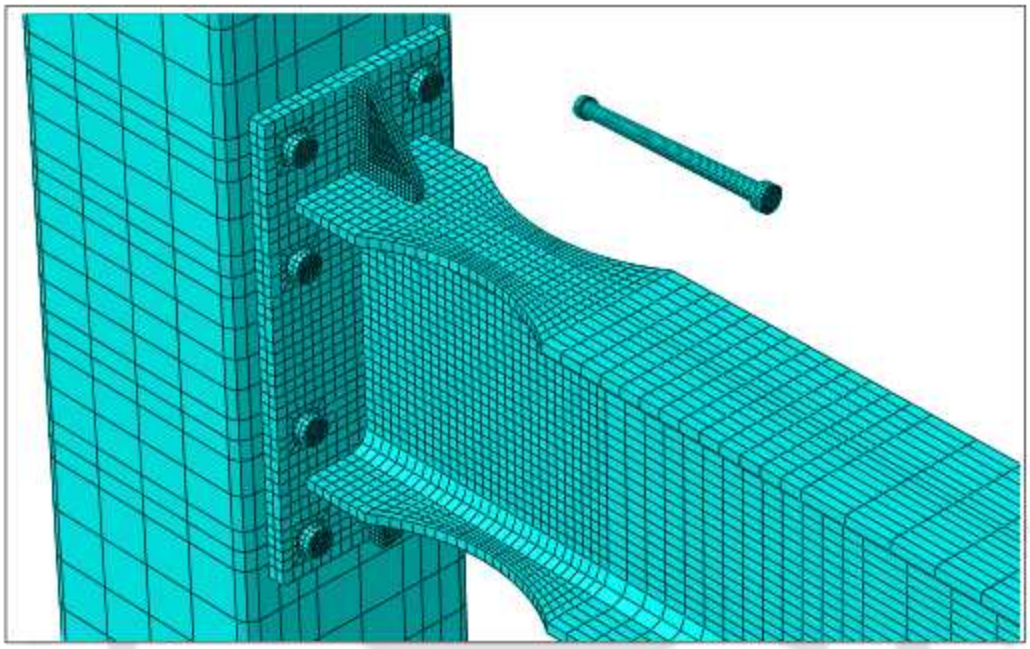

Fig. 6.5 Meshing details of radius cut RBS-CFT connection

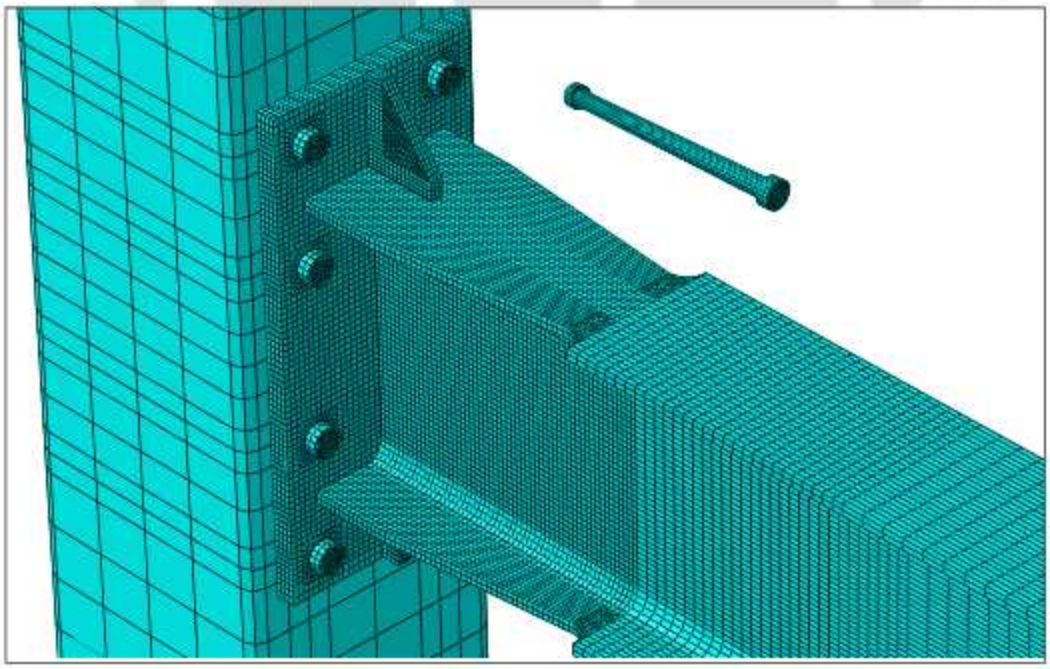

Fig. 6.6 Meshing details of *V*-cut RBS-CFT connection

***Initial boundary conditions and loading*:** The boundary conditions of the FE models simulated the support conditions imposed in the experimental study. Top and bottom end cross-section of the column were *coupled* to reference points *RP-2* and *RP-3* respectively, while the free-end

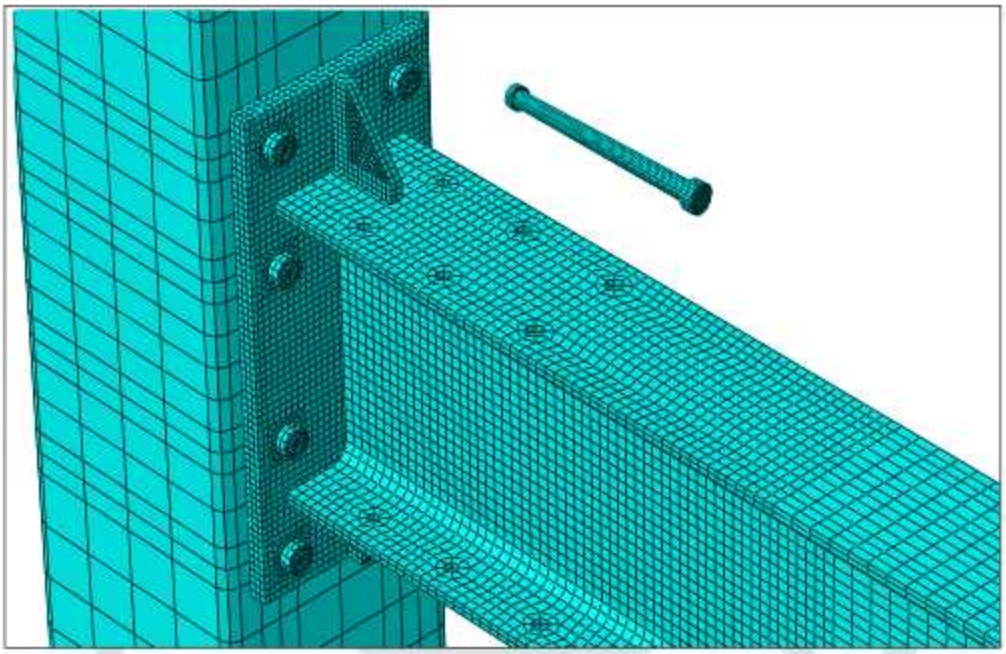

Fig. 6.7 Meshing details of *CD*-cut RBS-CFT connection

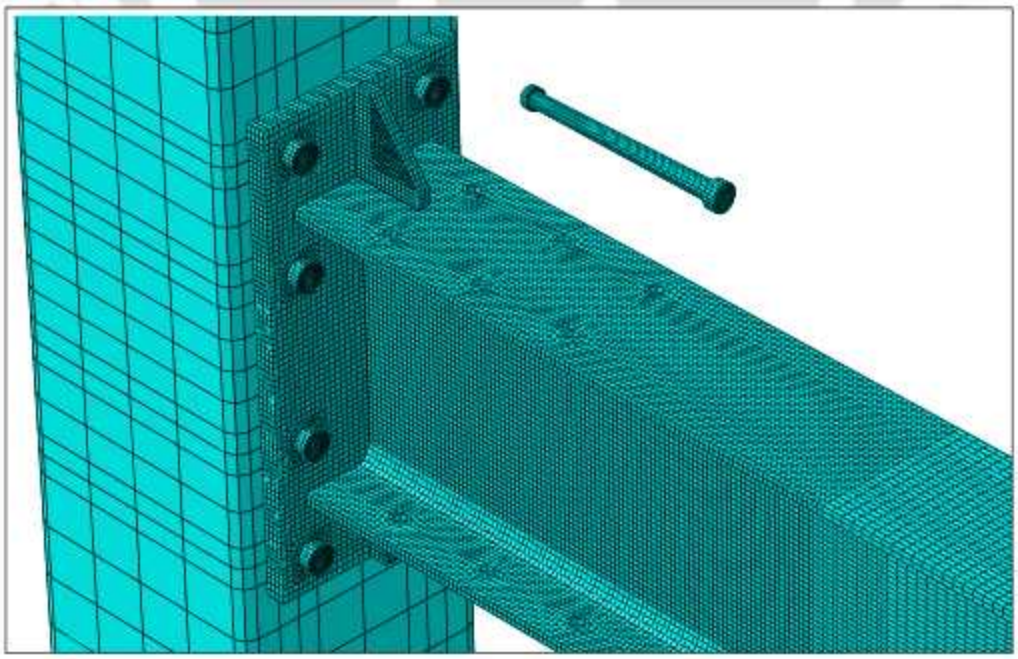

Fig. 6.8 Meshing details of *VD*-cut RBS-CFT connection

surfaces of the beam *coupled* to *RP-1*. The upper end of columns was assigned pinned boundary condition which allowed movement in the longitudinal direction of the column (i.e., $U1=U3=UR1=UR2=0$, $U2\neq0$, $UR3\neq0$). The movement in the longitudinal direction was allowed to consider the axial shortening of column due to application of an axial load on the column. The lower end of the column was also assigned pinned boundary condition, but the longitudinal movement was restrained (i.e., $U1=U2=U3=UR1=UR2=0$, $UR3\neq0$), otherwise it could cause rigid body motion.

The loading in the models were applied in two steps. In the first step apply axial loads and initial boundary conditions were imposed while in the second step was used to apply the displacement control monotonic loading was applied at the *RP-1* point in *Y* (*U2*) direction in the beam. Necessary precaution was taken to apply the monotonic load at *RP-1* point in the model. For monotonic loading, the load was generated by imposing a support displacement at the *RP-1* point of the beam. A displacement-type boundary condition was used to apply monotonically increasing displacement loading upto a maximum value of 40 mm. The postprocessor in ABAQUS automatically calculated the equivalent forces for each displacement step. Finally, based on the developed FE models the force-displacement response of the connections was computed and compared with experimental results.

***Load-displacement behaviour*:** Fig. 6.9 shows the comparison of the experimental and numerical load-displacement response of different RBS-CFT connections. The numerical load-displacement response of different RBS-CFT connection matches quite well with the experimental load-displacement envelope curves. Comparison of numerical and experimental envelope curve established that FE model develop in this study can predict the different parameters of all the RBS-CFT connections with reasonable accuracy as error varies from 0.87 % to 7.58% as shown in Table 6.2. Most of the numerical study including Elfah et al. [111], Castro et al. [112] and Silva et al. [113] for analysis of beam-column connection with bolts were carried out under application of monotonically increasing loads. Numerical analysis of bolted beam-column under cyclic loads are challenging task because of the multiple interaction and convergence issues. In view of the above, this numerical modelling technique can be adopted for further studies on RBS-CFT connections with bidirectional bolts as the predicted error varies from 1%-8%.

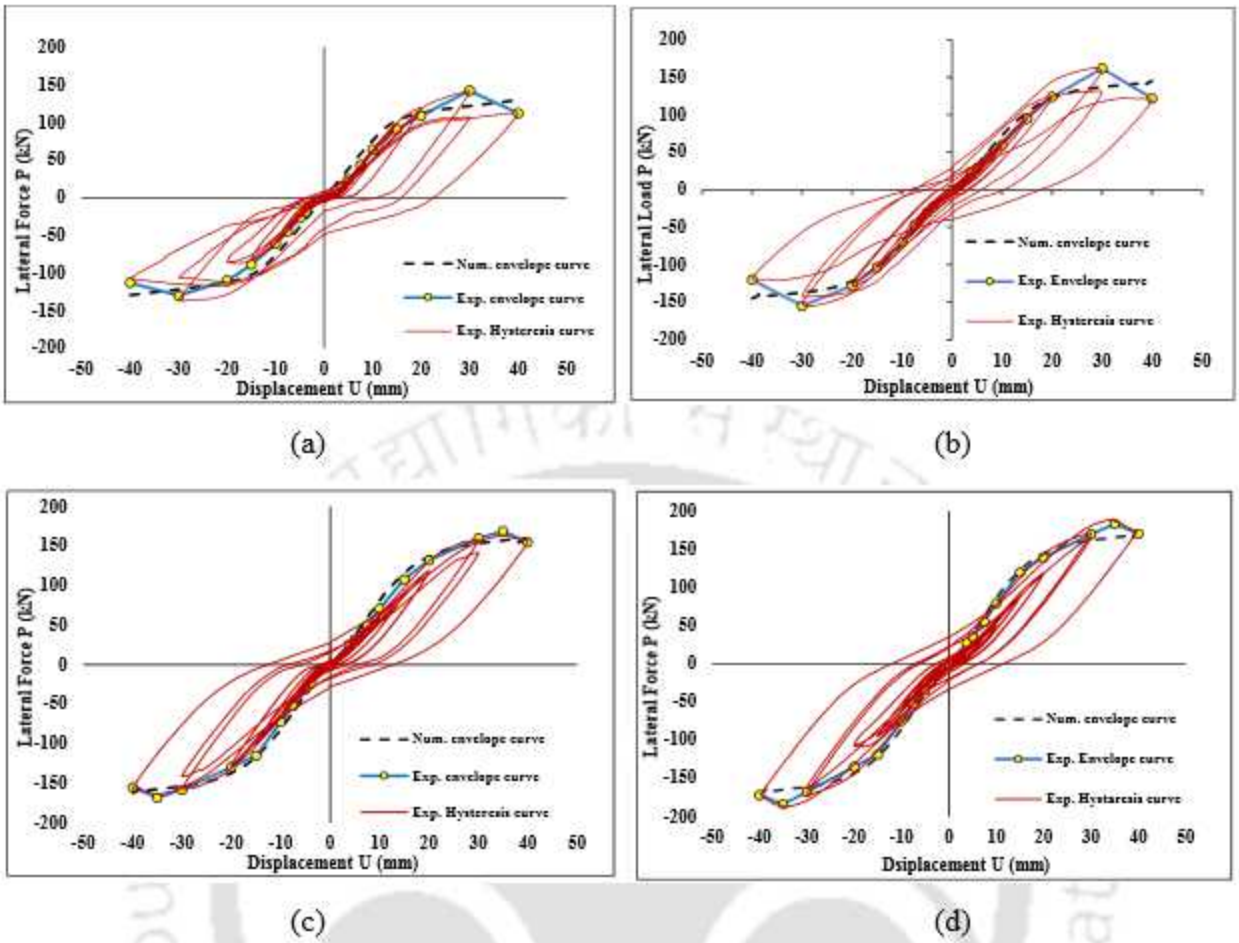

Fig. 6.9 Comparison of numerical and experimental envelope curve: (a) Radius-cut-I RBS (b) *V*-cut-I RBS (c) *CD*-cut RBS (d) *VD*-cut RBS

Table 6.2 Comparison of different parameters based on experimental and detailed numerical study

Types of RBS	Maximum loads (kN)			Initial stiffness (kN/mm)			Energy dissipated (kN-mm)		
	Exp.	Num.	Error	Exp.	Num.	Error	Exp.	Num.	Error
Radius cut-I	145	134	7.58%	4.70	5.03	7.02%	7275	7617	4.50%
V-cut-I	152	145	4.60%	5.29	5.21	1.53%	8169	8112	6.98%
CD-cut	170	165	2.94%	5.64	5.69	1.03%	8993	9086	1.02%
VD-cut	188	175	6.91%	5.83	5.81	1.02%	9624	9540	0.87%

Failure pattern of connections: One of the aims of the detailed FE simulation of RBS-CFT connection was to predict failure patterns, stress concentration at RBS zone of the RBS-CFT connection as observed in the experimental study. Fig 6.10 to 6.13 shows the damage pattern observed at various locations in the RBS zone of different RBS-CFT connections. It was observed

that FE prediction of the failure pattern matches well with the experimental observations. During the monotonic loading, the entire RBS zone yielded corresponding to 0.015 to 0.02 rad rotation. von-Mises stress distributions showed that the higher stresses were mainly located at the RBS zone area of the beam. Highest stress levels are observed at the narrowest part of the cross section. From Fig. 6.10 to Fig. 6.13, it can be observed that the numerical model was capable of simulating failure pattern similar to that observed in the experimental study. The plastic hinge formed in the RBS zone for all the RBS-CFT connection can be identified from these figures. From the Fig. 6.14, it is evident that no damage occurred in CFT column specimens. From the numerical study, it is established that reduced beam section is effective for the formation of plastic hinge away from the column, hence column and panel zone essentially remained in elastic. Hence, all the RBS-CFT connection with bidirectional bolts fulfilled the requirements of strong column weak beam concept.

6.3 Simplified numerical modelling

The simplified numerical model was created in OpenSees as shown in Fig.6.15. From the experiment, it is established that the RBS region in beam undergo yielding (plastic hinging) while the column and panel zone remain elastic. Fig. 6.15 shows the proposed simplified connection

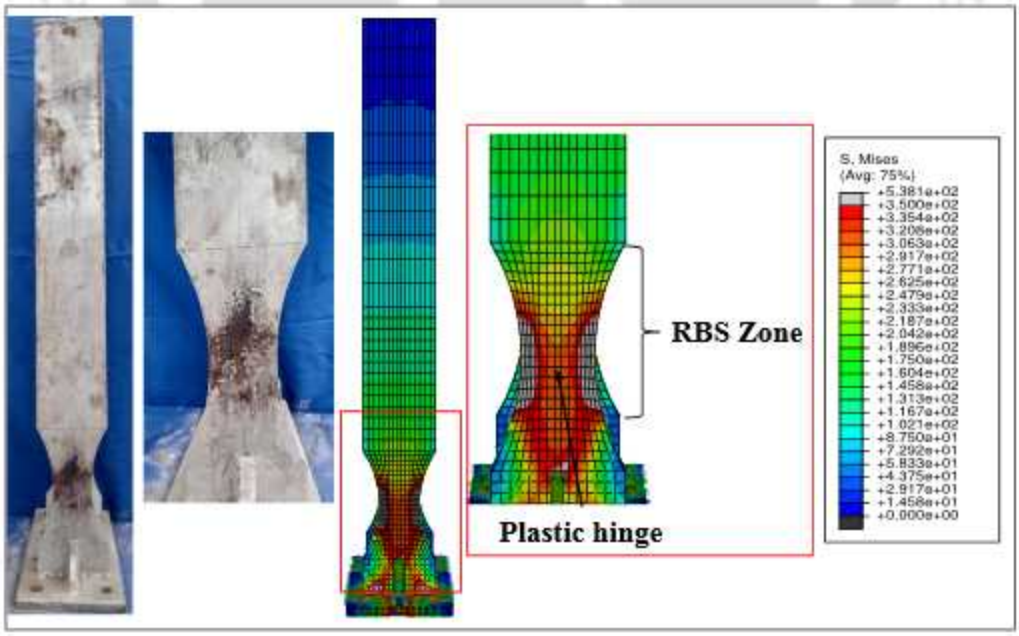

Fig 6.10 Failure patterns of radius cut-I RBS-CFT connection

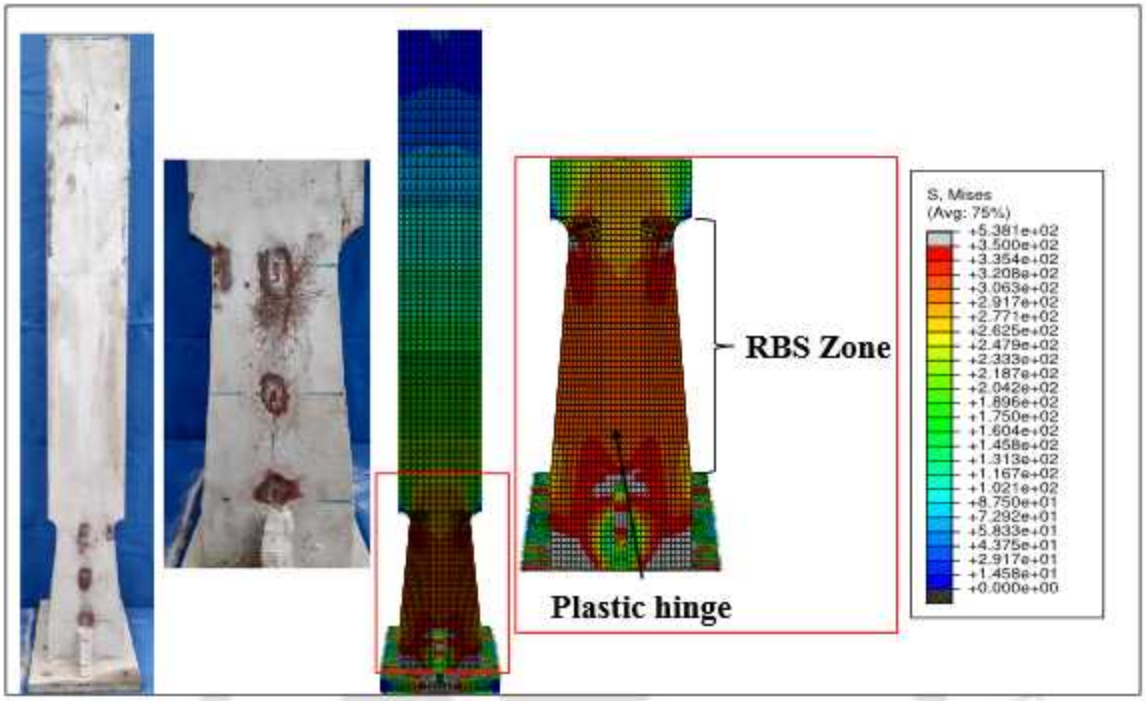

Fig 6.11 Failure patterns of *V*-cut-I RBS-CFT connection

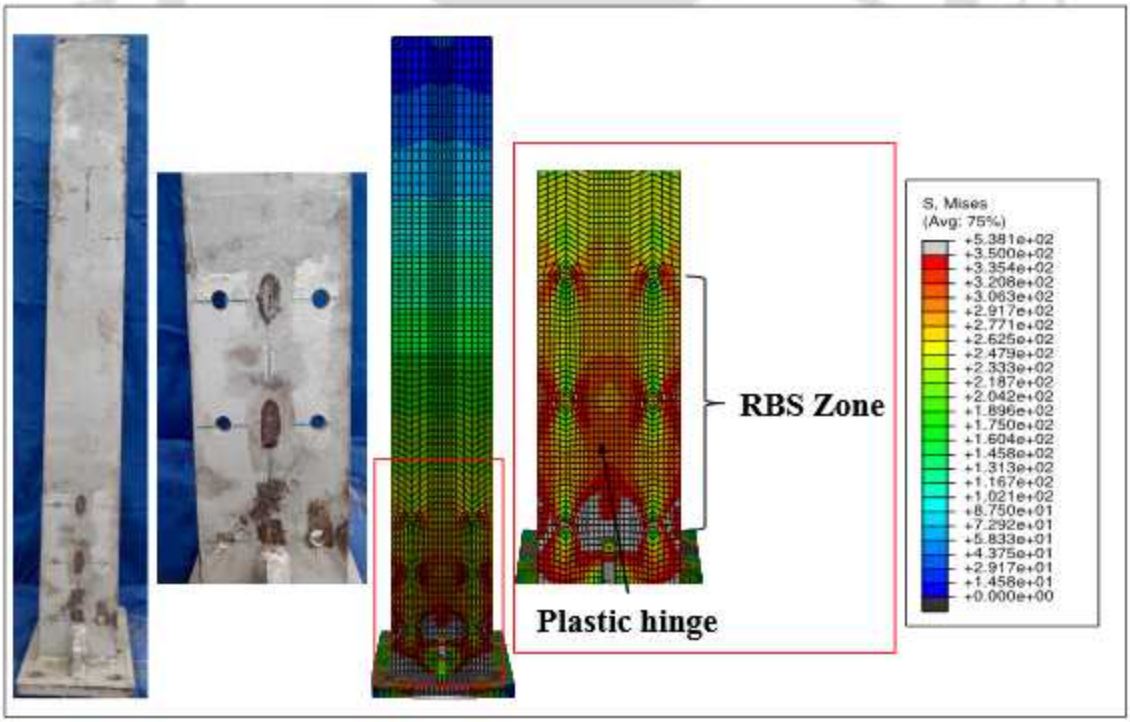

Fig 6.12 Failure patterns of *CD*-cut RBS-CFT connection

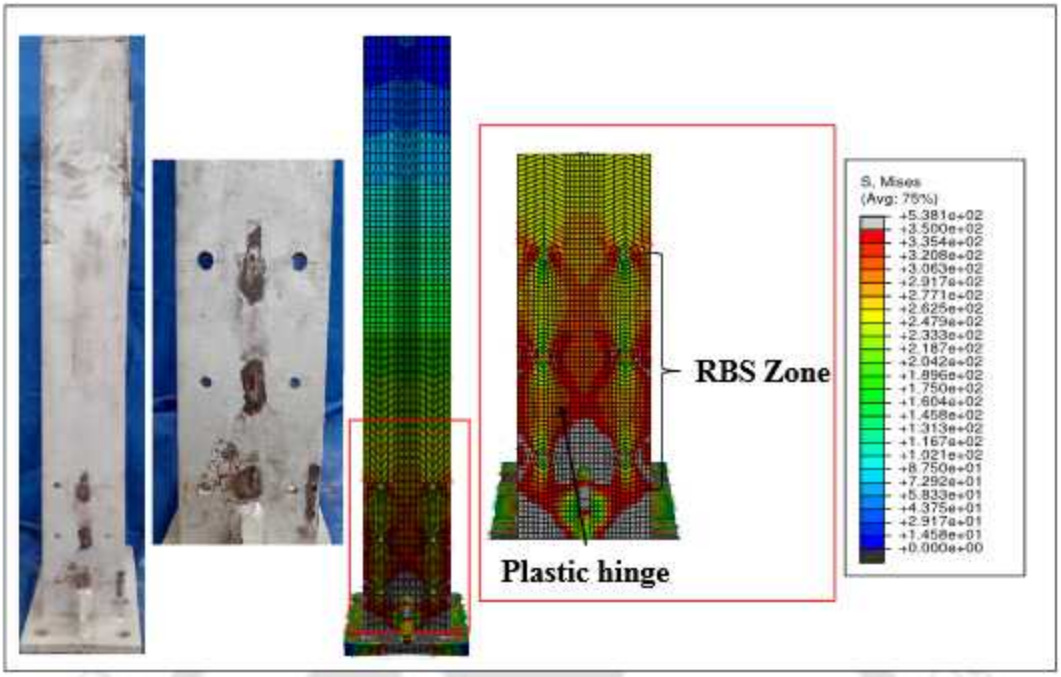

Fig 6.13 Failure patterns of *VD*-cut RBS-CFT connection

(a)

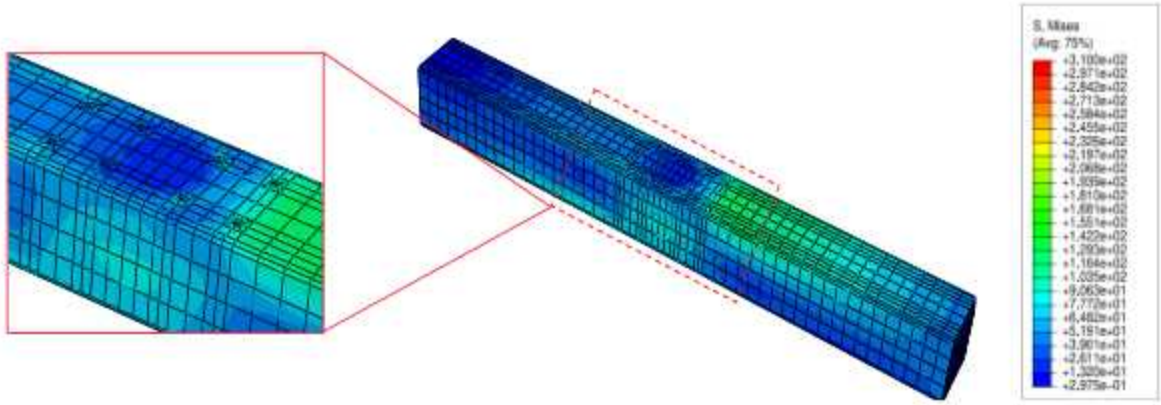

Fig 6.14 (a) Experimental test specimen (b) Dissembled simulated CFT column specimen

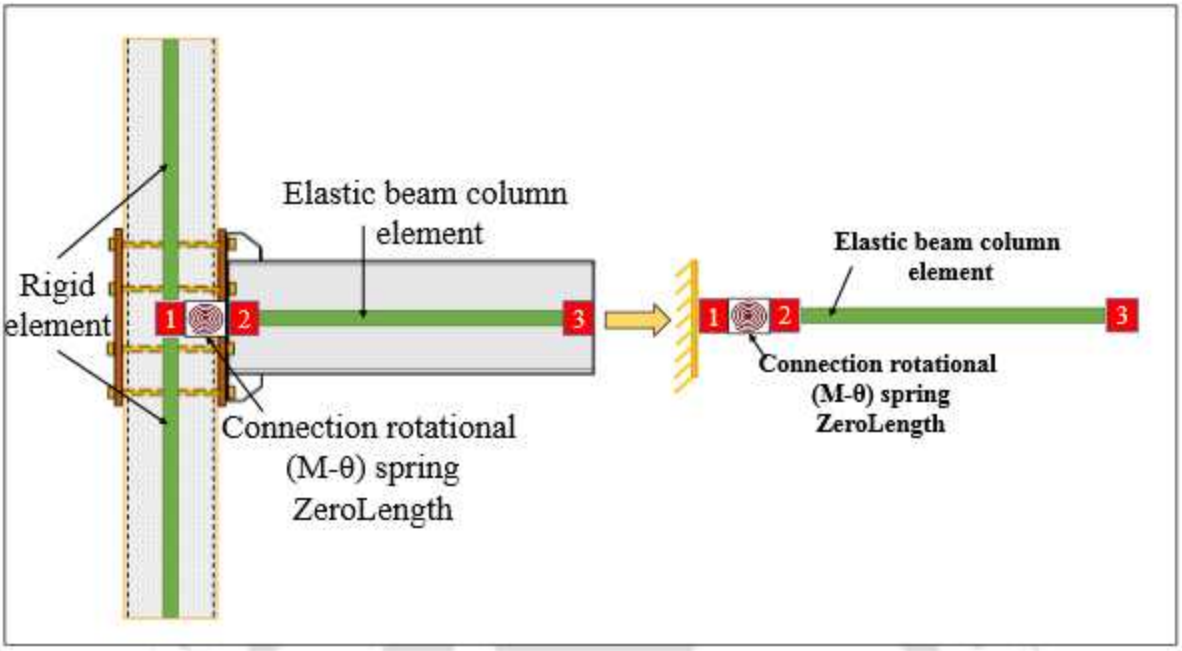

Fig.6.15 Simplified model for RBS-CFT connection

model. Panel zone, end plates, bolts and RBS zone are replaced by an equivalent rotational spring element to represent the joint region.

6.3.1 Modelling of beam-joint and rotational spring

In the OpenSees model, 2-noded an *elastic beam-column* element was used to model the beam of RBS-column connections. Nonlinearity in the connection was considered using a rotational spring between node 1 and node 2 of the connection. Concentrated plasticity (CP) approach [114] was used to model the rotational spring elements.

6.3.2 Calibration technique

The nonlinear force-deformation response behavior of the CP model relies on the behavior of the nonlinear springs (zero-length element). To make the nonlinear spring accurately simulate the cyclic behavior of the simplified model, three requirements are satisfied here: i) availability of reliable response data, which represents the cyclic behavior of the member. The target data here obtained from the experimental study. ii) selection of a proper nonlinear spring model to simulate

the nonlinear response of the member. iii) accurate and efficient calibration needed for identification of the required parameters of the nonlinear spring from the experimental data. Here, experimental force-displacement relationship was used to generate the *M-θ* response of the RBS-CFT connections. The modified Ibarra–Krawinkler–Medina deterioration model with peak-oriented hysteretic response (*ModIMKPeakOriented*) [115] was adopted to model the nonlinear springs of the CP model. The hysteresis rules defined by the model are shown in Fig. 6.16.

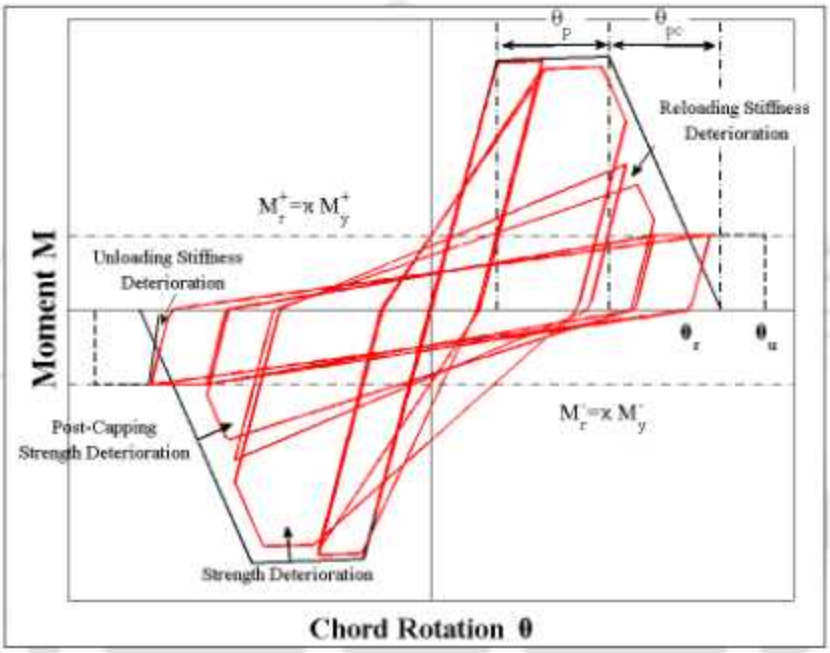

Fig. 6.16 Hysteresis rules defined by *IMK* model [114]

A backbone curve is used to limit the ultimate capacity of the nonlinear spring. The backbone curve is divided into three stages, namely a linear stage, a pre-peak stage and a post-peak stage. By defining a descending post-peak linear, the CP model is able to simulate the cyclic strength deterioration of the RBS-CFT connection. To obtain the required input parameters for the *Mod-IMK-Peak* oriented model from the experimental data, accurate and efficient calibration has been done by trial error methods. The required parameters could be grouped into two categories, namely, the backbone parameters and the deterioration parameters. The calibration of the backbone parameters is directly extracted from the envelope of the experimental data. The cyclic deterioration parameters are generated by the calibrating both bilinear model and *Mod-IMK-Peak* oriented models using web based interactive tools for performance-based earthquake engineering.

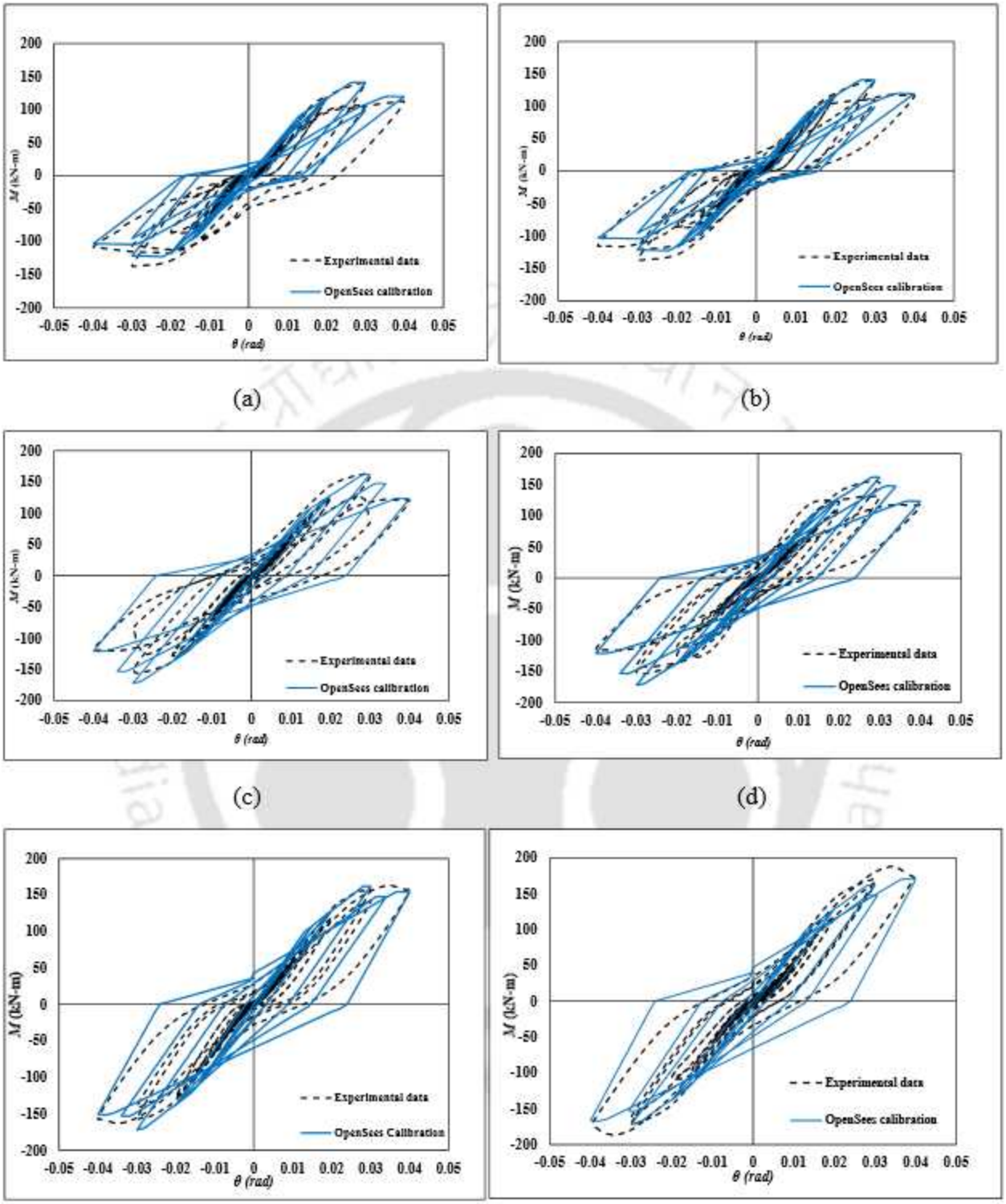

Fig. 6.17 Comparison between experimental data and calibrated data (a) Radius-cut-I (b) Radius-cut-II (c) *V*-cut-I (d) *V*-cut-II (e) *CD*-cut (f) *VD*-cut

After calculating the all parameters for the cyclic deterioration, the hysteretic response of the calibrated CP model and the experimental *M-θ* are plotted. Fig 6.17 has shown the calibrated curve for different RBS-CFT connections. A fairly good agreement between the experimental *M-θ* and the CP model prediction was observed. The elastic stiffness, the ultimate load and the backbone curve are captured well by the nonlinear spring. A similar method was adopted in several past studies [111, 116-117] for calibration and validation of numerical models.

To evaluate simulated hysteretic response of the connections under cyclic loading, cyclic horizontal displacement protocol was applied at the free end of the beam (node3). For each stage of the analysis, the reactions at node1 and nodal displacements at node3 are tabulated and thereafter, force-displacement hysteresis loops are plotted. The reaction force and nodal displacement plots obtained using OpenSees is compared with that obtained from the experiments in Fig. 6.18.

It was observed that the numerical models are reasonably good in reproducing hysteresis response similar to that obtained from the experiment. As the numerical and experimental results were in fairly good agreement, the similar simulation methods can be adopted for prototype RBS-CFT connections in steel moment resisting frames. The comparisons shown that the present FE model can predict the different parameters of all the RBS-CFT connections with reasonable accuracy as error varies from 1 % to 12% as shown in Table 6.3.

Table 6.3: Comparison of different parameters based on experimental and simplified numerical study

Types of RBS	Maximum loads (kN)			Initial stiffness (kN/mm)			Energy dissipated (kN-mm)		
	Exp.	Num.	Error	Exp.	Num.	Error	Exp.	Num.	Error
Radius cut-I	143	160	11.89%	4.70	5.03	7.02%	13639	13921	2.02%
Radius cut-II	145	160	10.35%	4.72	5.10	7.45%	13850	14036	1.32%
V-cut -I	152	158	3.94%	5.29	5.21	1.53%	15245	15542	1.92%
V-cut -II	162	158	2.47%	5.35	5.25	1.86%	15378	15120	1.67%
CD-cut	170	160	5.88%	5.64	5.69	0.87%	15022	14969	0.35%
VD-cut	188	175	6.91%	5.83	5.81	0.34%	15269	15023	1.61%

6.4 Concluding Remarks

In this chapter, numerical analysis of RBS-CFT connection with bidirectional bolts is presented. Detailed and simplified, modelling techniques were developed using two finite element software ABAQUS and OpenSees for: (*i*) The finite element analysis of RBS-CFT connections using under

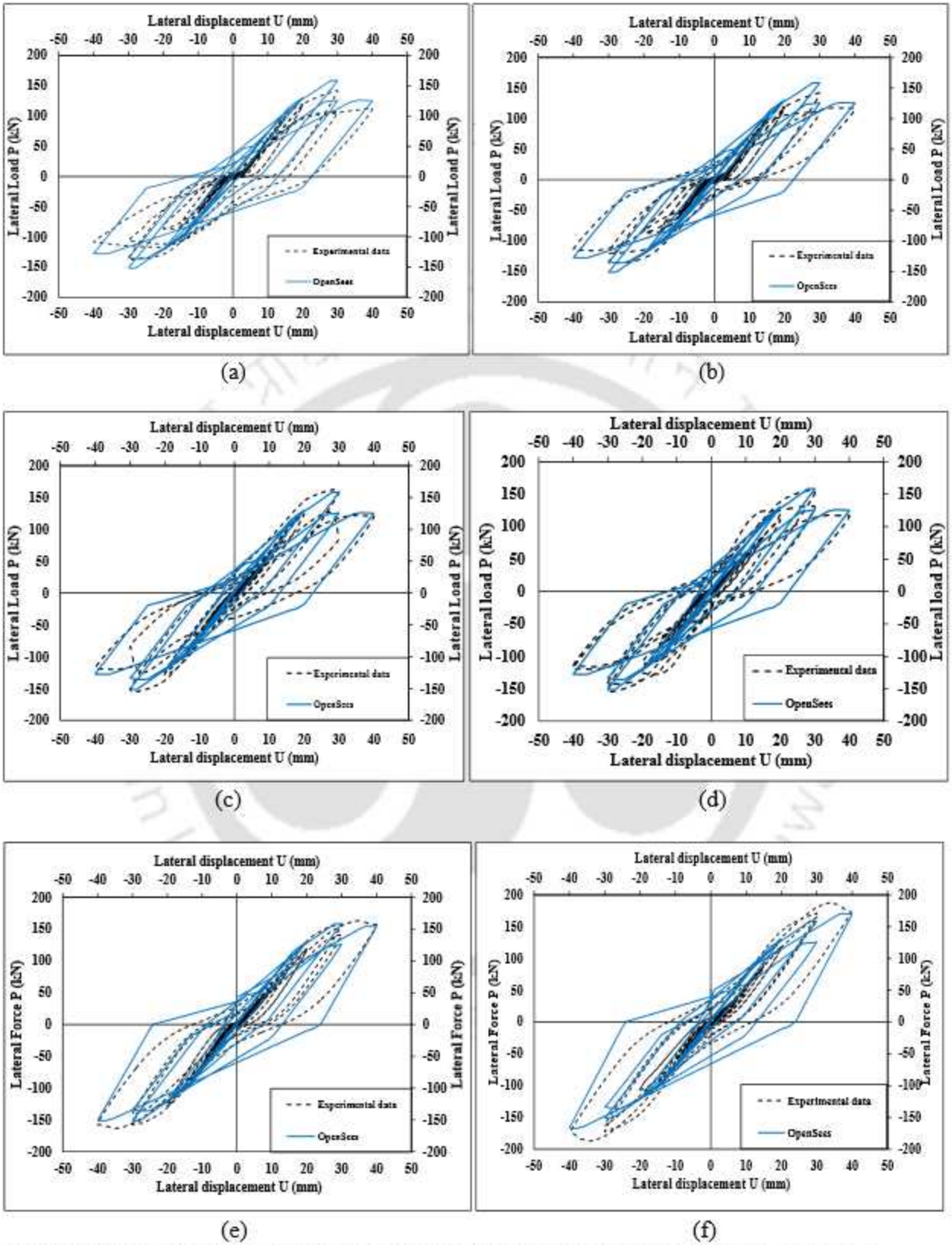

Fig. 6.18 Comparison of experimental and simulated force-displacement hysteresis loops:

(a) Radius-cut-I (b) Radius-cut-II (c) *V*-cut-I (d) *V*-cut-II (e) *CD*-cut (f) *VD*-cut

monotonically increasing load applied at beam tip for simulating their force-displacement behaviour and (*ii*) Simplified numerical analysis of RBS-CFT connection using OpenSees under cyclic loading applied at beam tip for simulating their hysteretic behaviour. The detailed finite element analysis predicts the load-displacement behaviour, failure patterns of the connections and these responses are in close agreement with that obtained experimentally. Simplified numerical models were capable to simulate the hysteretic loops of the RBS-CFT connections reasonably well as compared to that obtained from experimental study. Based on numerical study reported in this chapter following conclusion are drawn:

1. The finite element models developed in ABAQUS, satisfactorily predicted not only the lateral load-displacement response of RBS-CFT connections under monotonically increasing load but also failure patterns of the RBS specimens similar to those observed in the experiments.
2. Based on the comparison of numerical results and experimental observations, it can be concluded that the finite element can predict the failure patterns of the RBS-CFT connection. The contact interface satisfactorily predicted the expected behavior of the connection. Hence, the numerical models can be used conveniently for the study of monotonic behavior of different RBS-column connections.
3. The simplified models with the rotational springs elements simulated the hysteretic response of different types of RBS-CFT connection reasonably well under cyclic load as compared to that obtained from the experimental studies. Hence, similar kinds of modelling approaches can be used for different types RBS-CFT connections with bidirectional bolts.

CHAPTER-7

Development of Fragility Functions for RBS-column Connection

CONTENTS

7.1 Introduction

Fragility functions are developed to estimate the probability of reaching or exceeding various damage states of RBS beam-column connections as a function of engineering demand parameter (EDP). There are many ways to obtain fragility functions. Developing fragility functions from experimental data is considered to be the most reliable one among the different methods. Availability of fragility functions developed from experimental data are very limited because of time and economic constraints along with other difficulties for conducting experiments. This chapter presents the development of the fragility functions using experimental data obtained in the present study along with experimental data obtained from the literatures published since 2009. The data set consists of 20 tests on RBS moment connections. Inter-story drift ratio (IDR) considered as EDP in this study. Damage states are identified from the test reported in literatures. Four probability distributions were fit to the data, and suitability of each distribution were evaluated using standard statistical methods.

7.2 Fragility functions

Fragility functions are probability distributions that are used to indicate the probability that a component will reach or exceed a particular damage state as a function of an EDP. The mathematical form of fragility function given by Porter *et al.* [118] using lognormal distribution is defined as

$$F_i(D) = \Phi\left[\frac{\ln\left(\frac{D}{\theta_i}\right)}{\beta_i}\right] \tag{7.1}$$

where F_i (D) is the conditional probability that the component would be damaged to a damage state "i" as a function of demand parameter (D), Φ denotes the standard normal (Gaussian) cumulative distribution function, θ_i denotes the median value of the probability distribution and β_i denotes the logarithmic standard deviation. These parameters can be evaluated using the following expression (Ang and Tang, 1975).

$$\theta = \exp\left[\frac{1}{N}\sum_{i=1}^{m} \ln r_i\right] \tag{7.2}$$

$$\beta = \sqrt{\frac{1}{N-1}\sum_{i=1}^{m}(\ln\frac{r_i}{\theta})^2} \tag{7.3}$$

where N= number of samples, i = index of specimens and r_i = EDP at which damage was observed to occur in specimen i.

7.3 Engineering demand parameter (EDP)

An EDP is a measure of demand imposed by events like earthquake on a structural component. In developing fragility functions, it is important to identify an EDP that most accurately and precisely relates to damage states. Gulec *et al.* [119] reported that many researchers used IDR as a demand parameter. IDR which is defined as the ratio of beam tip displacement to the height of the floor was used as an EDP in the present study.

7.4 Damage state definitions

Damage measures provide a description of the extent of damage sustained by a component during an earthquake. The extent of damage is characterized by damage states. Thus, identification of the

appropriate damage states is the most important step for developing fragility functions. Damage states describing observed damages experienced by RBS-column connections either by visual inspections or by measurement through appropriate instrumentation. The damage states identified by Lignos et al. [120] from the results of previous experimental research were used in the present study. These damage states were assembled from the analysis of the progression of damage observed from 6 numbers of specimens tested in this study. RBS-column connections typically experienced different types of damage such as yielding, lateral torsional buckling, and fracture. Yielding may occur at various locations (e.g. at the beam flanges, the beam web), whereas buckling and fracture may occur at any parts of the connections. Two distinct damage states, DS1 and DS2 are adopted in this study. These damage states were characterized by visual observation on the damaged specimens which are presented in the following sub sections:

7.4.1 Definitions of damage states 1: (DS1)

Yielding can occur first at various locations in RBS-column connections, such as flanges or webs of beams. Strain gauges, direct current differential transformers (DCDTs), LVDTs were used to detect yielding in the flange of the beam. However, most of the studies used IDR corresponding to the strain/displacement at which yielding was initiated, for defining this damage states.

Yielding was detected from the force displacement plots provided in the literatures in case it was not recorded. Yielding in RBS-column connections occurs mainly in the beam flange. However, in this study, the first recorded incidence of yielding somewhere on the beam flange was considered to define the IDR at which this damage state was induced. Fig. 7.1(a) illustrates an example of this damage state. Table 7.1 showed the damage states and its corresponding associated drift value.

7.4.2 Definitions of damage states 2: (DS2)

This damage state was defined by cases where buckling of beam flanges were observed and occurrence of fracture was noted anywhere in the connection after yielding in the beam flange.

Table 7.1 Damage states and associated drift value:

No.	Damages states (DS)	Damages	IDR value (%)
1.	DS1	Yielding in the flange of RBS	0.075 – 0.25
2.	DS2	Torsional buckling Welding fracture between beam and end plate Lateral buckling of flange Ductile tearing with in RBS zone	0.26 – 0.50

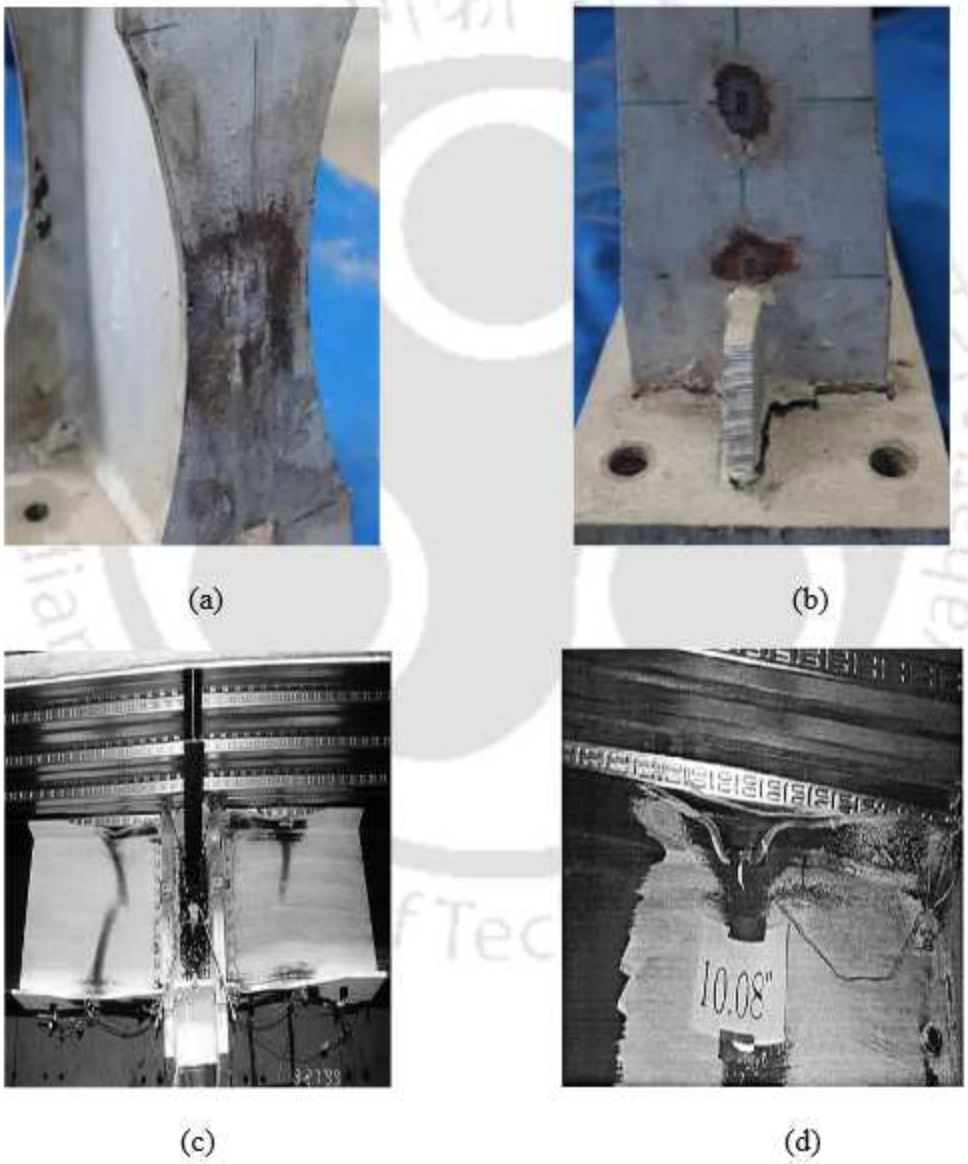

(a) (b) (c) (d)

Fig. 7.1 (a) Yielding in flange (b) Fracture between beam and end plate (Photo: S. Paul)

(c) Lateral buckling of flange (d) ductile tearing in RBS zone (Jones *et al.* [121])

Fracture can occur in various forms in RBS-column connections, like welding failure, bolt failure, ductile tearing failure etc. [122-123]. Fig. 7.1(b), Fig. 7.1(c), Fig. 7.1(d) provides an example of fracture, lateral torsional buckling and ductile tearing.

Table:7.2 Properties of RBS-column moment connections used in this study

No.	Reference source	Yield strength (MPa)	Geometry			
			Column section	Beam section	Depth (mm)	Slab
1	Li et al. [122]	350	Round426x8	H496x199x9x14	496	No
2	Li et al.	350	Round426x8	H496x199x9x14	496	Yes
3	Lee et al. [72]	385	W14x9	W24x9	609	No
4	Lee et al.	385	W14x9	W24x9	609	No
5	Lee et al.	377	W14x9	W24x9	609	No
6	Kulkarni et al. [71]	344	WPB150	NPB200	200	No
7	Parvari et al. [89]	345	Box240x200x20	W30x15	762	No
8	Parvari et al.	345	Box240x200x20	W30x16	762	No
9	Parvari et al.	345	Box240x200x20	W30x17	762	No
10	Parvari et al.	345	Box240x200x20	W30x18	762	No
11	Vajdian et al. [87]	367	Box250x250x10	IPE360	360	No
12	Vajdian et al.	367	Box250x250x10	IPE300	300	No
13	Vajdian et al.	367	Box500x500x10	IPE270	270	No
14	Vajdian et al.	367	Box250x250x10	IPE450	450	No
15	Paul & Deb [73]	350	SHS 220x220x6	NPB250	250	No
16	Paul & Deb	350	SHS 220x220x6	NPB250	250	No
17	Paul & Deb	350	SHS 220x220x6	NPB250	250	No
18	Paul & Deb	350	SHS 220x220x6	NPB250	250	No
19	Paul & Deb	350	SHS 220x220x6	NPB250	250	No
20	Paul & Deb	350	SHS 220x220x6	NPB250	250	No

7.5 Experimental results used in this study

Results of experimental research on RBS-column connections, that have been reported during the past 13 years were used to developed the fragility curves for the two damage states DS1 and DS2. The data set consists of 20 tests on RBS-column moment connections. Both types of shaved cut and drilled cut moment connections were considered. Information on each test was extracted from research papers for collection of deterioration properties of beams and columns, reported by the researchers, are presented in Table 7.2. Information about the material and geometrical properties of all specimens considered in this study is summarized in Table 7.2. IDRs corresponding to each of these two damage states were reported with respect to the centerline of the column or beam depending on whether the point of load application was at the end of the beam or column. IDRs

associated with each of the two damage states were identified. Yield strength of all structural steel beam specimens used in this study varies between 350-385 Mpa. As yielding is observed in the reduced beam zone of the RBS-column connection, the yield strength of the column is not considered for the study. Extracted M-θ data are used to verify the connection typology as per the Eq. 4.3 reported in Chapter 4. After the verification, it was observed that normalized M-θ plots are bounded between the A-line (red line) and C-line (green line), as shown in Fig 7.2. Hence all the connections are classified as semi-rigid Joint.

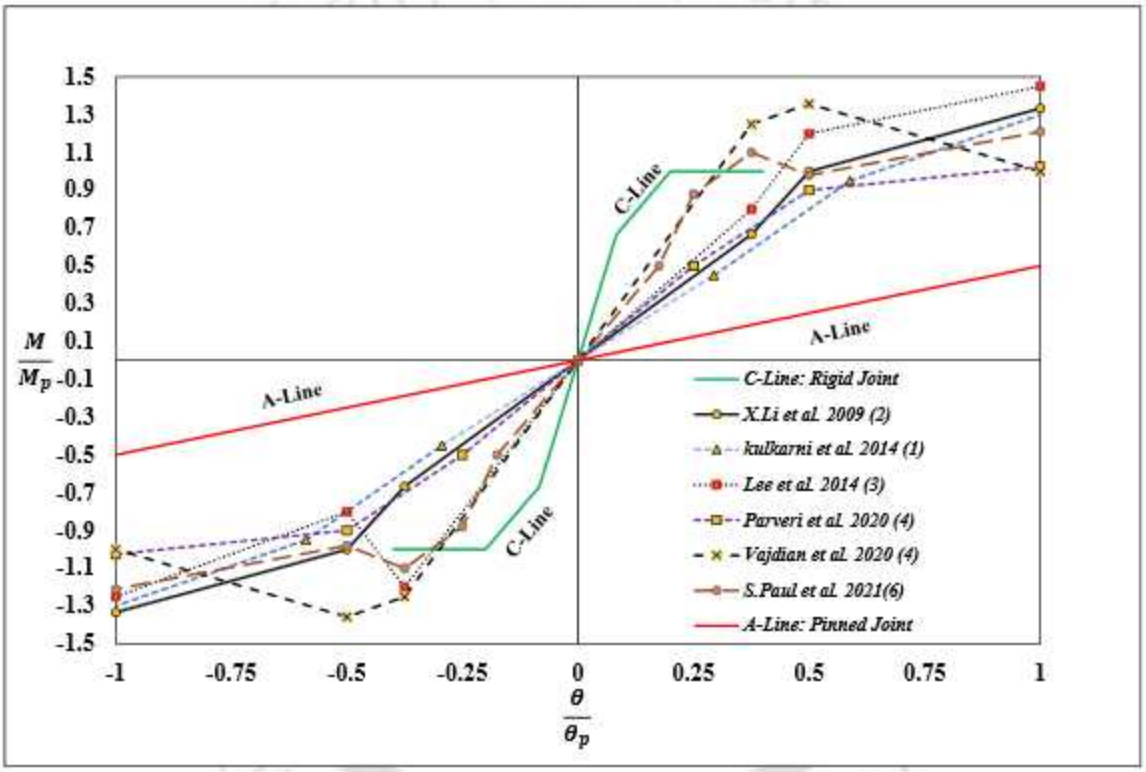

Fig. 7.2 Moment- rotation curve of reported specimens

7.6 Statistical analysis of damage data

Statistical analysis of damage data carried out to develop fragility functions for RBS-column connections. Collected data shown in the Table.7.3 were utilized to relate EDPs using standard probability distributions. The maximum likelihood method was used to fit these distributions to the data. The standard goodness-of-fit (GOF) test was performed to evaluate suitability of the considered probability distributions. Finally, most suitable distribution was identified for

development of fragility functions. Four standard probability distributions were considered to model the data. The distributions considered are lognormal, Weibull, beta (Haldar and Mahadevan [124]) and gamma distribution (Hayter [125]). Each of these probability distributions was defined by two parameters that were determined using the method of maximum likelihood. The lognormal distribution was commonly used in most fragility curve analysis.

Table 7.3 IDRs used to develop the fragility functions

Number	IDR_{DS1}	IDR_{DS2}	Number	IDR_{DS1}	IDR_{DS2}
1	0.01	0.030	11	0.0075	0.040
2	0.02	0.040	12	0.0075	0.040
3	0.02	0.040	13	0.02	0.050
4	0.02	0.040	14	0.02	0.050
5	0.02	0.040	15	0.02	0.050
6	0.01	0.035	16	0.01	0.030
7	0.01	0.035	17	0.015	0.025
8	0.01	0.035	18	0.0149	0.029
9	0.01	0.035	19	0.0152	0.030
10	0.0075	0.040	20	0.015	0.022

7.7 Evaluation of fragility functions

Shinozuka [126] was the first to introduce the hypothesis testing to evaluate the fragility functions. Once the standard probability functions have been fit to the data, standard goodness-of-fit (GOF) tests were used to evaluate how well the probability functions model the data. Two standard GOF tests were considered, namely, Kolmogorov-Smirov (K-S), the Chi-Square ($\chi 2$) tests.

7.7.1 Kolmogorov-Smirov (K-S) test

The K-S goodness-of-fit test (GOF) is a nonparametric test based on the cumulative distribution function (CDF) rather than the probability distribution function (PDF) of a continuous variable. The K-S test provides a numerical confirmation of the visual analysis for the best fit of the curve

when comparing selected distribution function. The K-S test requires the computation of the maximum difference between two CDFs (D_n) depends on the sample size n, defined as

$$D_n = \max | [\mathrm{F}_x(x_i) - \mathrm{S}_n(x_i)]| \tag{7.4}$$

$\mathrm{F}_x(x_i)$ is the CDF of the assumed distributions at the i^{th} observations of the order of sample X_i, $\mathrm{S}_n(x_i)$ is the corresponding stepwise CDF of the observed ordered samples.

GOF is determined from the comparison of the K-S parameter (D_n) to the critical value (D_n^{α}) for a selected significance level (α). The critical value is determined from a standard mathematical table where the number of data points and the significance level must be known. The significance level α is related to the probability of the K-S test parameter (D_n) as:

$$\mathrm{P}\ (D_n <= D_n^{\alpha}) = 1\text{-}\alpha \tag{7.5}$$

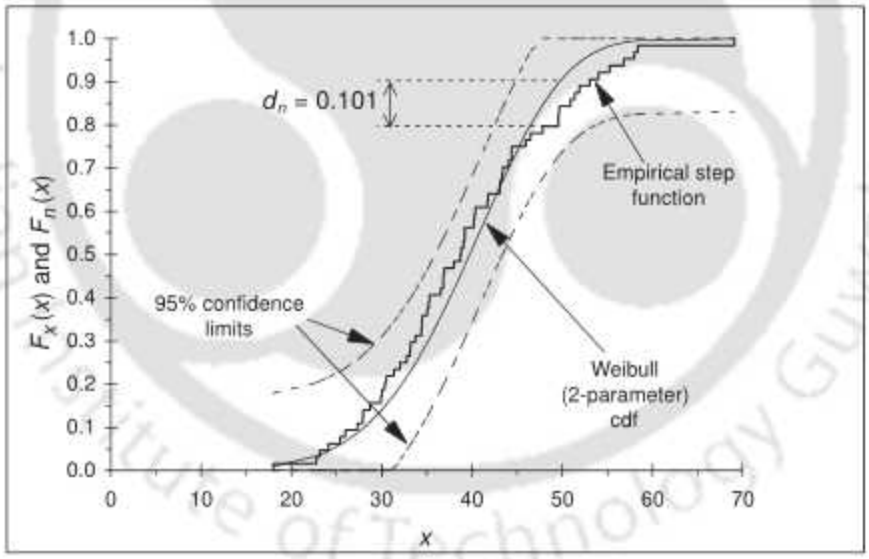

Fig. 7.3 K-S for one-sample goodness-of-fit test (Kottegoda and Rossa, [127])

According to the K-S test, if D_n is less than or equal to the tabulated value of D_n^{α}, the assumed distribution is acceptable at the significance level α. The highest probability determines the best fit distribution. A commonly used confidence level is 95%, in which the corresponding significance level is 5%. Typical K-S goodness-of-fit test for one-sample is shown in Fig.7.3.

7.7.2 Chi-square (χ^2) test

The chi-square test compares the observed and theoretical frequencies. The observed data are sub-divided into m intervals and the number of observations in each interval n_i is compared with the theoretical number of observations e_i. The theoretical distribution is acceptable at the significance level (α), if

$$\sum_{i=1}^{m} \frac{[n_i - e_i]^2}{e_i} < C_{1-\alpha f} \tag{7.6}$$

$$f = m\text{-}k\text{-}1 \tag{7.7}$$

where $C_{1-\alpha f}$ is the value of the χ^2 distribution, $f =$ is the degree of freedom, K is the number of parameters in the distribution which is two for all distributions. In applying the χ^2 test, it is desirable that the numbers of interval (m) and the number of observation (e_i) should be at least 5 for satisfactory results [127] and the total number of data points should exceed 50 (Kottegoda and Rosso) [128].

K-S test have the advantage over the χ^2 test as it is not necessary to divide collected data into number of interval (m). Thus, the error of judgement associated with the number or size of the distribution could be avoided.

7.8 Development of fragility functions for RBS connections

Identification of DS was done based on recommendation of the paper by Lignos *et al.* [129] and observations made during experiments for different levels of EDPs. All the collected damaged states (DS) were used for the development of fragility functions. Cumulative frequency distribution function was obtained by plotting demand parameter in ascending order for a given damage state which was observed during experiment against $\left[\frac{i-0.5}{n}\right]$, where i^{th} is the position of the drift level within the sorted data and n is the number of samples. This derived cumulative

frequency distribution functions provides the data set which does not exceed a particular value of demand. Four probability distribution functions were fitted to the derived cumulative frequency distribution functions in order to evaluate best fit probability distribution.

7.9 Fragility functions for the damage states

Fragility functions corresponding to four selected probability distributions for two damage states are shown in Fig 7.4 and Fig.7.5 respectively. It is observed that each of the distributions provide nearly similar good fit to the data. Graphical representation of the K-S goodness-of-fit test for 5% significance levels has also been shown in the Fig.7.4 and 7.5. The best distribution was determined using the K-S test where the parameter (D_n) or the error was evaluated. The error was compared to a critical value (D_n^{α}) for the selected significance level of 5%. The values D_n^{α} were obtained from Table VI [124]. Distribution providing highest probability was considered as the best fit distribution, in which the error was less than the critical value. The complete results of K-S test are furnished in Table 7.4. It may be concluded that each of the distribution functions provided comparable good fit to the data. However, the lognormal distribution provided the best fit among all the selected distributions when the critical values for each of the distributions were compared. The Chi-square GOF test method was also used in the present study. The results of Chi-square test are furnished in Table 7.5. The critical values were obtained from Tables II [125]. where the result of ($C_{1-\alpha,\ f}$) was found to be 5.991 in both the cases. The values furnished in Table 7.5 indicate that the Chi-Square value (error) is smaller than the Chi-Square critical value for degree of freedom (f) 2 in both cases. However, the lognormal distributions provided best results among all the distributions considered in the study.

The above GOF tests showed that each of the distribution functions provides comparable good fit to the data. However, the lognormal distribution provided the best fit among all the distributions. As mentioned earlier, many researchers [130, 131] developed fragility functions based on experimental results using different probability distributions. It was reported that lognormal distribution is the best fit for variety of structural component failure. In this study also, it was observed on the basis of GOF test that each of the distribution provides comparable good fit to the data.

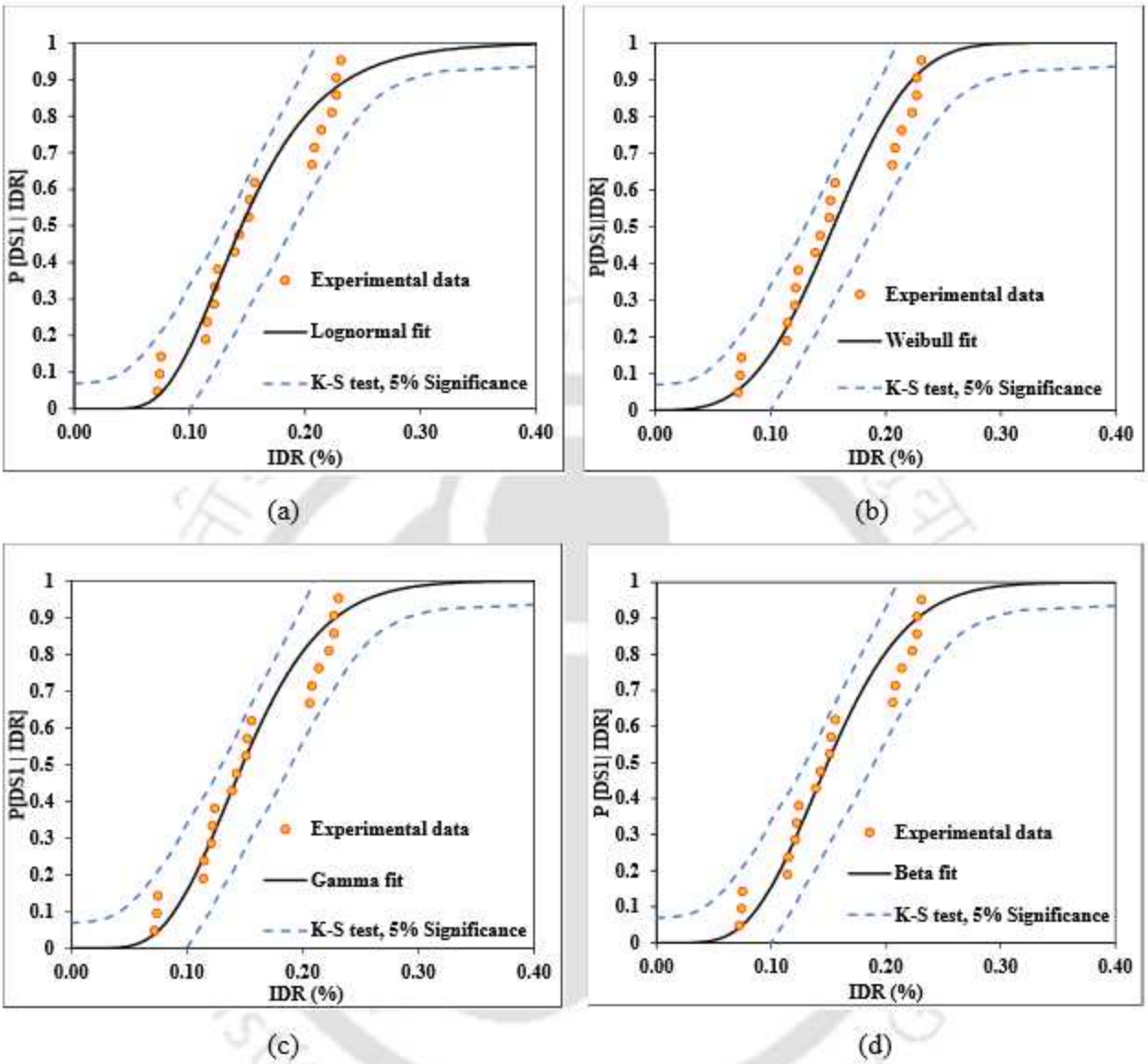

Fig. 7.4 Fragility functions for damage states DS1 defined by four probability distributions: (a) lognormal (b) Weibull (c) gamma and (d) beta.

But the lognormal distribution provided the best fit among all the distributions. Therefore, the lognormal distribution was chosen as the preferred distribution because (i) the lognormal distribution is commonly used for definition of fragility function and (ii) GOF test results indicates that lognormal distribution provided the best fit among all the distributions.

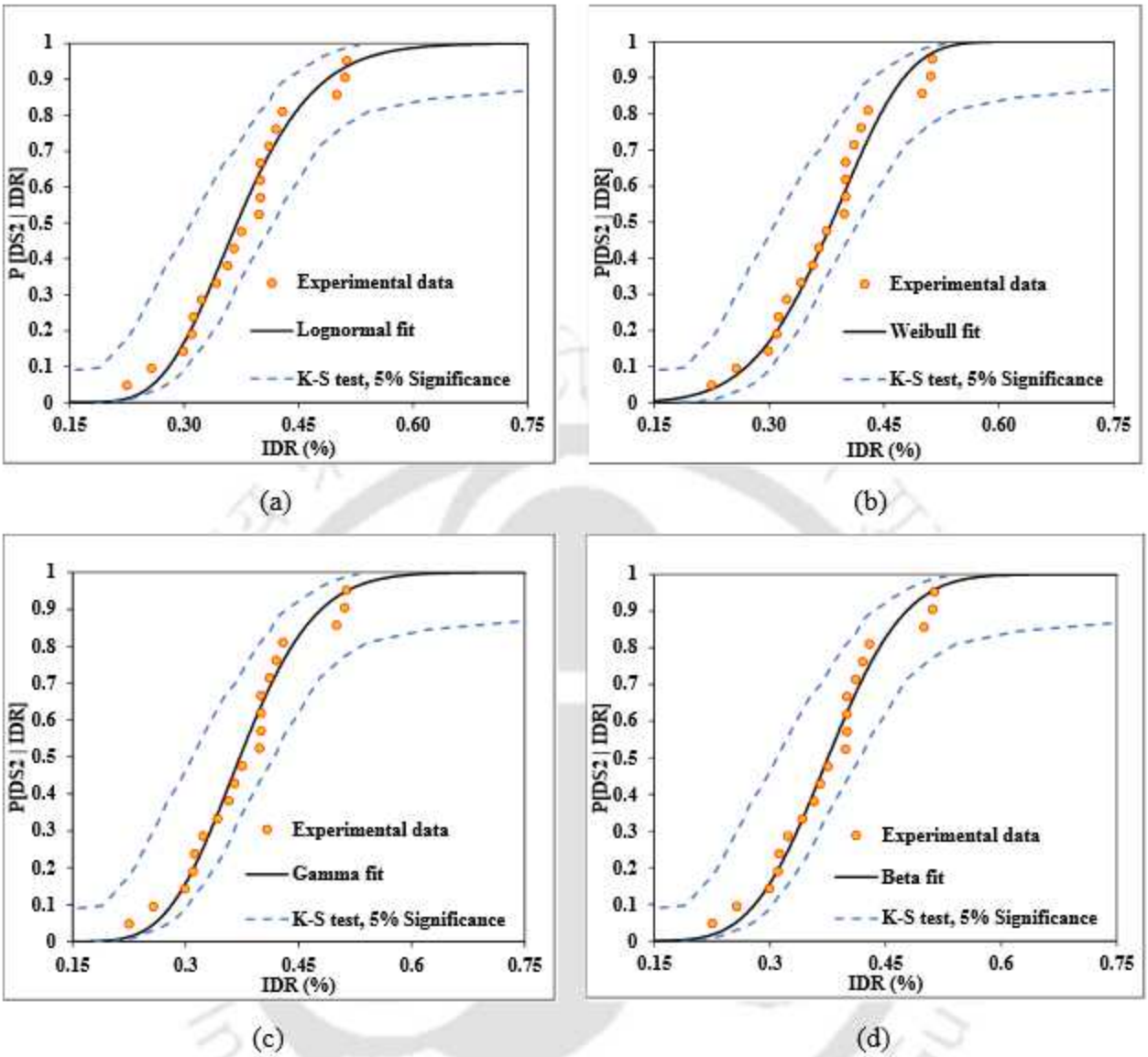

Fig. 7.5 Fragility functions for damage states DS2 defined by four probability distributions: (a) lognormal (b) Weibull (c) gamma and (d) beta.

7.10 Concluding remarks

In this chapter, fragility functions for exterior RBS-column semi-rigid connections were developed considering the experimental data obtained in the present study along with data collected from the past studies. The results of the study indicate that the probability of beginning of initial yielding, i.e. DS1, occurring at an IDR ranges from 0.10% to 0.25%, whereas the probability of lateral-torsional buckling, i.e. DS2, occurring at an IDR ranges from 0.30% to 0.50%. Four standard

Table 7.4 K-S test results for selected distributions for experimental data

		IDR_{DS1}	IDR_{DS2}
Sample size	n	20	20
Critical Value (D_n^{α})	$\alpha = 0.05$	0.294	0.294
Lognormal distribution	Median (θ)	0.917	2.758
	Std. deviation (β)	0.598	0.457
	K-S parameter (D_n)	0.102	0.101
	$P(D_n \leq D_n^{\alpha})$	0.928	0.961
Gamma distribution	Parameter (λ)	0.365	0.887
	Parameter (k)	1.650	2.740
	K-S parameter (D_n)	0.109	0.103
	$P(D_n \leq D_n^{\alpha})$	0.902	0.957
Weibull distribution	Parameter (w)	1.150	2.660
	Parameter (q)	0.810	0.863
	K-S parameter (D_n)	0.120	0.110
	$P(D_n \leq D_n^{\alpha})$	0.842	0.941
Beta distribution	Parameter (r)	1.370	1.231
	Lower bound (a)	0.210	2.293
	Lower bound (b)	2.400	7.580
	K-S parameter (D_n)	0.182	0.168
	$P(D_n \leq D_n^{\alpha})$	0.801	0.896

Table 7.5 Chi-square test results for selected distributions for experimental data

Distributions		IDR_{DS1}		IDR_{DS2}		Degree of freedom
		Error	P	Error	P	
lognormal	$\sum_{i=1}^{m} \frac{(n_i - e_i)^2}{e_i}$	1.286	0.525	0.692	0.824	2
Gamma		1.395	0.485	0.717	0.807	2
Weibull		1.585	0.425	1.388	0.793	2
Beta		1.681	0.402	1.415	0.715	2
Critical Value	$C_{1-\alpha f}$					5.991

Note: P $(D_n \leq D_n^{\alpha})$ = P

probability distributions were used to model data. The results of the GOF test showed that each of the distributions provided comparable fit to the data. However, in general the lognormal distributions provided the most acceptable when compared to the critical values for each of the damage states. Therefore, experimental fragility function for semi-rigid RBS-column connection developed in the present study would be useful for seismic vulnerability assessment of steel MRFs.

CHAPTER-8

Summary, Conclusions and Future work

CONTENTS

8.1 Summary

In the present study, the seismic performances of exterior RBS-CFT connection with bidirectional bolts under cyclic loading were evaluated and documented in terms of various parameters such as hysteretic load carrying capacity, stiffness degradation, energy dissipation, displacement ductility etc. Four different types of RBS-CFT connections with bidirectional bolts under were considered, namely, (a) Radius cut RBS-CFT connection (b) *V*-cut RBS-CFT connection (c) *CD*-cut RBS-CFT connection (d) *VD*-cut RBS-CFT connection. Geometrically similar specimens with radius cut, *V*-cut, *CD*-cut and *VD*-cut RBS were tested under cyclic loading for evaluation of their seismic performances.

The test setup was designed and fabricated for carrying out cyclic testing of specimens in the dynamic structural testing laboratory at IIT Guwahati. Servo hydraulic dynamic actuator of capacity 250 kN having a maximum displacement range of ± 250 mm was used for application of cyclic displacement histories. Displacement loading histories were applied as prescribed by AISC 341 (16).

Two types of strain sensors were used to record the strain values of the RBS zone of RBS-CFT connection. Reusable strain gauges were placed diagonally to record the strain value of panel zone of CFT. Foil type strain gauges were used to record the strain value of reduced zone of the beam. An inclinometer was used to measure beam rotation of the RBS-CFT connection.

All specimens of each types of RBS-CFT connections were tested under simultaneous action of axial load in CFT and cyclic load at the beam ends. All the test specimens attained maximum rotation of 0.04 rad as per AISC (2016) criteria for special moment resisting frames. All relevant mechanical characteristics of all types of RBS-CFT connections are calculated and reported. Force-displacement hysteresis loops of all the specimens of each types of RBS-CFT connections are used to find the different mechanical characteristics.

Recorded data was used to study hysteretic behaviour, envelope curve, stiffness degradation, energy dissipation capacity, strain distribution, ductility for all the RBS-CFT connections. In terms of the above-mentioned parameters, seismic performance of RBS-CFT connections were analysed to arrive at the important conclusions. It was observed that *V*-cut RBS had higher ductility and energy dissipating capacity as compared to these of the radius cut RBS whereas varied drilled cut (*VD*-cut) RBS had marginally higher energy dissipation capacity and stiffness as compared to these of the constant drilled cut (*CD*-cut) RBS. It was observed that the plastic hinges are formed in the RBS zone of the connections, whereas the column and panel zone area remained elastic at all times.

Nonlinear finite element analysis of RBS-CFT connections with bidirectional bolts was performed using the general-purpose software ABAQUS (v 6.6-1, 2006) and OpenSees (v.17.7.3, 2006). The failure patterns of the connections were identified by the ABAQUS software. Force vs. displacement behaviour under increasing monotonic load were simulated for the all the connections which were then compared with those obtained from the experimental study. Simplified model was proposed in OpenSees platform to simulate hysteresis loops these were then validated by comparing the same with those obtained from the experimental study.

Fragility function were developed for the semi-rigid RBS-column connections. Developing the fragility functions from experimental studies were considered to be the most reliable one among the different approaches. Here, development of fragility functions carried out using experimental data recorded in the present study and experimental data collected from past studies. Two damage states were considered. Four probability distribution functions were used to fit the data. Goodness of fit test were conducted to find the best fit distributions. Finally, it was reported that lognormal distributions were best fit distribution for both the damages states.

8.2 Conclusions

In this study, two different class of RBS-CFT connections are studied. (*i*) shaved cut RBS-CFT connections (*ii*) drilled cut RBS-CFT connections are studied. Following major conclusions can be drawn from the exhaustive experimental, numerical, and statistical study:

1. Proposed *V*-cut RBS-CFT connection have higher load carrying capacity, marginally higher ductility and stiffness as compared to those parameters of radius cut RBS-CFT connection.
2. Residual torsional deformation experienced by the connection with *V*-cut RBS is less as compared to that of the connection with radius cut RBS.
3. Energy dissipation capacity was 12-13% more in *V*-cut RBS, due to the increase of plastic hinge length, as compared to that of the radius cut RBS.
4. *VD*-cut RBS-CFT connection have higher load carrying capacity, stiffness and similar order of ductility as compared to those parameters of the *CD*-cut RBS.
5. Residual torsional deformation is less for the *VD*-cut RBS due to the lower drill size close to beam-column interface as compared to that of the *CD*-cut RBS
6. Energy dissipation capacity was marginally high in case of *VD*-cut RBS, due to the increase of plastic hinge length as compared to that of the *CD*-cut RBS.
7. Adopted design for all the RBS-CFT connection fulfilled the requirements of strong column-weak beam concept as no damage was observed in panel zone or CFT.
8. All the RBS-CFT connection achieved a rotational capacity of 0.04 radians without any damage in the joint panel region, and thereby meets the seismic provisions of the AISC prescribed for a special composite moment-resisting frame.
9. All types of the RBS-CFT connections were found to be semi-rigid in nature which would ensure their ductile behavior.
10. The developed FE models in ABAQUS were found to be satisfactory in predicting the lateral load-displacement behaviour of RBS-CFT connections with bidirectional bolts. The

developed FE models were capable of predicting the peak response of the RBS-CFT connection as well as failure patterns in all the connections.

11. The simplified model in OpenSees was capable to simulate the force-displacement hysteretic loops for all types of RBS-CFT connections. Numerically simulated and experimental force-displacement hysteresis loops for all types of connections were found to be in good agreement.
12. Experimental fragility function for semi-rigid RBS-column connection developed in the present study would be useful for seismic vulnerability assessment of steel MRFs

8.3 Scope of future work

In this study experimental and numerical investigations are carried out to evaluate the seismic performance of RBS-CFT connection with bidirectional bolts under cyclic loads. Experimental and numerical study was reported for the evaluation of seismic behavior. The results of the study highlight the significant conclusions for RBS-CFT connections with bidirectional bolts. However, future research directions can include the following:

1. The effect of the concrete slab on the behavior of the RBS-column frames can be investigated by conducting experimental study.
2. Different sizes of RBS-CFT connection specimens were considered for size effect investigation for better acceptability of results.
3. The advanced numerical modelling technique can be extended by considering the interaction properties of bolts and concrete in the micro level for simulation of hysteresis loops obtained from experimental study.
4. Non-linear time history analysis may carried out for evaluation of seismic response of the composite moment resisting frames with different types of RBS-column connections.

References:

[1] R. S. M Brunaeu, C. Uang, *Ductile Design of Steel Structures*, Second Edi. The McGraw-Hill Companies, Inc, 2011.

[2] FEMA. (2000), "Recommended Seismic Evaluation and Upgrade Criteria for Existing Welded Steel Moment-Frame Buildings," *FEMA-351*, 2000.

[3] Chen, S.J., Chu, J. M. and Chou, Z. L. "Dynamic Behavior of Steel Frames with Beam Flanges Shaved Around Connection," 1997.

[4] Engelhardt, M. D. and Sabolt, T. A. "Seismic-resistant steel moment connections: developments since the I994 Northridge earthquake the pre-Northridge connection," *Prog. Struct. Eng. Mater.*, vol. 997, no. I, pp. 68–77.

[5] A. Plumier, "New idea for safe structures in seismic zones," 1990, doi: 10.5169/seals-46518.

[6] Chen, S.J., and C.H. Yeh, "Enhancement of ductility of steel beam-to-column connections for seismic resistance." In SSRC Task Group Meeting & Technical Session. Lehigh University. Pennsylvania

[7] Popov, E. P., Yang, T. S. and Chang, S. P. "Design of steel MRF connections before and after 1994 Northridge earthquake," *Eng. Struct.*, vol. 20, no. 12, pp. 1030–1038, 1998, doi: 10.1016/S0141-0296(97)00200-9.

[8] D. K. Miller, "Lessons learned from the Northridge earthquake," *Eng. Struct., vol.20, no. 4-6, pp.249-260,*1998, doi:10.1016/S0141-0296(97)00031-X.

[9] FEMA. (2000), "Recommended Seismic Design Criteria for New Steel Moment-Frame Buildings," *FEMA 350*.

[10] Zhou, G., Yonghui, A., Wu, Z., Dongsheng Li; and Jinping Ou. "Analytical Model for Initial Rotational Stiffness of Steel Beam to Concrete-Filled Steel Tube Column Connections with Bidirectional Bolts", Journal of Structural Engineering, ASCE, Vol. 144 (11), (2018).https://doi.org/10.1061/(asce)st.1943-541x.0002187

[11] Feizi, M. Gholipour., Mojtahedi, A. and Nourani, V. "Effect of semi-rigid connections in improvement of seismic performance of steel moment-resisting frames." Steel and Composite Structures, *Vol. 19, No. 2 (2015) 467-484.* doi: http://dx.doi.org/10.12989/scs.2015.19.2.467.

[12] Mirza, O. and Uy, B. "Behaviour of composite beam-column flush end-plate connections subjected to low-probability, high-consequence loading", Engineering structure, 33(2), (2011) 647-662. https://doi.org/10.1016/j.engstruct.2010.11.024.

[13] Agheshlui, H., H. Goldsworthy, E. Gad, H. Yao. "Tensile behavior of groups of anchored blind bolts within concrete-filled steel square hollow sections." Journal of Structural Engineering 142 (2): (2016) 04015125. https://doi.org/10 .1061/(asce)st.1943-541x.0001388.

[14] Wang, Z. Y., W. Tizani, Q. Y. Wang. "Strength and initial stiffness of a blind-bolt connection based on the T-stub model." Engineering structure 32 (9): (2010) 2505–2517. https://doi.org/10.1016/j.engstruct.2010.04.005.

[15] Tao, Z., W. Li, B. L. Shi, L. H. Han. "Behaviour of bolted end-plate connections to concrete-filled steel columns." Journal of Constructional Steel Research 134: (2017) 194–208. https://doi.org/10.1016/j.jcsr.2017.04.002.

[16] Yao, H., H. Goldsworthy, E. Gad. "Experimental and numerical investigation of the tensile behavior of blind-bolted T-stub connections to concrete-filled circular columns." Journal of Structural Engineering 134 (2): (2008) 198–208. https://doi.org/10.1061/(ASCE)0733-9445(2008)134:2(198).

[17] Wu, L. Y., L. L. Chung, S. F. Tsai, C. F. Lu, G. L. Huang. "Seismic behavior of bidirectional bolted connections for CFT columns and H-beams." Engineering structure 29 (3): (2007) 395–407. https://doi.org/10.1016/j .engstruct.2006.05.007.

[18] Rahnavard, R., Hassanipour, A., and Siahpolo, N. Analytical study on new types of reduced beam section moment connections affecting cyclic behavior. Case Studies in Structural Engineering, 3, (2015), 33-51. https://doi.org/10.1016/j.csse.2015.03.001.

[19] Mahin, S. A. "Lessons from damage to steel buildings during the Northridge earthquake." Engineering structure 20 (4): (1998) 261–270. https://doi.org/10.1016/S0141-0296(97)00032-1.

[20] Popov, E.P., Yang, T. S. and Chang, S. P. "Design of steel MRF connections before and after 1994 Northridge earthquake," *Eng. Struct.*, vol. 20, no. 12, pp. 1030–1038, 1998, doi: 10.1016/S0141-0296(97)00200-9.

[21] Kim, T., Whittaker,A. Bertero,S. Takhirov,V. S. M. Whittaker, A. S. and Gilani,A. S. J. "Cover-Plate and Flange-Plate Reinforced Steel Moment-Resisting Connections Cover-Plate and Flange-Plate Reinforced Steel Moment-Resisting Connections." Journal of Structural Engineering 134 (2): (2013) 198–208. 2000.

[22] Whittaker,C. O. A. Gilani,A. Takhirov, S. "Forensic Studies of a Large Cover-Plate Steel Moment-Resisting Connection," *Struct. Des. Tall Build.*, vol. 11, pp. 265–283, 2002, doi: 10.1002/tal.200 forensic.

[23] Zaghi, A. E. Soroushian,S. Itani,A. Manos Maragakis, E. Pekcan,G. and Mehrraoufi, M. "Impact of column-to-beam strength ratio on the seismic response of steel MRFs," *Bull. Earthq. Eng.*, vol. 13, no. 2, pp. 635–652, 2015, doi: 10.1007/s10518-014-9634-9.

[24] Zuo, H. Z. Gong, Z. M. Sun, J. "Seismic performance of RC frames with diferent column-to-beam fexural strength ratios under the excitation of pulse-like and non-pulse-like ground motion.pdf," *Bull. Earthq. Eng.*, vol. 19, pp. 5139–5159, 2021, 80.

[25] Popov, E.P., Yang,T., Chang, S. Design of steel MRF connections before and after 1994 v Northridge earthquake. Engineering structure 20, (1998) 1030-1038. https://doi:10.1016/S0141-0296(97)00200-9.

[26] Chen CC, Chen SW, Chung MD, Lin MC (2005). Cyclic behaviour of unreinforced and rib-reinforced moment connections. Journal of Constructional Steel Research; 61(1):1–21.

[27] Chen CC, Lee JM, Lin MC. Behavior of steel moment connections with a single flange rib. Engineering structures 2003; 25: 1419-28

[28] Chen CC, Lin CC, Tsai CL. Evaluation of reinforced connections between steel beams and box columns. Engineering Structures 2004; 26, 1889–1904.

[29] Chen, W.-E, and Patel, K. V. "Static behaviour of beam-to-column moment connections." J. Struct. Div., ASCE, 1981, 107(9), 1815-1838.

[30] Chia B, Uang CM, Chen A. Seismic rehabilitation of pre-Northridge steel moment connections: A case Study, (2006). Journal of Constructional Steel Research: 62:783–792.

[31] Cheng, C.T., Chung L.M., "Seismic performance of steel beams to concrete-filled steel tubular column connections (2003). Journal of Constructional Steel Research: 59(3):405–26. https://doi.org/10.1016/S0143-974X(02)00033-0.

[32] Engelhard, M.D., Uang, C.M., Gross, J.L., Kasai, K. and Iwankiw, N. Modification of existing welded steel moment frame connections for seismic resistance, AISC 2003.

[33] Uang C-M, Yu Q-S, Noel S, Gross J., (2000), Cyclic testing of steel moment connections rehabilitated with RBS or welded haunch. J Struct Eng, ASCE; 126(1):57–68.

[34] Bridge, R. and Webb, J. (1992). "Thin Walled Circular Concrete Filled Steel Tubular Columns." Composite Construction of Steel and Concrete II, ASCE, pp. 634-649.

[35] Broderick, B. M., Elnashi., A. S. (1994). "Seismic Resistance of Composite Beam-Columns in Multi-Story Structures. Part 2: Analytical Model and Discussion of Results." Journal of Constructional Steel Research, Vol. 30, No.3, pp. 231-258.

[36] "Building Code Requirements for Reinforced Concrete." (1992). ACI 318-89 Revised 1992. American Concrete Institute, Detroit, Michigan.

[37] Daniels, J. H., Kroll, G. D., and Fisher J. H. (1970). "Behavior of Composite-Beam to Column Joints." Journal of the Structural Division, Proceedings of the ASCE, March, Vol. 96, No. ST3, pp. 671-685.

[38] Ge, H., and Usami, T. (1992). "Strength of Concrete-Filled Thin-Walled Steel Box Columns: Experiment." Journal of Structural Engineering, ASCE, Vol. 118, No. 11, pp. 3036-3054.

[39] Xu, F., J. Chen, and T. M. Chan. 2017. "Mechanical behaviour of concrete filled CHS connections subjected to in-plane bending." Eng. Struct. 148: 101–112. https://doi.org/10.1016/j.engstruct.2017.06.033.

[40] YujieYu, MengkeMan., ChaoZhang., Faxing Ding Seismic performance and working mechanism of innovate bottom-flange-bolted type through-diaphragm connections structures Volume 28, December 2020, Pages 1601-1615 https://doi.org/10.1016/j.istruc.2020.10.006

[41] Shin, K. J., Y. J. Kim, Y. S. Oh, and T. S. Moon. 2004. "Behavior of welded CFT column to H-beam connections with external stiffeners." Eng. Struct. 26 (13): 1877–1887. https://doi.org/10.1016/j.engstruct.2004.06.016.

[42] Mahin, S. A. "Lessons from damage to steel buildings during the Northridge earthquake." Engineering structure 20 (4): (1998) 261–270. https://doi.org/10.1016/S0141-0296(97)00032-1.

[43] Sheet, I.S., Gunasekaran, U., MacRae, G.A., "Experimental investigation of CFT column to steel connections under cyclic loading." Journal of constructional steel research 86 (2013) 167-182. http://dx.doi.org/ 10.1016/j.jcsr.2013.03.021.

[44] Jeddi, M. Sulong, N. Khanouki, M. A. "Seismic performance of a new through rib stiffener beam connection to concrete-filled steel tubular columns: An experimental study" Engg. Struc. vol 131, 15 January 2017, Pages 477-491. https://doi.org/10.1016/j.engstruct.2016.10.038

[45] Tao, Z., W. Li, B. L. Shi, and L. H. Han. 2017. "Behaviour of bolted end-plate connections to CFT column." J. Constr. Steel Res. 134: 194–208. https://doi.org/10.1016/j.jcsr.2017.04.002.

[46] Wang, J., B. Li, D. Wang, and C. Zhao. 2017. "Cyclic testing of steel beam blind bolted to CFST column composite frames with SBTD concrete slabs." Eng. Struct. 148: 293–311. https://doi.org/10.1016/j.engstruct .2017.06.065.

[47] Tizani, W., and Pitrakkos, T. 2015. "Performance of T-stub to CFT joints using blind bolts with headed anchors." J. Struct. Engg. 141 (10): 04015001. https://doi.org/10.1061/(ASCE)ST.1943-541X.0001169.

[48] Wang, Z. B., Z. Tao, D. S. Li, and L. H. Han. 2016b. "Cyclic behaviour of novel blind bolted joints with different stiffening elements." Supplement, Thin Walled Struct. 101 (SC): 157–168. https://doi.org/10 .1016/j.tws.2016.01.007.

[49] Wu, L. Y., L. L. Chung, S. F. Tsai, C. F. Lu, and G. L. Huang. 2007. "Seismic behavior of bidirectional bolted connections for CFT columns and H-beams." Eng. Struct. 29 (3): 395–407. https://doi.org/10.1016/j.engstruct.2006.05.007.

[50] Yao, H., H. Goldsworthy, and E. Gad. 2008. "Experimental and numerical investigation of the tensile behavior of blind-bolted T-stub connections to concrete-filled circular columns." J. Struct. Eng. 134 (2): 198–208. https://doi.org/10.1061/(ASCE)0733-9445(2008)134:2(198).

[51] Zhou, G., An. Y, Wu. Zhaoqi., Li. D. and Ou. Jinping 2018. "Analytical Model for Initial Rotational Stiffness of Steel Beam to Concrete-Filled Steel Tube Column Connections with Bidirectional Bolts." J. Struct. Eng. J. Struct. Eng., 2018, 144(11): 04018199. https://doi:10.1061/(ASCE)ST.1943-541X.0002187.

[52] Wang, Z. Y., W. Tizani, and Q. Y. Wang. 2010. "Strength and initial stiffness of a blind-bolt connection based on the T-stub model." Eng. Struct. 32 (9): 2505–2517. https://doi.org/10.1016/j.engstruct.2010.04.005.

[53] Tizani, W., and T. Pitrakkos. 2015. "Performance of T-stub to CFT joints using blind bolts with headed anchors." J. Struct. Eng. 141 (10): 04015001 https://doi.org/10.1061/(ASCE)ST.1943-541X.0001169.

[54] Oktavianus, Y., H. Chang, H. M. Goldsworthy, and E. F. Gad. 2017. "Component model for pull-out behaviour of headed anchored blind bolt within concrete filled circular hollow section." Eng. Struct.148: 210–224. https://doi.org/10.1016/j.engstruct.2017.06.056.

[55] Thai, H. T., and B. Uy. 2016. "Rotational stiffness and moment resistance of bolted endplate joints with hollow or CFST columns." J. Constr. Steel Res. 126: 139–152. https://doi.org/10.1016/j.jcsr.2016.07.005.

[56] Wang, S. F., and Y. Y. Chen. 2008. "Calculation of initial stiffness of beam-to-column end-plate joint." [In Chinese.] Eng. Mech. 25 (8): 109–115.

[57] Han,L. H., Li,W. and Bjorhovde, R. "Developments and advanced applications of concrete-filled steel tubular (CFST) structures: Members," *J. Constr. Steel Res.*, vol. 100, pp. 211–228, 2014, doi: 10.1016/j.jcsr.2014.04.016.

[58] Wongpakdee, N. and Leelataviwat, S. "Influence of Column Strength and Stiffness on the Inelastic Behavior of Strong-Column-Weak-Beam Frames," *J. Struct. Eng.*, vol. 143, no. 9, p. 04017124, 2017, doi: 10.1061/(asce)st.1943-541x.0001864.

[59] Zhang, C. and Tao, M. X. "Strong-column–weak-beam criterion for reinforced concrete frames subjected to biaxial seismic excitation," *Eng. Struct.*, vol. 241, no. November 2020, p. 112481, 2021, doi: 10.1016/j.engstruct.2021.112481.

[60] Ge, B. H. and Usami, T. "Strength of concrete filled thin walled steel box columns: experiment," vol. 118, no. 11, pp. 3036–3054, 1993.

[61] S. Schneider, "Axially Loaded Concrete-filled Steel Tubes," *J. Struct. Eng.*, vol. 124, no. October, pp. 1125–1138, 1998, doi: 10.1061/(asce)0733-9445(1998)124:10(1125).

[62] Uy, B. "Local and post-local buckling of concrete filled steel welded box columns," *J. Constr. Steel Res.*, vol. 47, no. 1–2, pp. 47–72, 1998, doi: 10.1016/S0143-974X(98)80102-8.

[63] Zheng, Y. He, C. and Zheng, L. "Experimental and numerical investigation of circular double-tube concrete-filled stainless-steel tubular columns under cyclic loading," *Thin-Walled Struct.*, vol. 132, no. July, pp. 151–166, 2018, doi: 10.1016/j.tws.2018.07.058.

[64] Zong, Z. H., Y. D. Lin, and J. Lin. 2004. "Experimental study on seismic performance of rectangular concrete-filled steel tube column-to-steel beam semi-rigid connections." [In Chinese.] J. Build. Struct. 25 (6):29–36.

[65] Wu, L. Y., L. L. Chung, S. F. Tsai, T. J. Shen, and G. L. Huang. 2005. "Seismic behavior of bolted beam-to-column connections for concrete filled steel tube." J. Constr. Steel Res. 61 (10): 1387–1410. https://doi.org/10.1016/j.jcsr.2005.03.007.

[66] Zong, Z. H., Y. D. Lin, H. W. Chen, J. P. Ge, and Q. Y. Yang. 2005. "Quasi-static test on concrete-filled square steel tube column to steel beam connections." [In Chinese.] J. Build. Struct. 26 (1): 77–84.

[67] Nakashima, M., K. Inoue, M. Tada. "Classification of damage to steel buildings observed in the 1995 Hyogoken-Nanbu earthquake" Engineering structure 20 (4): (1998) 271–281. https://doi.org/10.1016/s0141-0296 (97)00019-9.

[68] Chen, S.J., Chu, J.M., Chou, Z.L. Dynamic behavior of steel frames with beam flanges shaved around connection. Journal of Constructional Steel Research 42(1): (1997) 49-70. https://doi.org/10.1016/s0143-974x(97)00011-4.

[69] Popov, E.P., Yang,T., Chang, S. Design of steel MRF connections before and after 1994 v Northridge earthquake. Engineering structure 20, (1998) 1030-1038. https://doi:10.1016/S0141-0296(97)00200-9.

[70] Jones Gary, S. Fry, L. T. and Engelhardt, M. D. "Experimental Evaluation of Cyclically Loaded RBS Moment Connections," doi:10.1061/ASCE0733-94452002128:4441.

[71] Kulkerni S. A. and Vesmawala. G, "Study of steel moment connection with and without reduced beam section," *Case Stud. Struct. Eng.*, vol. 1, no. 1, pp. 26–31, 2014, doi: 10.1016/j.csse.2014.04.001.

[72] Oh K, Lee K, Chen L, Hong S-B, Yang Y (2015) Seismic performance evaluation of weak axis column-tree moment connections with reduced beam section. J. Constr. Steel Res 105:28–38. https://doi.org/10.1016/j.jcsr.2014.10.005.

[73] Paul S. and Deb, S. K. "Experimental study on a new *V*-cut RBS and CFT connections with bidirectional bolts under cyclic loadings," *J. Build. Eng.*, vol. 46, no. November 2021, p. 103688, 2022, doi: 10.1016/j.jobe.2021.103688.

[74] Zhang,X. and Ricles, J. M. "Experimental Evaluation of Reduced Beam Section Connections to Deep Columns," doi: 10.1061/ASCE0733-94452006132:3346.

[75] Pachoumis, D. Galoussis,T. E. Kalfas,G. C. N. and Efthimiou, I. Z. "Cyclic performance of steel moment-resisting connections with reduced beam sections - experimental analysis and finite element model simulation," *Eng. Struct.*, vol. 32, no. 9, pp. 2683–2692, Sep. 2010, doi: 10.1016/j.engstruct.2010.04.038.

[76] Sofias, C. E. Kalfas,C. N. and Pachoumis, D. T. "Experimental and FEM analysis of reduced beam section moment endplate connections under cyclic loading," *Eng. Struct.*, vol. 59, pp. 320–329, Feb. 2014, doi: 10.1016/j.engstruct.2013.11.010.

[77] Sofias C. E. and Pachoumis, D. T. "Assessment of reduced beam section (RBS) moment connections subjected to cyclic loading," *J. Constr. Steel Res.*, vol. 171, Aug. 2020, doi: 10.1016/j.jcsr.2020.106151.

[78] Chen, S.J., Chu, J.M., Chou, Z.L. Dynamic behavior of steel frames with beam flanges shaved around connection. Journal of Constructional Steel Research 42(1): (1997) 49-70. https://doi.org/10.1016/s0143-974x(97)00011-4.

[80] K. S. Moore & J. Y. Feng (2007) "Design of RBS Connections for Special Moment Frames",

[81] Pachoumis,D. T. Galoussis,E. G. . Kalfas, C. N and Christitsas, A. D. "Reduced beam section moment connections subjected to cyclic loading: Experimental analysis and FEM simulation," *Eng. Struct.*, vol. 31, no. 1, pp. 216–223, Jan. 2009, doi: 10.1016/j.engstruct.2008.08.007.

[82] Engelhardt, M.D., Winneberger, T., Zekany, A.j. and Potyraj, T.J., "Experimental Investigation of dogbone Moment Connections," Proceedings; (1997) National steel construction conference, American Institute of steel construction, May7-9,1997, Chicago.

[83] Deri, A. and Moslehi Tabar, A. Promotion of cyclic behaviour of reduced beam section connections restraining beam web to local buckling. Thin-Walled Structure. 73, (2011) 112–120. https://doi:10.1016/j.tws.2013.07.013.

[84] Morshedi, M. A., Dolatshahi, K. M., and Maleki, S. Double reduced beam section connection. Journal of Constructional Steel Research, *138*, (2017) 283-297. https://de.doi.org/10.1016/j/jcsr.2017.07.013.

[85] Rahnavard, R., Hassanipour, A., and Siahpolo, N. Analytical study on new types of reduced beam section moment connections affecting cyclic behavior. Case Studies in Structural Engineering, 3, (2015), 33-51. https://doi.org/10.1016/j.csse.2015.03.001.

[86] Vetr, M., Miri, M.,Haddad, A. "Seismic Behavior of a New Reduced Beam Section Connection by Drilled Holes Arrangement (RBS_DHA) on the Beam Flanges through Experimental Studies." 15th World Conference of Earthquake Engineering, (15WCEE). Lisbon, Portugal (2012).

[87] Vajdian, M., Zahraei, S.M., Mirhosseini, S.M., and Zeighami, E., "Investigation of seismic performance of RBS and drilled flange connection (DFC) containing rhombus shaped hole in steel moment frames (2020) Australian journal of civil engineering 18 (2), 246-262. https://doi.org/10.1080/14488353.2020.1771664.

[88] Fanaie, N., and Moghadam, H.S., (2019) Experimental study of rigid connection of drilled beam to CFT with external stiffeners, 153, 209-221. https://doi.org/10.1016/j.jcsr.2018.10.016.

[89] Parvari, A., Zahrai, S.M., Mirhosseini, S.M., Zeighami, E., (2020) Numerical and experimental study on the behavior of drilled flange steel beam to CFT column connections. Structures (28), 726-740. https://doi.org/10.1016/j.istruc.2020.09.021.

[90] Rahnavard, R., Hassanipour, A., and Siahpolo, N. (2015). Analytical study on new types of reduced beam section moment connections affecting cyclic behavior. Case Studies in Structural Engineering, 3, 33-51. https://doi.org/10.1016/j.csse.2015.03.001.

[91] Deri, A. and Moslehi Tabar, A. (2011) "Promotion of cyclic behaviour of reduced beam section connections restraining beam web to local buckling". Thin-Walled Struct. 73, 112–120.

[92] Li, X., Xiao, Y., Wu, Y.T., (2009) "Seismic behavior of exterior connections with steel beams bolted to CFT columns". Journal of constructional steel research. 65, 1438-1446. https://doi:10.1016/j.jcsr.2009.03.009

[93] Majid M. Nia, Saber Moradi (2020) "Effects of design factors on the cyclic response of sloped RBS moment connections". Engineering structures. 207, 110228. https://doi.org/10.1016/j.engstruct.2020.110228.

[94] Thomas Alexander Horton, Iman Hajirasouliha, Buick Davison, Zuhal Ozdemir "More efficient design of reduced beam sections (RBS) for maximum seismic performance" Journal of Constructional Steel Research 183, 106728. https://doi.org/10.1016/j.jcsr.2021.106728

[95] BIS 10262:1982: Recommended guidelines for concrete mix designs. New Delhi.

[96] BIS 383: 2002: Indian standard specification for coarse and fine aggregates from natural sources for concrete, New Delhi.

[97] BIS 4031: Part-6: 1988: Determination of compressive strength of hydraulic cement, New Delhi.

[98] BIS 12269: 1987: Specification for 53 grade ordinary Portland cement, New Delhi.

[99] BIS 2386: Part-3: 1963: Methods of test for aggregates for concrete: Specific gravity, density, voids, absorption and bulk density, New Delhi.

[101] BIS 2386: Part-1: 1963: Methods of test for aggregates for concrete: Particle size and shape, New Delhi.

[102] ASTM E8 / E8M - 2013a Standard Test Methods for Tension Testing of Metallic Materials. (American Society for Testing and Materials), https://doi:10.1520/e0008_e0008m-13a.

[103] ANSI/AISC 358-16, Seismic provision for structural steel building, Chicago (IL) An American National Standard (2016).

[104] BIS 12778:2004: Hot Rolled Parallel Flange Steel Sections for Beams, Columns and Bearing Piles - Dimensions and Section Properties [CED 7: Structural Engineering and structural sections].

[105] BIS 4923:1997: Hollow steel sections for structural use - Specification [MTD 19: Steel Tubes, Pipes and Fittings]

[106] Eurocode 3, Part 1-8, (1992) Design of Steel Structures, European Committee for Standardization (CEN).

[107] Liu, J., He, W., Chen, G., and Chen, Y.F. (2020) Seismic behavior of large-diameter CFTST column to steel beam connections, Journal of constructional steel research, 175, 106338. http://dx.doi.org/10.1016/j.jcsr.2020.106338.

[108] A. K. Chopra, Dynamics of Structures (2006): Theory and Applications of Earthquake Engineering. Englewood Cliffs, NJ, Prentice Hall.

[109] ABAQUS (*V.* 6.14-1) (2006), Theory and User's Manual, Hibbit, Karlsson & Sorensen, Inc., Pawtucket, RI

[110] Mazzoni, S., McKenna, F., Scott, M.H., Fenves GL Open system for earthquake engineering simulation (OpenSees *V*.17.7.3, 2006) command language manual (2007).

[111] Elflah, M. Theofanous, M. and Dirar, S. "Behaviour of stainless-steel beam-to-column joints-part 2: Numerical modelling and parametric study," *J. Constr. Steel Res.*, vol. 152, pp. 194–212, 2019, doi: 10.1016/j.jcsr.2018.04.017

[112] Castro, J.M., Elghazouli, A. Y., Izzuddin, B.A. [2005] "Modelling of the panel zone in steel and composite moment frames", Journal of Engineering Structures 27; 129-144.

[113] Silva. A., Jiang. Y., Macedo, L., Castro, J.M. and Monteiro, R., [2018] "Seismic performance assessment of conventional steel and steel-concrete composite moment frames using CFST columns", 12th International conference on advances in steel-concrete composite structures, (ASCCS 2018), Spain, June 27-29. http://dx.doi.org/10.4995/ASCCS2018

[114] Ibarra L.F., Medina R. A., Krawinkler H. "Hysteretic models that incorporate strength and stiffness deterioration", Earthquake Engineering and Structural Dynamics, 34(12), (2005)1489-1511.https://doi.org/10.1002/eqe.495.

[115] Lignos, D.G., Krawinkler, H. "Deterioration modeling of steel components in support of collapse prediction of steel moment frames under earthquake loading", Journal of Structural

Engineering, ASCE, Vol. 137 (11), (2011) 1291-1302. https://doi.org/10.1061/(asce)st.1943-541x.0000376.

[116] Oliveira. S., Gentili. F., Macedo, R., Carlos, J.M. and Monteiro, R., [2017] "Assessment of the seismic performance of steel frames using OpenSees", *1st European conference on OpenSees*, (ASCCS 2018), Porto, Portugal, June 19-20.

[117] Jiang. Y., Silva. A., Macedo, L., Castro, J.M. and Monteiro, R., [2018] "Seismic performance of composite structures made with concrete-filled steel tubular members", 16th European conference on earthquake engineering, (ASCCS 2018), Spain, June 18-21.

[118] Porter, K., Kennedy, R. and Bachman, R. (2007a), "Creating fragility functions for performance-based earthquake engineering", *Earthq. Spectra*, 23(2), 471-489.

[119] Gulec, C.K., Whittaker, A.S. and Hooper, J.D. (2010), "Fragility functions for low aspect ratio reinforced concrete walls", *Eng. Struct.*, 32(9), 2894-2901.

[120] Lignos, D., Kolios, D. and Miranda, E. (2010), "Fragility assessment of reduced beam section moment connections", *J. Struct. Eng*, 136(9), 1140-1150.

[121] Jeons, J., Lowes, L.N., DesRoches, R. and Brilakis, I. (2015), "Fragility curves for non-ductile reinforced concrete frames that exhibit different component response mechanisms", *Eng. Struct.*, 85, 127-143.

[122] Uang, C. M., Y. Q. Noel, and J. Gross. 2000. "Cyclic Testing of Steel Moment Connection Rehabilitated with RBS or Welded Haunch." Journal of Structural Engineering 126 (1): 67–78.

[123] Li, X., Xiao, Y., Wu, Y.T., (2009) "Seismic behavior of exterior connections with steel beams bolted to CFT columns" J. Const. Steel Research 65 1438–1446.

doi: 10.1016/j.jcsr.2009.03.009.

[124] Haldar, A. and Mahadevan, S. (2000), *Probability, Reliability, and Statistical Methods for Engineering Design*, John Wiley & Sons, Inc.

[125] Hayter, A.J. (2002), "Probability and statistic for engineers and scientists", Duxbury, Thompson Learning, USA.

[126] Shinozuka, M., Kim, S., Kushiyama, S. and Yi, J. (2002), "Fragility curves of concrete bridges retrofitted by column jacketing", *Eng. Eng. Vib.*, **1**(2), 195-205.

[127] Porter, K., Hamburger, R. and Kennedy, R. (2007b), "Practical development and application of fragility functions", *Struct. Eng. Res. Front.*, 1-16.

[128] Kottegoda, N.T., and Rosso, R. (1997) "Applied statistics for civil and environmental engineers." The McGraw-Hill Companies, Inc.

[129] Lignos, D., Kolios, D. and Miranda, E. (2010), "Fragility assessment of reduced beam section moment connections", *J. Struct. Eng*, **136**(9), 1140-1150. doi.org/10.1061/(ASCE)ST.1943-541X.0000214

LIST OF PUBLICATIONS FROM THESIS

List of Journals:

1. **Paul, S., Deb, S.K., (2021). "Seismic performance evaluation of new *V*-cut RBS to concrete filled tube connections with bidirectional bolts under cyclic loadings."** *Journal of Building Engineering*, vol. 46, 1 April, 2022. (ELSEVIER). https://doi.org/10.1016/j.jobe.2021.103688.

2. **Paul, S., Deb, S.K., (2021).** "Experimental study of *V*-cut and *VD*-cut RBS-CFT exterior connections under cyclic loadings." (under review)

3. **Paul, S., Deb, S.K., Rangoonwala, A. H., (2022).** "Seismic Behavior of bidirectional bolted drilled steel beam-CFT semi-rigid connections." (Under review)

4. **Paul, S., Deb, S.K., (2022).** "Development of experimental fragility functions for exterior RBS-column semi-rigid connection." (Under review)

5. **Paul, S., Rangoonwala, A. H., Deb, S.K., (2022).** "Experimental and numerical study on seismic performance of steel MRFs with and without RBS." (To be communicated shorthly)

List of Conferences:

1. **Paul, S., Deb, S.K., (2022). "Experimental study on radius-cut RBS and CFT connection with bidirectional bolts under cyclic loadings."**
(Paper accepted on 15.10.2022 in 17th Edition of Symposium on Earthquake Engineering, **IIT-Roorkee**.)

2. **Rangoonwala, A. H., Paul, S., Deb, S.K., (2022). "Numerical simulation of special moment resisting frame with and without RBS under cyclic load."**
(Paper accepted on 26.10.2022 in 17th Edition of Symposium on Earthquake Engineering, **IIT-Roorkee**.)

3. **Paul, S., Deb, S.K., (2022). "Simplified numerical simulation method for bolted drilled-cut RBS-CFT connections using OpenSees."**
(Paper accepted on 30.10.2022 in 8th International Congress on Computational Mechanics and Simulation, ICCMS 2022, **IIT-Indore**.)

APPENDIX-A

A.1 RESULTS OF TESTS ON CEMENT

SL. No.	Name of test	Details of relevant code	Test result
1.	Standard Consistency	IS: 4031(4)-1988	28%
2.	Initial Setting Time	IS: 4031 (5)-1988	1 hr 20 minutes
3.	Final setting time	IS 4031: (5)-1988	5 hr 25 minutes
4.	Specific gravity (p)	IS: 4031(11)-1988	3.12

A.2 COMPRESSIVE STRENGTH OF CEMENT

No of days	Compressive strength (MPa)	
	According to Test results IS 12269:1987	Test results
3.	27	26.96
7.	37	38.42
28.	53	55.36

A.3 SIEVE ANALYSIS OF FINE AGGREGATE

SL. No.	Sieve size	Weight retained (gm)	% Weight. retained	Cumulative % weight retained	% fine	Remark about Zone
1.	4.75 mm	0	0	0	100	Falls in Zone II
2.	2.36 mm	31	3.1	3.1	96.9	
3.	1.18 mm	52	5.2	8.3	91.7	
4.	600 µ	388	38.8	47.1	52.1	
5.	300 µ	348	34.8	81.9	18.1	
6.	150 µ	137	13.7	95.6	4.4	
7.	75 µ	34	3.4	99	1	

TABLE A.4 SIEVE ANALYSIS OF COARSE AGGREGATE

SL.No.	Sieve size	Weight retained (gm)	% Weight. retained	Cumulative % weight retained	% fine
1	10 mm	1401	23.35	23.35	76.65
2	7.5 mm	3785	63.08	86.43	13.57
3	4.75 mm	730	12.17	98.6	1.4
4	2.36 mm	56	0.93	99.53	0.47
5	1.18 mm	10	0.16	99.69	0.31
6	600 µ	2	0.03	99.72	0.28
7	300 µ	2	0.03	99.75	0.25
8	150 µ	3	0.05	99.80	0.2
9	<150 µ	10	0.16	99.96	0

APPENDIX-B

B.1. DESIGN OF RADIUS CUT RBS

Beam NPB 250 X 125 (IS 12778: 2004)

Grade IS 2062 E350 (Fe 490)

Yield Stress F_{yb} = 350 MPa, Ultimate Tensile Stress F_u = 490 MPa

Column SHS 220 x 220x 6 mm

Grade IS: 4923 (1997) YST 310 MPa

Yield Stress F_{yc} = 310 MPa, Ultimate Tensile Stress f_u = 450 MPa

Gravity load on the beam is due to floor tributary and exterior walls loads.

1.2D + 0.5L Load Combinations as per section 9.2c of AISC seismic provisions.

Section Properties of beam NPB 250X 150

Mass (kg/m)	A_b (mm^2)	d_b (mm)	b_{bf} (mm)	t_{bw} (mm)	t_{bf} (mm)	Z_{bpx} (mm^3)	Z_{bpy} (mm^3)
30.11	3836	250	125	6	9	373650	73630

Section Properties of Column (TUBE) 220 x 220 x 6

Mass (kg/m)	A_c (mm^2)	d_c (mm)	b_{cf} (mm)	t_{cw} (mm)	t_{cf} (mm)	Z_{cpx} (mm^3)	Z_{cpy} (mm^3)
39.59	5043	220	220	6	6	402178	402178

STEP:1. Choose trial values for RBS dimensions *a*, b and *c*

a = 62.5 mm ($0.5b_f$), b = 187.5 mm ($0.75\ d_b$), c = 28.8 mm ($0.23b_f$)

STEP:2. Compute the plastic section modulus for minimum c/s of RBS.

Plastic Section Modulus of RBS (Z_{RBS}) = Z_{px} - $2ct_{bf}(d - t_{bf})$ = 248716 mm^3

STEP:3. Established the expected yield stress of the beam

$F_{ye} = R_y F_y$ = 385 MPa, (IS 2062: E350 Grade)

R_y = Material over strength factor = 1.1 for other types of rolled shapes and bars.

STEP:4. Compute the Maximum Moment expected at center of RBS.

$$M_{RBS} = M_{pr} = C_{pr} F_{ye} Z_{RBS} = 114906330 \text{ N-mm}$$

$$M_{RBS} = M_{pr} = C_{pr} R_y F_y Z_{RBS} = 114906330 \text{ N-mm}$$

C_{pr}= Factor to account for the peak connection strength including strain hardening, local restraint, additional reinforcement, and other connection conditions.

$$C_{pr} = \frac{F_y + F_u}{2F_y} \leq 1.2 = \frac{350+490}{2\ X\ 350} = 1.2$$

STEP:5. Compute the shear force at the center of the RBS cuts at each end of the beam

$$L' = L - d_c - 2\left(a + \frac{b}{2}\right) = 2000 - 220 - 2\left(62.5 + \frac{187.5}{2}\right) = 1467.5 \text{ mm},\ V_{RBS} = \frac{2M_{RBS}}{L'} + \frac{wL'}{2} = 178614 \text{ N}$$

$$V'_{RBS} = \frac{2M_{RBS}}{L'} - \frac{wL'}{2} = 134589 \text{ N}$$

STEP:6. Compute the maximum moment expected at the face of the column.

$$M_f = M_{RBS} + V_{RBS}\left(a + \frac{b}{2}\right) = 142814767.5 \text{ N-mm}$$

STEP:7. Compute the plastic moment of the beam based on expected yield stress of beam.

$$M_{pe} = R_y F_y Z_p = 143855250 \text{ N-mm}$$

STEP:8. Check that M_f is in the range of 85 to 100 percent of M_{pe}

$$\frac{M_f}{M_{pe}} = \frac{142814767.5}{143855250} = 0.99 < 1 \text{ (OK) Thus, the}$$

Preliminary dimensions are OK. Use: a = 62.5 mm, b = 187.5 mm, c = 28.8 mm, R = 167 mm.

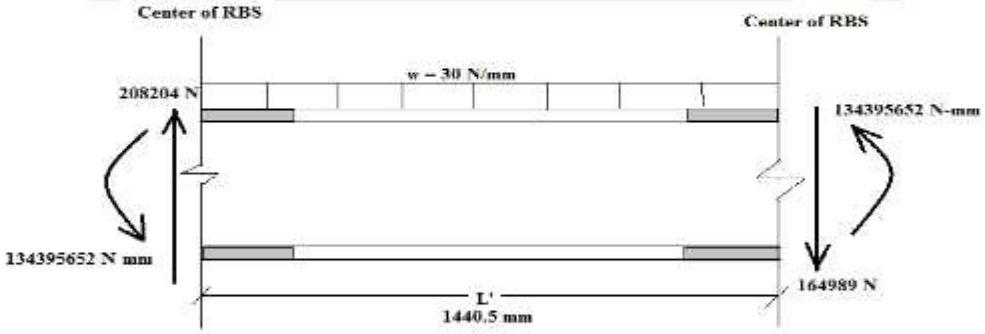

Fig.B-1 Free body Diagram of RBS

Fig.B-2 Shear force of the Portion of the beam of RBS centre

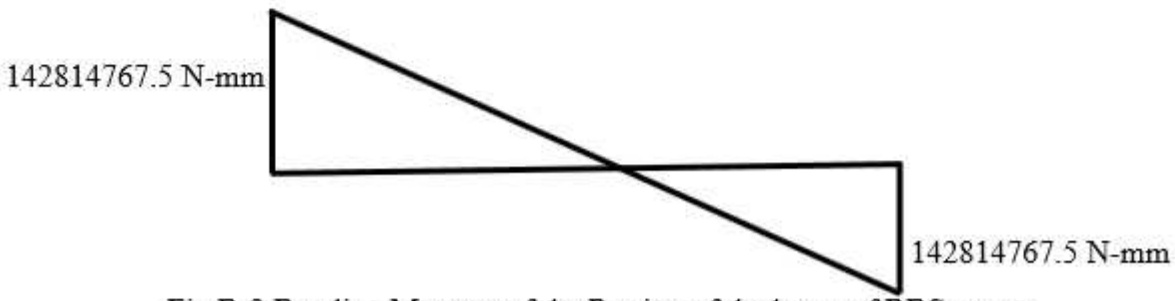

Fig.B-3 Bending Moment of the Portion of the beam of RBS centre

STEP 9: Strong Column Weak Beam Check

To check strong column-weak beam requirements, the procedure presented in the (FEMA 267A-1997) will be used, with minor modification. The equation to be used to check this requirement (Eq. 7.5.2.5-1-4 of FEMA 267A 1997) is as follows.

$$\frac{\Sigma Z_c\,(F_{yc} - f_a)}{\Sigma M_c} \geq 1$$

Assuming that the point of inflection at mid heights of the column and calculating axial stress (f_a) of 7.55 MPa in the column under earthquake and gravity loading calculate the shear force of column (V_c).

$$V_c = \frac{\Sigma M_f + V_{RBS}\left(\frac{d_c}{2} + a + \frac{b}{2}\right)}{h_t + d_b + h_b} = \frac{142814767.5 + 178614\left(\frac{220}{2} + 62.5 + \frac{187.5}{2}\right)}{2200} = 86533\ \text{N}$$

$$M_{ct} = V_c h_t = 86533 \times 971 = 84022724.27\ \text{N-mm}$$

$$M_{cb} = V_c h_b = 86533 \times 971 = 84022724.27\ \text{N-mm}$$

$$\Sigma M_c = M_{ct} + M_{cb} = 168045448.5\ \text{N-mm}$$

$$\frac{\Sigma Z_c\,(F_{yc} - f_a)}{\Sigma M_c} \geq 1 = \frac{2X\ 402178\ (310 - 7.55)}{168045448.5} = 1.45 > 1$$

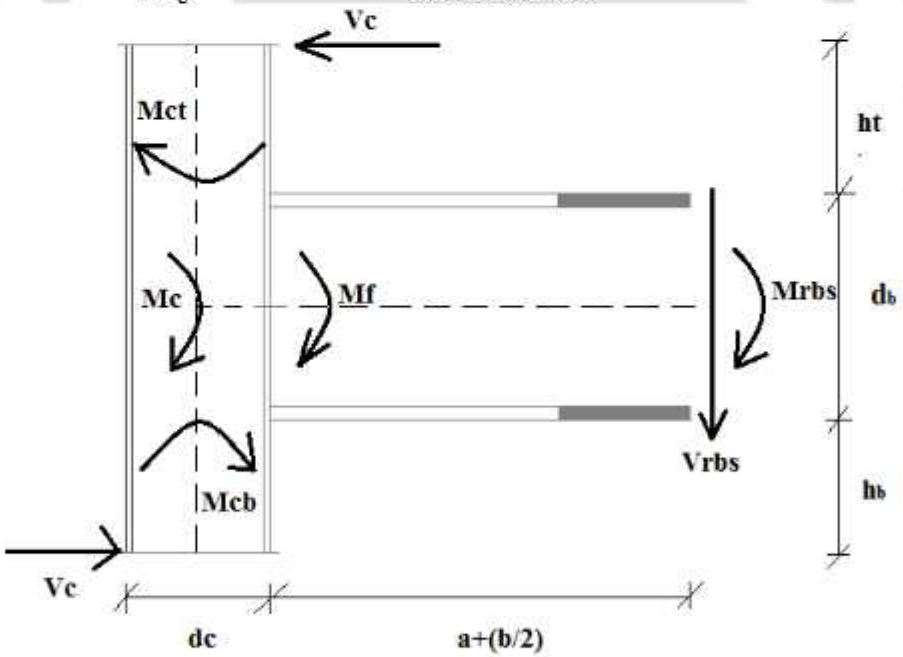

Fig.B-4 Free body Diagram of Column Moments

V_c = shear force in the column above and below the connection.
M_{ct} =column moment immediately above connection
M_{bc} = column moment immediately below connection
h_t =distance from top of beam to point of inflection in the column above the connection
h_b=distance from bottom of beam to point of inflection in the column below the connection
d_b=depth of beam

STEP 10: Check for Column Panel Zone

To check the column panel zone, the procedure used in FEMA 267A (1997) will be used. This section requires that the panel zone has sufficient strength to develop the shear force developed by $0.8\Sigma M_f$ is based on this approach; the panel zone shear force can be computed as follows:

$$\Sigma M_f = M_f = 142814767.5 \text{ N-mm}$$

$$V_{pz} = \frac{0.8\ \Sigma M_f}{0.95\ d_b} - 0.8V_c = \frac{0.8\ X\ 142814767.5}{0.95\ X\ 250} - 0.8 \text{ x } 56833 = 411834.54 \text{ N}$$

B.1.1 DESIGN OF PANEL ZONE

The shear yielding strength of the rectangular shaped panel zone filled by concrete is calculated as per (Wu et *al*., 2005) and (Wu et *al*., 2007).

Geometrical Properties (mm)											
b_c	d_c	t_f	t_w	d_b	t_{bf}	t_{bw}	t_{ep}	t_{bf}	d_h	m	n
220	220	6	6	250	125	6	16	9	16	2	4

b_c = The width of the column, d_c = the depth of the column, t_w = The thickness of the column web, t_f = The thickness of the column flange, d_b = The depth of the beam, t_{bw} = The thickness of the beam web, t_{bf} = The thickness of the beam flange, t_{ep} = The thickness of the end-plate, d_h = The diameter of the bolt hole, n= The no. of rows of bolt holes in the PZ, m= The number of bolt holes in one row.

Material Properties							
E_S (MPa)	F_{yc} (MPa)	μ_S	μ_{ep}	B	μ_c	E_c (MPa)	f'_c
200000	310	0.3	0.35	1.3	0.15	27387	30

E_s = Elastic modulus of the steel (MPa)
F_{yc} = The yield stress of the IS 4923(1997) Grade steel tube column (N/mm^2)
μ_s = Poisson's ration of the steel
μ_{ep} = friction co-efficient at the interface of endplate
f'_c = The confined compressive concrete stress including strengthened diaphragms (N/mm^2)
β = The strain hardening factor of the steel
E_c = Elastic modulus of the concrete (MPa)

Loading (N)			
t	P	F	T
130000	365602	1456000	2080000

t = The average pre-stress of each bolt, P = The axial compression acting on the CFT columns (exterior columns at the 1st story level, KN), F = friction force between end-plate and steel tube. T = Pre-stress force of all tension bolts.

Calculate the shear stiffness for two generalized column flanges (K_f):

$$I_f = \frac{b_c(t_f+t_{ep})^3}{12} = \frac{220(6+16)^3}{12} = 195214\ mm^4$$

$$K_f = 2\frac{12E_sI_f}{(d_b-t_{bf})^2} = 2\frac{12\ X\ 200000\ X\ 195214}{(258-9.2)^2} = 15137353.83 \text{ N/rad}$$

Calculate the shear stiffness for two column webs without the bolt hole (Kw):

$$G_s = \frac{E_S}{2(1+\mu_S)} = \frac{200000}{2.(1+.3)} = 76923.1 \text{ N/mm}^2$$

$K_w = 2(d_c - 2t_f)t_w G_s$ = 2 x (220-2 x 9.2) x 6.1 x 76923.1 = 192000000 N/rad

Calculate the shear stiffness of the steel column including the stiffness loss due to bolt holes (K_{wh}):

$$K_{wh} = 2(d_c - 2t_f - md_h)t_w G_s = 147692307.7 \text{ N/rad}$$

Use the superposition and calculate the shear stiffness of two column webs (K_{w1}):

$$K_{w1} = \left[\left(1 - \frac{\mathrm{nd_h}}{\mathrm{d_b}}\right).\left(\frac{1}{\mathrm{K_w}}\right) + \left(\frac{\mathrm{nd_h}}{\mathrm{d_b}}\right).\left(\frac{1}{\mathrm{K_{wh}}}\right)\right]^{-1} = 172719665.2 \text{ N/rad}$$

The shear stiffness (K_{s1}) of the steel tube at the panel zone is the superposition of the shear stiffness of the column webs (K_{w1}) and the shear stiffness of the column flanges (K_f).

$$K_{s1} = K_f + K_{w1} = 187857019.1 \text{ N/rad}$$

Calculate the pre-stress of all tension bars (T) and friction force between end-plate and steel tube (F):

T = 2mnt = 2x2x4x130000 = 2080000 N (Pre-stress is elastic state)

F = 2Tμ = 1456000 N

Calculate the yield strength of two column webs including the loss due to the bolt holes (V_{why}):

$$V_{why} = \frac{2(d_c - 2t_f - m.d_h)t_w F_y}{\sqrt{3}} = \frac{2(220-2X9.2-2X24)X6.1X310}{\sqrt{3}} = 343638.88 \text{ N}$$

Calculate the corresponding shear strain of the steel tube (γ2):

$$\gamma_2 = \frac{V_{why}}{K_{w1}} = \frac{343638.88}{172719665.2} = 0.00199 \text{ rad}$$

Calculate the yield strength of two column webs without bolt holes (V_{wy}):

$$V_{wy} = \frac{2(d_c - 2t_f)t_w F_y}{\sqrt{3}} = \frac{2(220-2X9.2)X6.1X310}{\sqrt{3}} = 446730.566$$

Calculate the yield strength of the generalized column flanges (V_{fy}):

$$V_{fy} = \frac{2(t_f + t_{ep})b_c F_y}{3(d_b - t_{bf})} = \frac{2(9.2+16)X220X\,310}{3(258-9.2)} = 4020.3644$$

Calculate the axial compressive stress (σ_x) and the lateral pre-stress acted on the concrete (σ_y) in the panel zone:

$A_c = (b_c - 2t_f)(d_c - 2t_w) = 43264\ mm^2$

$A_s = b_c d_c - A_c = 5136\ mm^2$

$$\sigma_x = f_{cp} = \frac{-PE_C}{E_S A_S + E_C A_C} = \frac{-365602 \text{ X } 27387}{200000 \text{ X } 5136 + 27387 \text{ X } 43264} = -4.52 \text{ N/mm}^2$$

$$\sigma_y = f_{ct} = \frac{T}{b_C d_C} = \frac{1270400}{220\ X\ 220} = 36.64 \text{ N/mm}^2$$

Calculate the ultimate shear stress of the inside confined concrete (τ_{cu}):

$$f_t = \frac{7.5\sqrt{1000 f_c'}}{1000} = 1.19 \text{ N/mm}^2$$

$$m_r = \frac{f_t}{f'_c} = 0.047$$

$$\tau_{cu} = \frac{1}{1+m_r}\left(\sqrt{(f_c' + \sigma_x - m_r\sigma_y)(f_c' + \sigma_y - m_r\sigma_x)}\right) = 32.67 \text{ N/mm}^2$$

Calculate the reduction factor for the shear stiffness of the confined concrete (r_c):

$$r_A = 1 - \frac{m d_h}{d_c - 2t_f} = 0.77, \qquad r_C = \left(1 - \frac{2nd_h}{d_b} + \frac{2nd_h}{d_b r_A}\right)^{-1} = 0.82$$

Calculate the ultimate shear stress of the inside confined concrete (V_{cu}):

$$V_{cu} = r_c \tau_{cu} A_c = 1296320.84 \text{ N}$$

Panel Zone Strength

Calculate the yield strength, shear stiffness, and the ultimate shear strength for the composite panel zone using the superposition theory

$$V_{y,pro} = (K_f + K_{w1})\gamma_2 + F + V_{cu} = 3161470 \text{ N}$$

$$K_{y,pro} = (K_f + K_{w1}) + \frac{(F + V_{cu})}{\gamma_2} = 1536513947 \text{ N/rad}$$

$$V_{u,pro} = V_{fy} + V_{wy} + F + V_{cu} = 3203072 \text{ N}, \; V_{y,pro} > V_{pz} \text{ Hence OK.}$$

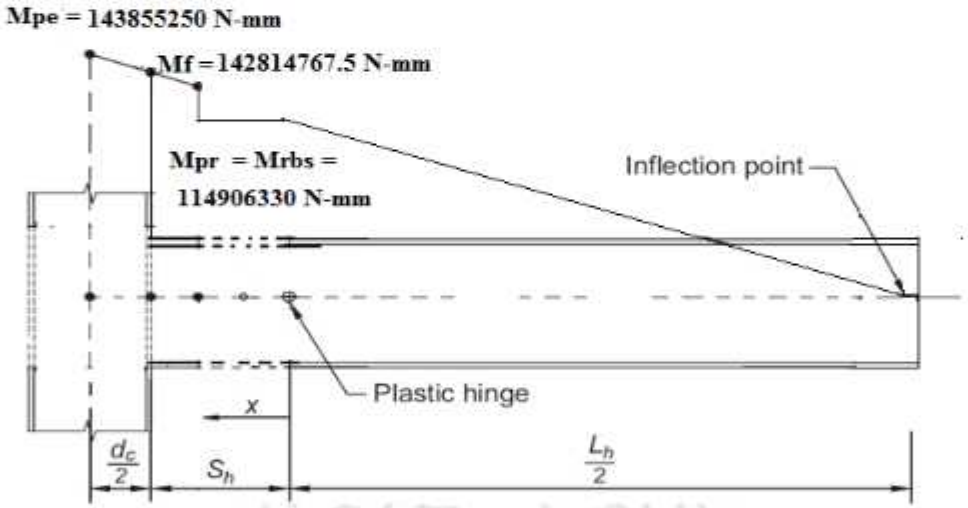

Fig.B-5 Moment gradient at different location in the radius cut RBS

B.2. DESIGN PRINCIPLE OF DRILLED CUT RBS

In order to achieve a simultaneous plastic hinge, the reduce section in the beam flange must reach a specific percentage of the plastic moment of the beam. This can be obtained using Eq.-B.1

$$\frac{M1}{Zp1} \cong \frac{M2}{Zp2} \cong \frac{M3}{Zp3} \cong \frac{Mi}{Zi} \qquad \text{(B.1)}$$

In eqn. (1) M_i is a reduced moment for designing holes in the considered section for creating fuse in the beam which is obtained through Eq. B.2 and B.3. Z_i= is the basis of the beam's plastic cross section in the reduced region, which is obtained by Eq. B.2.

$$M_i = \alpha M_{pe}\left(\frac{\frac{L}{2}-L_i}{\frac{L}{2}}\right) \quad \text{(B.2)}$$

$$M_{pe} = C_{pr}R_yF_yZ_p \quad \text{(B.3)}$$

$$Z_i = Z_p - 2D_i t_f(d_b - t_f) \quad \text{(B.4)}$$

In Eq.B.2, α is the coefficient of transfer for the plastic hinge with a recommended value of 0.85 to 1, L is the beam's span length. L_i is the hole diameter in the considered section's distance for drilling and reduced section from the column's face. D_i is the hole diameter in the considered location for the reduced section and d_b is the beam height, b_f is the beam flange width. According to the conducted studies, a minimum of three rows for holes with length of $0.75d_b$ are recommended. which in experimental models, samples were designed identical to these specifications. The remaining design procedure and required controls are the same as the RBS connection with radius cuts in ANSI/AISC 358-05.

B.2.1. DESIGN OF CONSTANT DRILLED CUT RBS

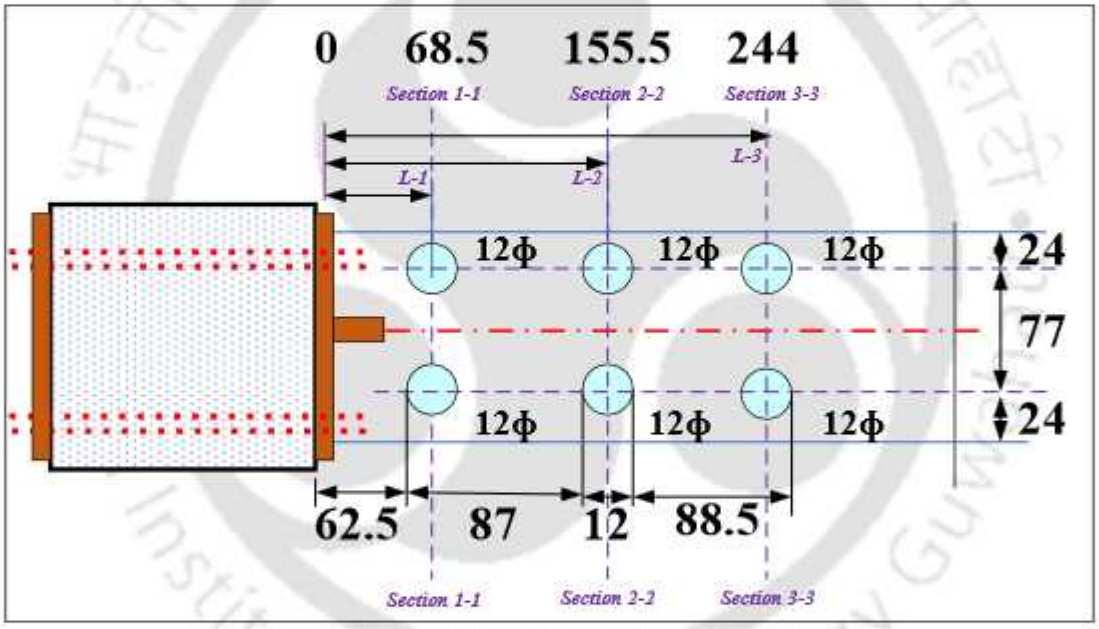

Fig.B-6 Drilling location of constant drilled-cut RBS

FOR CONSTANT HOLE

M_{pe} (N-mm)	M_1(N-mm)	M_2(N-mm)	M_3(N-mm)
143855250	125961095	114196613	102229295
L/2 (mm)	L_1(mm)	L_2(mm)	L_3(mm)
1000	68.5	155.5	244
Drilling Size	$Z_{p1}(mm^3)$	$Z_{p2}(mm^3)$	$Z_{p3}(mm^3)$
12Φ	321594	321594	321594
Bending Stress	$\frac{M1}{Zp1}$ (N/mm²)	$\frac{M2}{Zp2}$ (N/mm²)	$\frac{M3}{Zp3}$ (N/mm²)
	391.68	355.09	317.88

B.2.2. DESIGN OF VARIED DRILLED CUT RBS

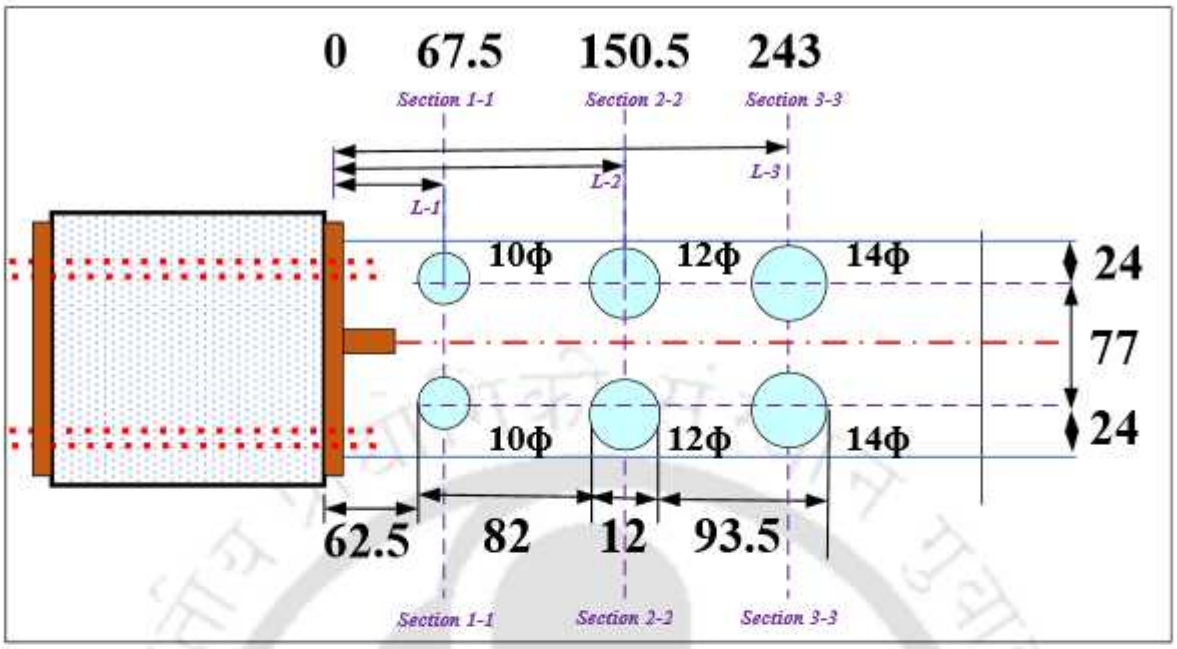

Fig.B-7 Drilling location of varied drilled-cut RBS

FOR VARIED HOLE

M_{pe} (N-mm)	M_1(N-mm)	M_2(N-mm)	M_3(N-mm)
143855250	126231543.3	114467061	102229295
L/2 (mm)	L_1(mm)	L_2(mm)	L_3(mm)
1000	67.5	150.5	243
Drill Size (Φ)	$Z_{p1}(mm^3)$ (10Φ)	$Z_{p2}(mm^3)$ (12Φ)	$Z_{p3}(mm^3)$ (14Φ)
	330270	321594	312918
Bending Stress	$\frac{M1}{Zp1}$ (N/mm²)	$\frac{M2}{Zp2}$ (N/mm²)	$\frac{M3}{Zp3}$ (N/mm²)
	382.20	355.93	326.69

Table No. 1 Plastic Section Modulus of NPB 250 x 125 with available Drill Size

Available drill size	Plastic Section Modulus of NPB 250 X 150
10φ mm	330270
12φ mm	321594
14φ mm	312918

B.3 DESIGN OF *V*-CUT RBS

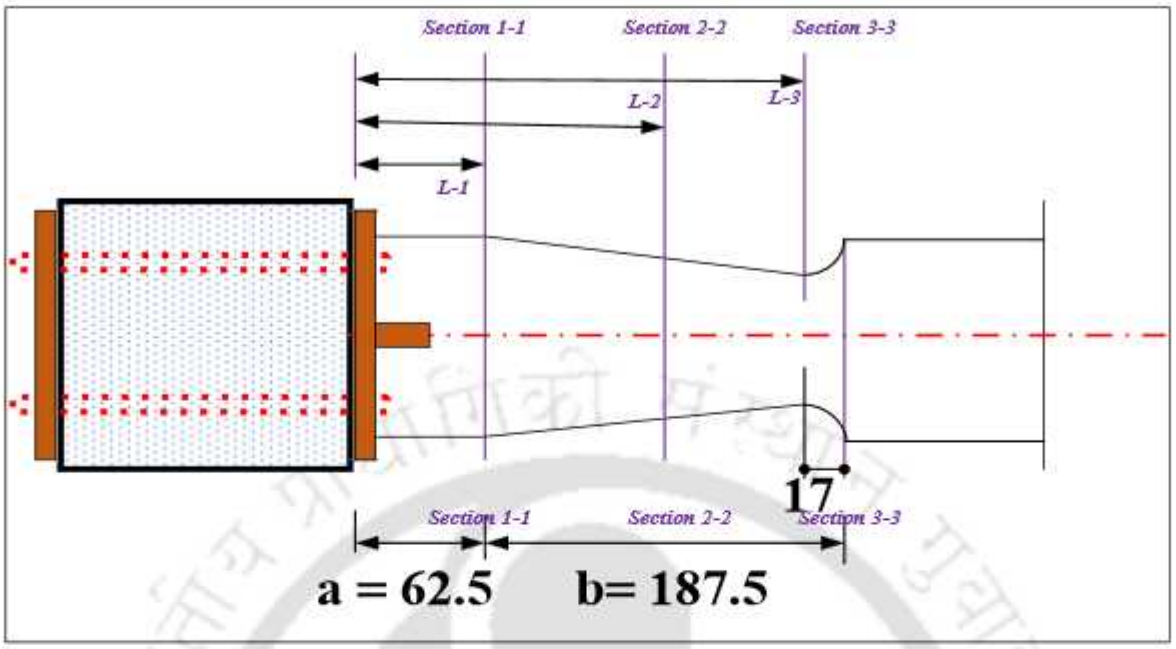

Fig.B-8 Geometric details of *V*-cut RBS

M_{pe} (N-mm)	M_1(N-mm)	M_2(N-mm)	M_3(N-mm)
143855250	134864297	114196613	110336977
L/2 (mm)	L_1(mm)	L_2(mm)	L_3(mm)
1000	62.5	150	233
Depth of cut (*d*)	c_1 (mm) = 0	c_2 (mm) = 9	c_3 (mm) = 17
Plastic section modulous	$Z_{p1}(mm^3)$ 373650	$Z_{p2}(mm^3)$ 335090	$Z_{p3}(mm^3)$ 299904
Bending Stress	$\frac{M1}{Zp1}$ (N/mm²)	$\frac{M2}{Zp2}$ (N/mm²)	$\frac{M3}{Zp3}$ (N/mm²)
	360.94	364.90	367.90

B.4 DESIGN OF END PLATE

B.4.1 END-PLATE CONNECTION

The geometric details for the end plate connections were designed in accordance with AISC/ANSI 358-05. The design procedures for the end-plate connection are described in this section.

1) Determine the prequalified limits and geometric dimensions. The geometric parameters are given in Fig.B-10.

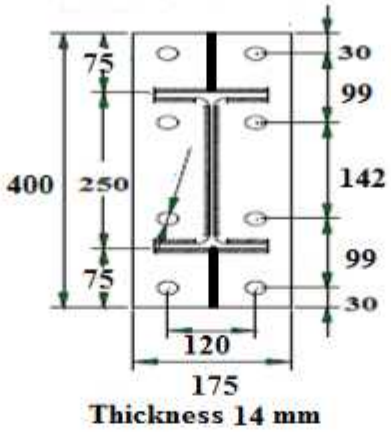

Fig.B-9 Geometric details of extended bolt stiffened end-plate

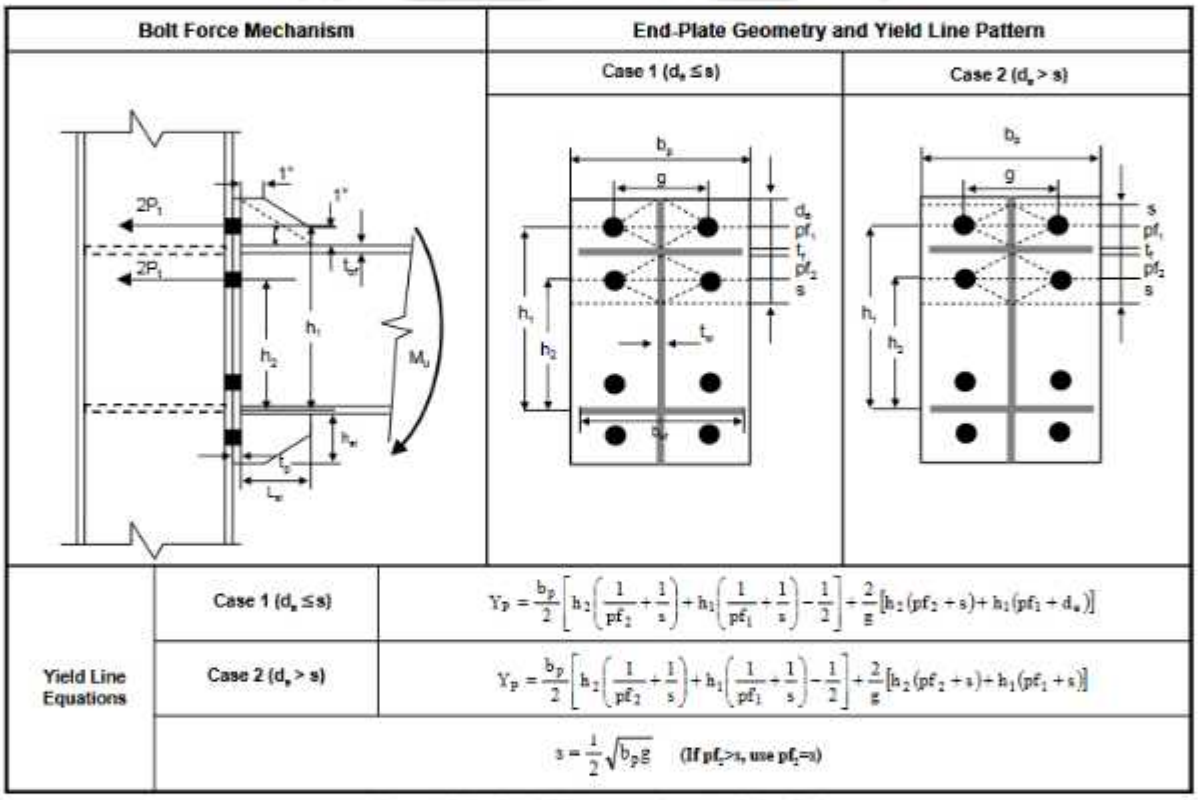

Fig.B-10 Geometry Summary and yield line failure mechanism (4 Bolt Stiffened, 4ES).

2) Determine the dimensions

Choose 4 bolt extended end-plate connection system (4ES).
b_p = 175 the width of the end-plate (mm)
g = 120 the horizontal distance between bars (mm)
P_{f1} = 45 The Vertical distance between beam flange and the center of the bar holes. (mm)
P_{f2} = 45 The Vertical distance between beam flange and the center of the bar holes. (mm)
d_e = 30 Edge distance (mm), t_f = 9 thickness of the flange (mm)
Determine the position of the tension bolts

$h_1 = (250 - \frac{9}{2} + 45) = 290.5$ mm, $h_2 = (250 - \frac{9}{2} - 9) - 45 = 191.5$ mm

3) Determine the material properties

Grade IS 2062 E350 (Fe 490), Yield Stress $F_{yp} = 350$ MPa, Ultimate Tensile Stress $F_u = 490$ MPa

B.4.2. SIZE OF BOLTS DIAMETER

1) $C_{pr} = \frac{F_y + F_u}{2F_y} \leq 1.2 = \frac{350+490}{2\ X\ 350} = 1.2$

2) Determine the design strength based on the full plastic strength of the beam

$M_{design} = M_{pe} = 143855250$ N-mm

3) Choose the required bolt diameter ($d_{b,req}$)

$$d_{b,req} = \sqrt{\frac{2\ X\ M_{pe}}{\pi\ \varphi F_{nt}\ (h_1 + h_2)}} = 14.52 \text{ mm} = 16 \text{ mm}$$

F_{nt} = Nominal tensile stress of bolt = 1000 MPa, Length of the bolt = 320 mm

($\varphi = 0.9$ for non-ductile limit state 2005 AISC Seismic Provisions) Compatible Nut **Class 10**

Details of bolts							
Product Specification (Grade)	Tensile Strength Minimum	0.2% Strength Minimum	Proof Strength Minimum	D x P (mm)	Area $(mm)^2$	Bolt Torque (N-m)	Material
Class 10.9	1000	900	830	16 x 2	157	354	Alloy steel Heat Treated

B.4.3 END-PLATE THICKNESS

1) Calculate the yield line mechanism for the end-plate

$S = \frac{1}{2}\sqrt{b_p g} = 73.49$ mm

$Y_p = \frac{b_p}{2}[h_2(\frac{1}{p_{f2}} + \frac{1}{s}) + h_1(\frac{1}{p_{f1}} + \frac{1}{s}) - \frac{1}{2}] + \frac{2}{g}[h_2(p_{f2} + s) + h_1(p_{f1} + d_e)] = 2453.97$ mm

Choose the required thickness of the end-plate

$$t_{p,req} = \sqrt{\frac{1.11\ M_{RBS}}{\emptyset_b F_{yp} Y_p}} = 12.83 \text{ mm} \cong 16 \text{ mm (OK)}$$ ($\emptyset_b = 1.0$ for ductile limit state)

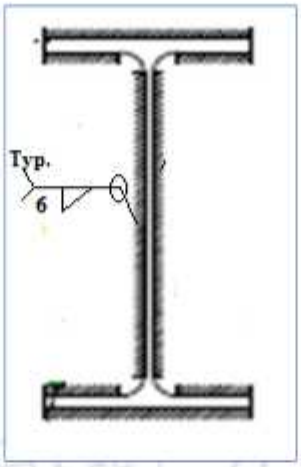

Fig.B-11 welding size of the end-plate

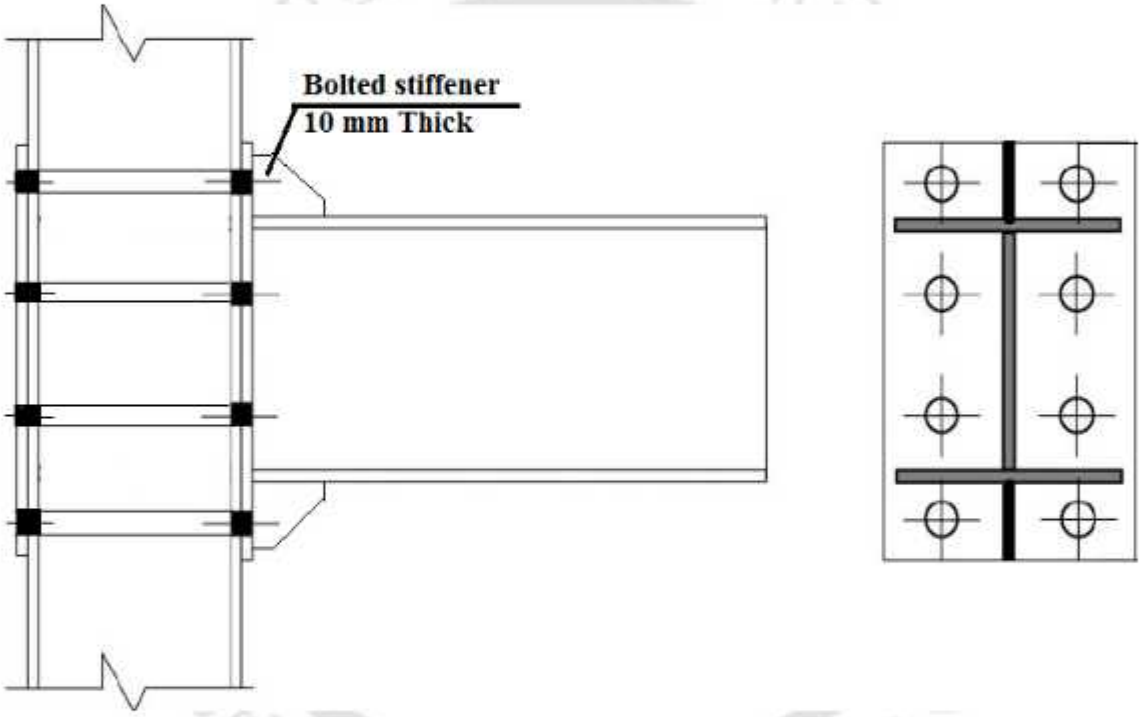

Fig.B-12 Details of 4 bolt stiffened end-plate connection geometry (4ES).

B.4.4 WELDING SIZE: BETWEEN END-PLATE AND BEAM

NPB 250 x150					B.M.	S.F.
b_f (mm)	D (mm)	t_f(mm)	t_w (mm)	$\frac{D}{2}$	M (kN-m)	F (kN)
146	250	9.2	6.1	125	172	208

Assuming unit weld throat

A_{weld} = (2 x 146 x 1) + (2 x (146-6.1) x 1) + (1 x (270-2 x 9.2)) = 804mm^2

I_{zz} = 2 x 146 x 125^2+ 2 x (146-6.1) x (146- 9.2)^2+ 2 x (250- 2 x 9.2)^3/12 = 40477264 mm^4

Section Modulus (Z) = 323819 mm^3

Direct Stress (σ_v) = $\frac{V}{A_{weld}}$ = 0.26 KN/mm, Bending stress (σ_z) = $\frac{M}{Z}$ = 0.53 KN/mm

Resultant Stress (σ_r) = 0.59 KN/mm, Permissible stress of welding = $\frac{410}{0.7 \text{ X } 15 \text{ X} 1.73}$ = 226MPa,

Size of the weld = $\frac{0.59 \text{ X } 1000}{226}$ = 2.62 mm

Minimum Thickness = 3 mm

Maximum Thickness = 9.2-1.5 = 7.7 mm

Adopt **6 mm** fillet weld of **410 grade** steel with **E43** electrodes.

B.4.5 THICKNESS OF STIFFENER

$$t_{s,min} = t_{bw} \text{ x } \frac{F_{yb}}{F_{ys}} = 6.1 \text{ x } \frac{350}{350} = 6.1 \text{ mm}$$

Where $t_{s,min}$ = Thickness of the end plate.

t_{bw} = Thickness of the beam web.

F_{yb} = Yield Stress of the beam.

F_{ys} = Yield stress of the stiffener.

Adopt **10 mm** thick stiffener.

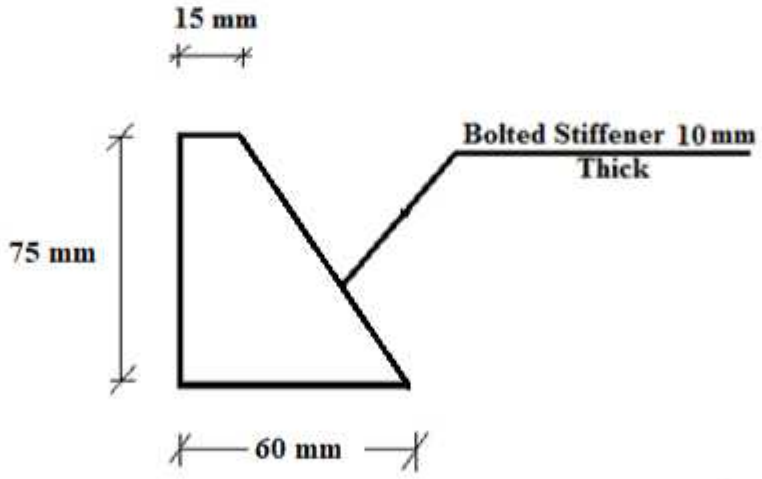

Fig.B-13 Details of the Stiffener Plate